ISRN LUTMDN/TMHP—10/5218—SE
ISSN 0282-1990

Flame turbulence interaction in lean premixed flame

Henning Carlsson

Thesis for the Degree of Master of Science

Division of Fluid Mechanics
Department of Energy Sciences
Faculty of Engineering, LTH
Lund University
P.O. Box 118
SE-221 00 Lund
Sweden

Abstract

Some fundamental physical questions were highlighted through a literature study. The mathematical model for both the initiation of turbulence fields and for the DNS solver was shown. Initial turbulence fields were then formed by the different methods and a comparison between them was made. The comparison included differences in overall pattern through the use of different energy spectrum functions, which also was reviewed in detail. Flame-turbulence interaction for a lean hydrogen-air flame at different turbulence fields, by varying the turbulent intensity and integral length scale and thereby also the Reynolds and Karlovitz numbers, was studied in 2D and 3D through DNS. The phenomenon of preheat zone broadening by turbulent eddies, the distribution of species within the reaction zone and preheat zone, pressure effects on the reaction zone, eddy pair distortion of the flame front and 2D-3D simulation differences were observed qualitatively. Turbulent flame speed, flame induced turbulence and flame surface density was measured quantitatively through defining of the instantaneous flame surface position by the fuel distribution. Based on the used set up, an outlook towards future work was done.

Contents

1. Introduction

To acquire a good understanding of the present research on turbulent flames, an overview of the subject is given first. Based on this, several fundamental questions are discussed. Finally a summary of some unresolved scientific questions is given, followed by a short description of this thesis work.

1.1. Turbulent combustion

A process where a fuel is oxidized, releasing heat, is called combustion. If the fuel is in fluid form and flows through the reaction zone, the flow case can either be laminar or turbulent. Turbulence occurs for sufficiently high Reynolds number, defined as

$$\mathrm{Re} = \frac{u \cdot l}{\nu} \tag{1}$$

where u is the flow speed, l is the characteristic length and ν is the kinematic viscosity. In a laminar case, molecular diffusion is the main transport process across the streamwise flow convection. In a turbulent flow, however, transport by turbulent eddies is also present, making the transport in the flow cross-streamwise direction severely higher. The turbulent convection speed can be estimated as the turbulent integral velocity and written as u'. In a turbulent flow, the dimensionless turbulent Reynolds number is often used to describe the characteristics of the flow. The turbulent Reynolds number is defined as

$$\mathrm{Re}_T = \frac{u' \cdot l}{\nu}, \tag{2}$$

where the characteristic length scale l now is set as the integral length scale. Both the laminar flame speed, S_L, and the laminar flame thickness, δ_L, is proportional to the square root of the diffusion coefficient and the diffusion coefficient is proportional to the viscosity. Assuming approximately equality instead of proportionality gives that expression (2) can be rewritten as

$$\mathrm{Re}_T \approx \frac{u'}{S_L} \cdot \frac{l}{\delta_L}. \tag{3}$$

Turbulent combustion is achieved when the flow of fuel/air mixture through a reaction zone is turbulent.

Depending on the intake of air into the fuel flow, the combustion can be premixed, partially premixed or non-premixed. Different types of combustion have different types of applications. Non-premixed flames are the most common type of flame used. This is due to the easiness of controlling such flames by only having possible flammability in the small region of mixing. A non-premixed flame can not flash back and is therefore very safe. A typical use of the turbulent non-premixed flame is in the diesel engine. High injection speed of the diesel is required to keep the engine at high rotational speed. To burn all fuel, the mixing by diffusion is not sufficient. When turbulence is present, the mixing of fuel and air is increased, which makes the flame burn fast enough. Premixed flames are most commonly used in spark-ignition engines, modern gas turbines and industrial gas burners. The advantage

of the premixed flame in comparison to the non-premixed flame, is that the access of air can be modulated, making it possible to alter the characteristics of the combustion. The temperature of the flame is often altered in this way, because a change in temperature also changes the emissions. When a premixed flame becomes turbulent, the flame-front becomes wrinkled and the area of it increases. An increased area results in a higher effective flame speed according to

$$S_T = \frac{A_L}{A_M} S_L , \tag{4}$$

where S_T is the turbulent flame speed, A_L is the laminar flame-front area and A_M is the mean flame-front area. This relation explains why it is necessary to have turbulent combustion in a lot of practical applications where high flame speed is required to e.g. keep an engine at high revolution speed. This information is assembled from [1], which could be reviewed for a deeper discussion.

1.2. The influence of turbulent eddies on a flame front

Laminar flames are well examined due to less required CPU time in comparison to the turbulent cases. Studies of turbulent eddies in laminar cases are not possible, but a flame's interaction with vortices can provide some valuable information [2].
Flame/vortex interaction is much dependent on the Froude number and can only exist for low numbers. The Froude number is defined as

$$Fr = \frac{U}{\sqrt{D \cdot g}} , \tag{5}$$

where U is the mean flow velocity, D is the characteristic diameter for the flow and g is the gravitational acceleration. This is due to the fact that the buoyancy effect is totally negligible for high Froude numbers, but when it is lowered, flame/vortex interaction appears, first downstream and then for higher Froude numbers, more upstream [3]. In a typical case, the flame/vortex interaction is studied by using a bluff body or a rim to stabilize the flame and

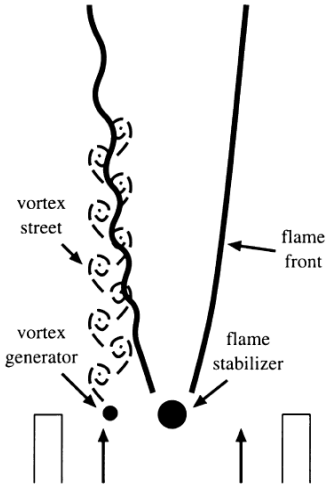

Figure 1. A bluff body stabilized flame interacts with votices [3].

then generate vortices and making them flow through the flame front. For a bluff body stabilized flame, this is illustrated in figure 1. In a turbulent case, turbulent eddies are generated.

Depending on Damköhler number, defined as

$$Da = \frac{\tau_t}{\tau_c} \tag{6}$$

and representing the ratio of the fluid time scale, τ_t, and the chemical time scale, τ_c, the vortices disturb the flame very differently. (i) For small Damköhler numbers, typically Da<0.5, the mixing with ambient gas by vortices is very intense and pockets of unburned fuel/air mixture may be formed. (ii) For intermediate Damköhler numbers, typically 0.5<Da<5, the convection interacts with the flame surface, making it wrinkled, but it stays connected without breaking points. (iii) For large Damköhler numbers, the flame remains almost unperturbed, since the chemical timescale is much smaller than the one for the vortex. This is detailed reviewed by Renard et al. [3].

It is indicated that at least for low Damköhler numbers, Da<<1, vortices contribute to significant flame contortion. However, the formation of pockets can be canceled by slow vortex rotational speed or high convectional speed, making it possible for the flame to consume them.

The pocket formation by vortices and the reaction zone curvature has been numerically studied [2, 4, 5]. Poinsot et al. [2] revised the turbulent-regime diagram originally proposed by Borghi, which helps interpreting e.g. flame quenching in turbulent combustion. Kadowaki and Hasegaw [4] performed a study of cellular, premixed, laminar flames' interaction with vortices and the differences of the flame/vortex pair interaction at variant vortex strengths by numerical simulation. Particularly the influences of the hydrodynamic, body-force and diffusive-thermal effects were studied. Najm and Wyckoff [5] studied the contortion of a premixed flame by a vortex pair and the generation of baroclinic vorticity.

In a turbulent case, turbulent eddies are the ones affecting the flame front and their interference is quite similar to that of vortices. Depending on the Karlovitz number, defined as

$$Ka = \frac{\tau_c}{\tau_k} = \left(\frac{u'}{S_L}\right)^{3/2} \left(\frac{\delta_L}{l}\right)^{1/2} \tag{7}$$

which represents the ratio of the chemical time scale and the Kolmogorov time scale, τ_k, the flame/eddy interaction acts in three different regimes: (i) For Karlovitz number lower than one, the smallest turbulent eddy is larger than the reaction zone, which makes it unable to interact within the reaction zone. The large scale eddies however will induce different flow speeds at different positions of the flame front causing wrinkling of the flame front. Increasing the Karlovitz number will decrease the size of the Kolmogorov eddy. (ii) For Ka>1 the Kolmogorov eddy is smaller than the reaction zone thickness, making it able to influence the preheat zone. In the preheat zone, the interaction performed by turbulent eddies is visualized by a not too significant broadening, making the heat and mass transfer amidst reaction zone and preheat zone larger. This is a commonly accepted theory, however, the

experimental and numerical results differ significantly and the theory could not be considered to be proven, since the point where the preheat zone broadening is visible span over the range $\sim 2 < Ka <\sim 40$ according to Driscoll [7]. The effect of flame wrinkling and, more generally, the structure of the flame have been studied numerically by e.g. Sankaran and Menon [8, 9]. (iii) When Karlovitz number exceeds 100, the Kolmogorov eddy fits into the inner layer of the reaction zone. When this is possible, the interaction of flame and eddy is very intense, causing effective mixing with ambient air and unburned fuel/air pockets could be created in the reaction zone. When unburned mixture passes through the reaction zone, the temperature will be lowered due to the unreleased thermal energy and may even exceed the limit of quenching. An interesting notation is that for a fluid time scale equal to the Kolmogorov time scale, the Karlovitz number is the inverse of the Damköhler number, which is in fact the case for laminar flames. The Damköhler number ranges described for laminar flame/vortex interaction studies could therefore easily be related to Karlovitz number ranges.

Additional numerical studies for Bunsen flame, V-flame and other apparatuses to view the flame front structure has been performed [10, 11, 12, 13]. Experiments for high Karlovitz number flames have recently been studied with high resolution [6, 14, 15].
The Kolmogorov eddy is very quickly dissipated due to viscous effects. At $Ka = 1$, where the smallest eddy should be able to interact with the preheat zone, the Kolmogorov eddy barely survives one revolution, making its effect on the preheat zone very insignificant [7]. When the Karlovitz number is raised, the Kolmogorov eddy becomes smaller than the reaction zone thickness, making the largest eddy that is able to interact with the preheat zone more long lived, causing the preheat zone width to grow with increasing Karlovitz number [7].

As a result of the wrinkling process by vortices or turbulent eddies, the wrinkled flame front will become affected by a few additional effects. The most significant influences are the diffusive thermal effect and the wrinkling enhancing Darrieus-Landau effect. For non-unity Lewis number flame, the flame velocity changes in a curved surface and changes counter actively for a convex and concave surface respectively, enhancing the existing differences. The Darrieus-Landau effect is more straight-forwardly derived from the continuity equation. If a flow is diverging, the flow speed becomes lower, making it possible for a flame to propagate faster upstream. The Darrieus-Landau effect always enhances wrinkling, while the influence of the diffusive thermal effect is dependent on the Lewis number. These effects are more detailedly reviewed in different applications by references [3, 4, 5, 16, 17]. An additional effect to keep in mind is that over a flame, the viscosity is raised. A viscosity raise dissipates the smallest eddies more quickly, making their interaction on the flame front even less important [18].

1.3. The influence of flame on turbulence

It is often desirable to increase and optimize turbulence when it is interacting with a flame. In many applications, an appropriate flame speed is sought and it is most effectively modulated with variation of the turbulent intensity. The turbulence/flame interaction is however not a one way communication. Turbulence is also induced by a propagating flame by a few different factors, detailedly reviewed by Lipatnikov and Chomiak [18].

When combustion occurs, it is a mistake to neglect pressure changes over the flame [18]. The pressure differences can be characterized as a torque, called the baroclinic torque, which depends on the misalignment of the pressure and density gradients. A counteraction of the pressure induced turbulence is, as mentioned above, the fact that the viscosity does not remain

constant during combustion. The viscosity downstream of a propagating flame is higher than that of the upstream. The raised viscosity dissipates the smallest eddies quickly, making the scale of the Kolmogorov eddy larger. In Reynolds averaged Navier-Stokes (RANS) framework, the turbulent kinetic energy equation is expressed as

$$\bar{\rho}\frac{\tilde{D}\tilde{k}}{Dt} = -\overline{\rho u_j"u_k"}\frac{\partial \tilde{u}_j}{\partial x_k} - \frac{\partial}{\partial x_k}\overline{\rho u_k"k} + \overline{u_j"\frac{\partial \tau_{jk}}{\partial x_k}} - \overline{u_k"\frac{\partial p'}{\partial x_k}} - \overline{u_k"}\frac{\partial \bar{p}}{\partial x_k} \tag{8}$$

where k is the turbulent kinetic energy, ρ is the density, u_j is the velocity in the j direction, p is pressure and τ_{ij} is the viscous stress tensor defined as

$$\tau_{ij} = \mu\left(\frac{\partial u_i}{\partial u_j} - \frac{\partial u_j}{\partial u_i}\right) - \frac{2}{3}\delta_{ij}\mu\frac{\partial u_k}{\partial x_k} \tag{9}$$

where μ is the dynamic viscosity. According to equation (8), the turbulent kinetic energy is affected by five separate terms, which can have different signs and therefore can both support as well as counteract each other. The first term on the right hand side is the production due to large scale mean velocity. The second term is the redistribution term within the flame brush. The contribution of this is small, if any. The third term is the dissipation term that can be affected by the raise of viscosity on the burned side. The fourth and fifth terms are due to pressure in the sense of the fluctuating pressure and the mean pressure gradient respectively. A DNS study of flame generated turbulence in a partially premixed case is done by Yaldizli et al. [19].

1.4. Local flame quenching in turbulent flames

As previously mentioned, at intense turbulence where Karlovitz number is high, Ka>100, flame/eddy interaction or mixing is occurring within the inner layer of the reaction zone, causing unburned fuel/air pockets to penetrate the reaction zone. The pockets left unburned lower the temperature of the flame. If the temperature is lower than the ignition temperature, fuel/air mixture will not be ignited at that position, creating an extincted area in the reaction zone called a flame hole. The dynamics and creation of flame holes in bluff body stabilized flames are described by Shanbhogue et al. [20]. According to Shanbhogue, flame holes are created under these circumstances through two mechanisms; (i) heat/radical losses to the bluff body and (ii) strains induced by flame wrinkling or divergence of the flow field. The strain needed to create a flame hole is called the extinction strain rate and is dependent on the characteristics of the flame; such as fuel composition, equivalence ratio and chemical time scale. The fact that flame holes are found is not the same as a bluff body stabilized flame is blowing off, but since extinction is associated with high Karlovitz number, the flame holes could lead towards it. A flame hole is not stationary. When it is induced, it is always convected downstream by the mean flow. The size is also changed depending on the characteristics of the edge of the flame.

Another interesting aspect of flame holes is that if a hole is initiated in a high strain region, it will affect the regions in the vicinity. A nearby location, which with its earlier local conditions would not be extinguished, can with an adjacent flame hole now fulfill the requirements.

1.5. Unresolved scientific questions

As reviewed in section 1.2, the effect of turbulence on a flame is well examined and understood for low and moderate levels of turbulence. When the Karlovitz number exceeds 100 however, the turbulence is very intense and the CPU requirements for simulation cases becomes challenging. A kind of vision would be to perform DNS on all different types of premixed flames and collecting them to form a data base. The next step is then to perform simulations on high intensity turbulence cases, which also will grant further understanding of flame holes. This could be done by studying near blowoff, bluff body stabilized flames like what Shanbhogue et al. [20] have done.
The results regarding flame generated turbulence differs quite a lot and it therefore seems likely that it requires more fundamental research. This might be done e.g. by more accurately determine the flame speed, as proposed by Driscoll [7].

1.6. Scope of this thesis

The goal of this project is to improve the understanding of the flame/turbulence interaction in the thin reaction zone regime and, maybe more importantly, in the broken reaction zone regime by using DNS. This involves all the above discussed phenomenon of turbulent eddies' effect on a flame-front, for different sizes, flame generated turbulence and local quenching of the flame-front.

2. Governing equations for DNS of turbulent flames

2.1. Governing equations

In a fluid flow, mass and momentum are conserved. This means that when simulating a turbulent flow, conservation equations for mass and momentum can be used. The conservation equations for mass and momentum are

$$\frac{\partial \rho}{\partial t} + \frac{\partial \left(\rho u_i \right)}{\partial x_i} = 0 \tag{10}$$

$$\frac{\partial \left(\rho u_j \right)}{\partial t} + \frac{\partial \left(\rho u_i u_j \right)}{\partial x_i} = -\frac{\partial p}{\partial x_j} + \frac{\partial \tau_{ij}}{\partial x_i} + \rho \sum_{k=1}^{N} Y_k f_{k,j} \tag{11}$$

where Y_k is the mass fraction of species k and f_j is the external force in the j th direction.

When simulating combustion process, the reaction proceeds through various species and an equation for the conservation of species is also required, which can be written as

$$\frac{\partial \rho Y_k}{\partial t} + \frac{\partial}{\partial x_i} \left(\rho \left(u_i + V_{k,i} \right) Y_k \right) = \dot{\omega}_k , \tag{12}$$

where $V_{k,i}$ is the i-component of the diffusion velocity of species k and $\dot{\omega}_k$ is the reaction rate of species k. The reaction rate $\dot{\omega}_k$ could be calculated by using the empirical Arrhenius expression. For e.g. a bimolecular reaction $A + B \rightarrow C$ it reads

$$\frac{dC_C}{dt} = C_A C_B A T^b \exp\left(-\frac{E_a}{R_u T}\right) \tag{13}$$

where A, b and E_a are empirical parameters and C represents concentrations of each substance.
The last very vital conservation equation is for energy and it is written as

$$\rho\frac{Dh}{Dt} - \frac{Dp}{Dt} = \frac{\partial}{\partial x_i}\left(\rho\alpha\frac{\partial h}{\partial x_i} - \rho\alpha\sum_{i=1}^{N}\left(1-\frac{1}{Le}\right)h\frac{\partial Y_j}{\partial x_i}\right) + \dot{Q}_r + \tau_{i,j} : \frac{\partial u_j}{\partial x_i} \tag{14}$$

where the enthalpy h is defined as

$$h = \sum_{i=1}^{N} Y_i h_i \tag{15}$$

$$h_i = h_i^0 + \int_{T_{ref}}^{T} c_{p,i}\left(T'\right)dT', \tag{16}$$

where α is the thermal diffusion coefficient and $\dot{Q}_r$ is the heat transferred from the environment to the control volume. The perfect gas law, or the equation of state, is also required to close the governing equations

$$p = \rho R_u T \sum_{i=1}^{N}\frac{Y_i}{W_i} \tag{17}$$

Where R_u is the universal gas constant and W_i is the molecular weight of species i.

The chemical model for hydrogen/air combustion is relatively simple in comparison to models for hydrocarbon combustion. The participating species in a hydrogen/air flame are H_2, O_2, HO_2, H_2O_2, H_2O, OH, H and O, resulting in a reaction scheme of 21 elementary chemical steps according to Williams [21].

2.2. DNS method

The simulations in this project are performed with an in-house code and the initial turbulence field is also compared with the one generated using an open source pencil code. DNS stands for direct numerical simulation. DNS solves equations (10) and (11) without any modeling, which makes the simulation more exact, but also much more dependent on the grid and available computational power. The grid has to fulfill some fundamental requirement to make the DNS possible. Both the spatial and temporal domain must be fully resolved and for the spatial part, this means that all possible length scales of turbulent eddies must have sufficient resolution. For small scales, this condition yields that the length between the grid point must be smaller than the Kolmogorov scale. For large scales, it means that the length of the computational domain must be larger than the integral scale to be assure of resolving the integral scale eddies, according to Poinsot and Veynatne [22]. The in-house code uses a first order temporal Euler solver and a spatial solver, containing a fifth order convection solver and

second order solvers for diffusion, pressure and continuity. The chemical scheme is detailed and handled by a stiff solver. The boundary conditions used are periodic, making the volume constant. The scheme of the pencil code uses third order Runge-Kutta temporal solver and has been verified to be fifth order in space [23].

3. Problem formulation and initial field

3.1. Initial field of turbulence

When a turbulence field is to be simulated, a set of initial conditions to describe a physical situation has to be prescribed along with iterations with the governing equations. This requires high processor power and is time consuming what so ever. When simulations are performed, the initial turbulence field is more commonly created by inducing a random field to the grid. The assumption of similar diffusion of turbulent eddies and molecules can thereafter create a non-physical, but well-behaving, turbulent flow [24]. In many applications, it is not vital that the velocity field is fully physical. If the velocity field is divergence free and contains the energy spectra and correlation functions of fully developed turbulence, it is sufficient [25]. Three different methods for creation of the initial field of turbulence will be described; (i) according to [25] for a general 2-D case, (ii) according to [24] for both 2-D and 3-D and (iii) a similar method to [24] but performed by the use of FFT (Fast Fourier transform).

3.1.1. Method 1

In [25], equations (18) and (19) were used to generate a 2D velocity field. A scalar field $\eta(r,t)$ was first defined, which was assumed to be homogeneous, isotropic and a stationary stochastic process according to

$$\vec{\xi}(r,t)=\left(\xi^x(r,t),\xi^y(r,t)\right)=\left(-\frac{\partial\eta(r,t)}{\partial y},\frac{\partial\eta(r,t)}{\partial x}\right), \tag{18}$$

where the statistics of the velocity field was taken from that of $\eta(r,t)$. The statistical properties of the field was then specified by the stochastic properties of

$$\tau\frac{\partial\eta(r,t)}{\partial t}=-\eta(\vec{x},t)+Q\left[\lambda^2\nabla^2\right]\zeta(r,t) \tag{19}$$

where τ and λ are the temporal and spatial correlation lengths, the ζ-field is Gaussian white noise and $Q\left[\lambda^2\nabla^2\right]$ is a mathematical operator, whose Fourier transform becomes $Q\left(\lambda^2k^2\right)$. For a grid with $N\times N$ grid points and constant distance between them, $\Delta_x=\Delta_y=\Delta$, manipulation of the scalar field by using transform to the Fourier space, discretization, time integration and random variables eventually results in the components of stochastic turbulence; the velocity field, the discrete correlation tensor $R_{mn}(s)$ and the energy spectrum $E_{\mu\nu}$, equations (19-22).

$$\xi^x_{m,n}(t)=\frac{1}{2\Delta}\left[\eta_{m,n-1}(t)-\eta_{m,n+1}(t)\right] \tag{20}$$

$$\xi^{y}_{m,n}(t) = \frac{1}{2\Delta}\left[\eta_{m+1,n}(t) - \eta_{m-1,n}(t)\right] \tag{21}$$

$$R_{mn}(s) = \frac{1}{2N^4\Delta^6}\sum_{\mu,\nu}\exp\left(-i(m\mu + n\nu)\frac{2\pi}{N} - \frac{s}{\tau}\right)$$

$$\times\left(\sin^2\left(\frac{2\pi\mu}{N}\right) + \sin^2\left(\frac{2\pi\nu}{N}\right)\right)\times\overline{\tilde{\eta}^{*}_{\mu\nu}(t)\tilde{\eta}_{\mu\nu}(t+s)} \tag{22}$$

$$E_{\mu\nu} = \frac{1}{2N^3\Delta^5}\left(\mu^2+\nu^2\right)^{1/2}\left(\sin^2\left(\frac{2\pi\mu}{N}\right) + \sin^2\left(\frac{2\pi\nu}{N}\right)\right)\times\overline{\tilde{\eta}^{*}_{\mu\nu}(t)\tilde{\eta}_{\mu\nu}(t)} \tag{23}$$

The turbulent kinetic energy, u_0^2, the time scale, t_0, and the length scale, l_0, is then given by

$$u_0^2 = \int_0^\infty E(k)\,dk \tag{24}$$

$$t_0 = \frac{1}{u_0^2}\int_0^\infty R(0,s)\,ds \tag{25}$$

$$l_0 = \frac{1}{u_0^2}\int_0^\infty R(r,0)\,dr\,. \tag{26}$$

The velocity field generated is incompressible, homogeneous, isotropic and stationary.

Careta et al. [25] reviewed two cases of turbulent flows where different initial fields are appropriate. The first one, originally proposed by Kraichnan, roots in the choice of the operator Q as

$$Q\left[\lambda^2\nabla^2\right] = \exp\left(\frac{1}{2}\lambda^2\nabla^2\right) \tag{27}$$

with the Fourier transform

$$Q\left(\lambda^2k^2\right) = \exp\left(\frac{1}{2}\lambda^2k^2\right). \tag{28}$$

This results in a correlation tensor and energy spectrum as

$$R(r,s) = \frac{\varepsilon}{8\pi\tau\lambda^4}\left(1 - \frac{r^2}{4\lambda^4}\right)\exp\left(-\frac{r^2}{4\lambda^2} - \frac{s}{\tau}\right) \tag{29}$$

$$E(k) = \frac{\varepsilon}{4\pi\tau} k^3 \exp\left(-\lambda^2 k^2\right) \tag{30}$$

and the basic parameters

$$u_0^2 = \frac{\varepsilon}{8\pi\tau\lambda^4} \tag{31}$$

$$t_0 = \tau \tag{32}$$

$$l_0 = \frac{\pi^{1/2}}{2}\lambda\,. \tag{33}$$

Figure 2 shows a simulation of turbulence generated in this way for different correlation lengths λ.

Choosing the Q operator as

$$Q\left[\lambda^2\nabla^2\right] = \left(1-\lambda^2\nabla^2\right)^{-7/6}, \tag{34}$$

with the Fourier transform

$$Q\left(-\lambda^2 k^2\right) = \left(1+\lambda^2 k^2\right)^{-7/6}, \tag{35}$$

(a) (b)

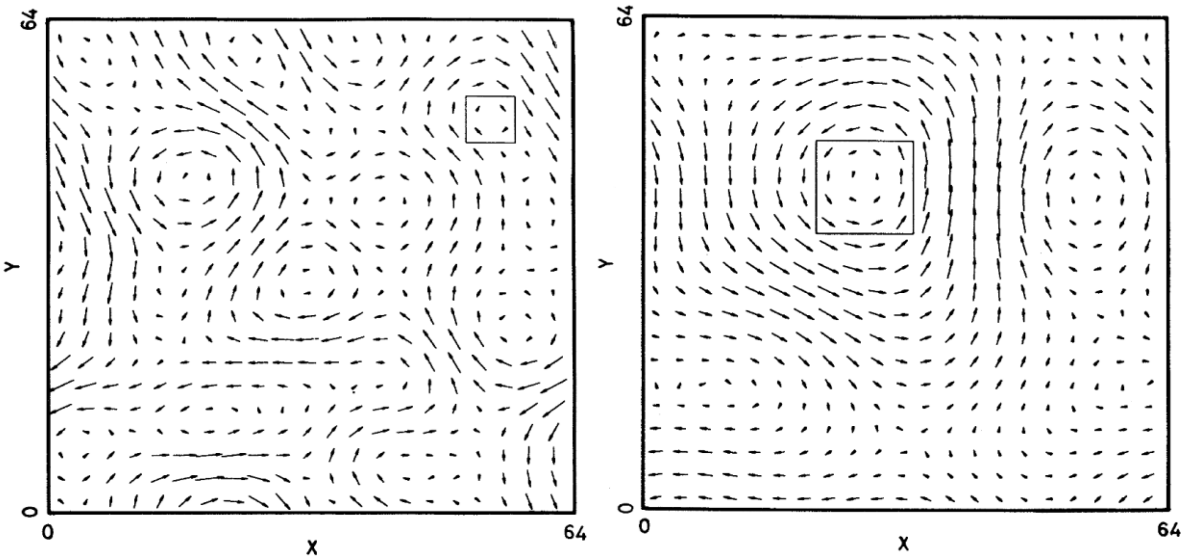

Figures 2 (a) and (b). Two Kraichnan's spectrums with grid mesh of 64x64 points. The only difference in operating condition for the images is that (a) uses $\lambda = 6$ and (b) uses $\lambda = 12$, which directly affects the size of the largest eddies according to (32) [25].

results in the so called Kárman-Obukhov's spectrum. The correlation tensor and energy spectrum then becomes

$$R(r,s)=\frac{9\varepsilon}{2^{13/3}\Gamma\left(\frac{1}{3}\right)\pi\tau\lambda^4}\left[\frac{4}{3}\rho^{1/3}K_{1/3}(\rho)-\frac{1}{2}\rho^{4/3}K_{4/3}(\rho)\right]\times\exp\left(-\frac{s}{\tau}\right) \tag{36}$$

$$E(k)=\frac{\varepsilon}{4\pi\tau}k^3\left(1+\lambda^2k^2\right)^{-7/6} \tag{37}$$

where $K_\nu(x)$ is the modified Bessel function of fractional order, Γ is the gamma function,

$$\Gamma(x)=\int_0^\infty t^{x-1}\cdot e^{-t}dt \tag{38}$$

and ρ is the non-dimensionalized spatial parameter r by $\rho=r/\lambda$. This yields turbulent intensity and length scales as

$$u_0^2=\frac{9\varepsilon}{32\pi\tau\lambda^4} \tag{39}$$

$$t_0=\tau \tag{40}$$

$$l_0=\frac{\Gamma\left(\frac{1}{2}\right)\Gamma\left(\frac{5}{6}\right)}{2\Gamma\left(\frac{1}{3}\right)}\lambda. \tag{41}$$

Figure 3 shows a turbulence field generated in this way. This spectrum's arrows are less ordered relative each other and the eddies are more diffusive.

3.1.2. Method 2

According to Kraichnan [24] a random velocity field can be initiated in the form

$$\vec{u}(\vec{x},t)=\sum_{n=1}^{N}\left[\vec{v}\left(\vec{k}_n\right)\cos\left(\vec{k}_n\cdot\vec{x}+\omega_n t\right)+\vec{w}\left(\vec{k}_n\right)\sin\left(\vec{k}_n\cdot\vec{x}+\omega_n t\right)\right]. \tag{42}$$

The conditions for $\vec{v}\left(\vec{k}_n\right)$ and $\vec{w}\left(\vec{k}_n\right)$ to assure divergence free flow, i.e.

$$\nabla\cdot\vec{u}(\vec{x},t)=0, \tag{43}$$

are checked through

$$\nabla \cdot \vec{u}(\vec{x},t) = \nabla \cdot \sum_{n=1}^{N} \left[\vec{v}(\vec{k}_n) \cos(\vec{k}_n \cdot \vec{x} + \omega_n t) + \vec{w}(\vec{k}_n) \sin(\vec{k}_n \cdot \vec{x} + \omega_n t) \right] =$$

$$= \sum_{n=1}^{N} \left[\vec{v}(\vec{k}_n) (-\sin(\vec{k}_n \cdot \vec{x} + \omega_n t) \cdot \vec{k}_n) + \vec{w}(\vec{k}_n) \cos(\vec{k}_n \cdot \vec{x} + \omega_n t) \cdot \vec{k}_n \right] = \quad (44)$$

$$= \sum_{n=1}^{N} \left[-\vec{v}(\vec{k}_n) \cdot \vec{k}_n \sin(\vec{k}_n \cdot \vec{x} + \omega_n t) + \vec{w}(\vec{k}_n) \cdot \vec{k}_n \cos(\vec{k}_n \cdot \vec{x} + \omega_n t) \right] = [(43)] = 0.$$

(44) is fulfilled for

$$\vec{k}_n \cdot \vec{v}(\vec{k}_n) = \vec{k}_n \cdot \vec{w}(\vec{k}_n) = 0 \quad (45)$$

i.e. $\vec{v}(\vec{k}_n)$ and $\vec{w}(\vec{k}_n)$ orthogonal to $\vec{k}_n$. The vectors $\vec{v}(\vec{k}_n)$ and $\vec{w}(\vec{k}_n)$ are therefore chosen as

$$\vec{v}(\vec{k}_n) = \vec{\zeta}_n \times \vec{k}_n, \ \vec{w}(k_n) = \vec{\xi}_n \times \vec{k}_n, \quad (46)$$

where $\vec{\zeta}_n$ and $\vec{\xi}_n$ are arbitrary vectors picked from Gaussian distributions to keep the randomness of the field. Only the initial field per se is of interest, the evolution in time of the initial field by the $(\omega_n \cdot t)$ term is not needed. The actual solving for time dependency is later performed by the CFD solver. The vectors $\vec{k}_n$ should also be random but must be picked so that the energy spectrum is fulfilled.

Numerically in a 3D case, the vectors $\vec{k}_n$ are distributed within the volume limited by spheres of radii equal to the lower and higher wave number of the discretized interval of the energy spectrum. Within the spheres there exist a certain number of grid points available for selection. This is depending on the radii of the spheres, hence larger radii results in more possible grid points. The number of grid points available for selection is limited by a set maximum for high wave numbers to keep the required CPU time down. The same procedure can be used in a 2D case, but with circles instead.

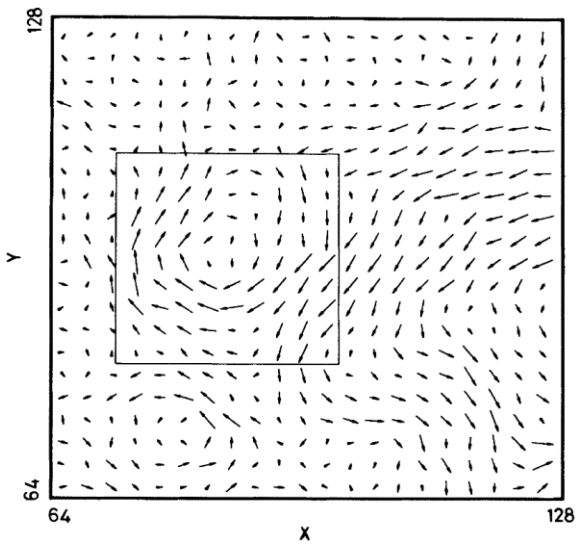

Figure 3. Initial field generated through the Kármán-Obukhov's spectrum approach [25].

According to Fourier decomposition, the velocity field could also be written as [26]

$$\begin{aligned}
&\vec{u}(\vec{x}) = \sum_{n=-N}^{N} \vec{\hat{u}}(\vec{k}_n) e^{i\vec{k}_n \vec{x}} = \\
&= \sum_{n=1}^{N} \vec{\hat{u}}(\vec{k}_n) e^{i\vec{k}_n \vec{x}} + \sum_{n=-N}^{-1} \vec{\hat{u}}(\vec{k}_n) e^{i\vec{k}_n \vec{x}} = \\
&= \sum_{n=1}^{N} \vec{\hat{u}}(\vec{k}_n) e^{i\vec{k}_n \vec{x}} + \sum_{n=1}^{N} \vec{\hat{u}}(-\vec{k}_n) e^{-i\vec{k}_n \vec{x}} = \left[\vec{\hat{u}}(-\vec{k}_n) = \vec{\hat{u}}^*(\vec{k}_n)\right] = \\
&= \sum_{n=1}^{N} \vec{\hat{u}}(\vec{k}_n) e^{i\vec{k}_n \vec{x}} + \vec{\hat{u}}^*(\vec{k}_n) e^{-i\vec{k}_n \vec{x}} = \left[\vec{\hat{u}}(\vec{k}_n) = a + bi\right] = \\
&= \sum_{n=1}^{N} (a+bi)\left(\cos(\vec{k}_n \vec{x}) + i \sin(\vec{k}_n \vec{x})\right) + (a-bi)\left(\cos(\vec{k}_n \vec{x}) - i \sin(\vec{k}_n \vec{x})\right) = \\
&= 2\sum_{n=1}^{N} a \cos(\vec{k}_n \vec{x}) - b \sin(\vec{k}_n \vec{x}).
\end{aligned} \tag{47}$$

Identification of terms in (42) with those in (47) yields

$$\begin{cases} a = \dfrac{\vec{v}(\vec{k}_n)}{2} \\ b = -\dfrac{\vec{w}(\vec{k}_n)}{2} \end{cases} \Rightarrow \vec{\hat{u}}(\vec{k}_n) = \frac{\vec{v}(\vec{k}_n)}{2} - \frac{\vec{w}(\vec{k}_n)}{2} i \,. \tag{48}$$

The turbulent kinetic energy, k_e, is given by [26]

$$k_e = \frac{1}{2}\overline{u_i u_i} = \frac{1}{2} R_{ii}(\vec{x} = 0) = \frac{1}{2} \sum_{n=-N}^{N} \hat{R}_{ii} e^{i\vec{k}_n \cdot \vec{0}} = \frac{1}{2} \sum_{n=-N}^{N} \hat{R}_{ii} \,, \tag{49}$$

whence the discretized energy spectrum is defined as [26]

$$\begin{aligned}
&E(\vec{k}_n) = \frac{1}{2}\hat{R}_{ii} = \left[\hat{R}_{ii} = \overline{\vec{\hat{u}}_i(-\vec{k}_n)\vec{\hat{u}}_i(\vec{k}_n)} = \overline{\vec{\hat{u}}_i^*(\vec{k}_n)\vec{\hat{u}}_i(\vec{k}_n)}\right] = \\
&= \frac{1}{2}\overline{\vec{\hat{u}}_i^*(\vec{k}_n)\vec{\hat{u}}_i(\vec{k}_n)} = \\
&= \frac{1}{2}\overline{\left(\frac{\vec{v}(\vec{k}_n)}{2} + \frac{\vec{w}(\vec{k}_n)}{2} i\right)\left(\frac{\vec{v}(\vec{k}_n)}{2} - \frac{\vec{w}(\vec{k}_n)}{2} i\right)} = \\
&= \frac{1}{2}\overline{\left(\frac{\vec{v}(\vec{k}_n) \cdot \vec{v}(\vec{k}_n)}{4} + \frac{\vec{w}(\vec{k}_n) \cdot \vec{w}(\vec{k}_n)}{4}\right)} = \\
&= \frac{1}{2}\overline{\left(\frac{\left|\vec{v}(\vec{k}_n)\right|^2}{4} + \frac{\left|\vec{w}(\vec{k}_n)\right|^2}{4}\right)}.
\end{aligned} \tag{50}$$

After that the vectors k_n has been distributed randomly, the coefficient vectors $\vec{v}(\vec{k}_n)$ and $\vec{w}(\vec{k}_n)$ are formed by first performing the cross product in (46), determining the direction and then determining the magnitude by multiplying with the assigned energy for each vector, governed by equation (50).

Calculation of the actual velocity field requires summation over the entire domain for each grid point, according to (42). Finally, the turbulent intensity of the created field needs to be controlled and if it differs too much from the desired one, it should be scaled. This is done by summing up the turbulent kinetic energy of the created field according to the first part of (49) and calculating the turbulent intensity. The estimation of the turbulent kinetic energy is dependant on the number of dimensions used, here written as *nDim* , according to

$$\begin{aligned} & k_e = \frac{nDim}{2} u'^2 \\ \Leftrightarrow & \\ & u' = \sqrt{\frac{2}{nDim} k_e} \end{aligned} \quad . \tag{51}$$

A factor can be calculated by dividing the desired turbulent intensity by the one received in (51) and then simply multiplying each velocity vector with that factor.

A strength of the method is that it works for 1D, 2D and 3D cases. The construction of a 2D initial turbulence field is very similar to the construction of a 3D field. Apart from putting the velocity components in the z-direction to 0, the only major difference is the random $\vec{\zeta}_n$ and $\vec{\xi}_n$ vectors, which should be projected onto the z-axis or directly created as a randomly positive or negative normal to the x-y plane.

3.1.3. Method 3

The routine of using FFT is quite similar to the method described in paragraph 4.1.2, but has the advantage of requiring less computational time. By applying the randomization of vectors k_n and calculating the Fourier coefficients from the energy spectrum according to (50), the velocity field is then constructed by performing an inverse Fourier transform by FFT.

3.1.4. High Reynolds number modeling of energy spectrum

The energy spectrum was modeled by the high Reynolds number approximation. The high Reynolds number energy spectrum approximation function is written as [26]

$$E(|k|) = C\varepsilon^{2/3} k^{-5/3} f_L(kl) f_\eta(k\eta) \tag{52}$$

with

$$f_L(kl) = \left(\frac{kl}{\left[(kl)^2 + c_L \right]^{1/2}} \right)^{5/3 + p_0} \tag{53}$$

and

$$f_\eta(k\eta) = e^{-\beta\left(\left[(k\eta)^4 + c_\eta^4\right]^{1/4} - c_\eta\right)} \tag{54}$$

where ε is the dissipation rate and C, c_L, p_0, β and c_η are modeling parameters. The energy spectrum function (52) describes the energy distribution as function of the absolute value of the wave number. Comparing the turbulent kinetic energy with the one expressed as an integral over the entire energy spectrum along with an estimation of the dissipation, results in a relation between the modeling parameters;

$$\begin{aligned}
k_e &= \int_0^\infty E(k)dk = \\
&= \int_0^\infty C\varepsilon^{2/3}k^{-5/3} f_L(kl) f_\eta(k\eta)dk = \\
&= C\varepsilon^{2/3}\int_0^\infty k^{-5/3}\left(\frac{kl}{\left[(kl)^2 + c_L\right]^{1/2}}\right)^{5/3+p_0} e^{-\beta\left(\left[(k\eta)^4 + c_\eta^4\right]^{1/4} - c_\eta\right)}dk = \left[\varepsilon \cong \frac{k_e^{3/2}}{l}\right] \cong \\
&\cong C\left(\frac{k_e^{3/2}}{l}\right)^{2/3}\int_0^\infty k^{-5/3}\left(\frac{kl}{\left[(kl)^2 + c_L\right]^{1/2}}\right)^{5/3+p_0} e^{-\beta\left(\left[(k\eta)^4 + c_\eta^4\right]^{1/4} - c_\eta\right)}dk
\end{aligned} \tag{55}$$

$$\Leftrightarrow$$

$$\begin{aligned}
1 &= C\int_0^\infty l^{-2/3}k^{-5/3}\left(\frac{kl}{\left[(kl)^2 + c_L\right]^{1/2}}\right)^{5/3+p_0} e^{-\beta\left(\left[(k\eta)^4 + c_\eta^4\right]^{1/4} - c_\eta\right)}dk = \\
&= C\int_0^\infty l^{-1}l^{-2/3}k^{-5/3}\left(\frac{kl}{\left[(kl)^2 + c_L\right]^{1/2}}\right)^{5/3+p_0} e^{-\beta\left(\left[(k\eta)^4 + c_\eta^4\right]^{1/4} - c_\eta\right)}d(kl) = \\
&= C\int_0^\infty (kl)^{-5/3}\left(\frac{kl}{\left[(kl)^2 + c_L\right]^{1/2}}\right)^{5/3+p_0} e^{-\beta\left(\left[(k\eta)^4 + c_\eta^4\right]^{1/4} - c_\eta\right)}d(kl) = \\
&= C \cdot I_1
\end{aligned} \tag{56}$$

$$\Leftrightarrow$$

$$I_1 = \frac{1}{C} \tag{57}$$

For high Reynolds numbers, a very minor part of the energy is contained in the range affected by the $f_\eta(k\eta)$ term and is in the high Reynolds number approximation neglected. The integral I_1 can in that case be rewritten as

$$I_1 = \int_0^\infty (kl)^{-5/3} \left(\frac{kl}{\left[(kl)^2 + c_L\right]^{1/2}} \right)^{5/3+p_0} e^{-\beta\left(\left[(k\eta)^4 + c_\eta^4\right]^{1/4} - c_\eta\right)} d(kl) \approx$$

$$\approx \int_0^\infty (kl)^{-5/3} \left(\frac{kl}{\left[(kl)^2 + c_L\right]^{1/2}} \right)^{5/3+p_0} d(kl) = \left[kl = x\right] =$$

$$= \int_0^\infty \frac{x^{p_0}}{\left[x^2 + c_L\right]^{\frac{5/3+p_0}{2}}} dx =$$

$$= \int_0^\infty \frac{x^{p_0}}{\left[\frac{x^2}{c_L} + 1\right]^{\frac{5/3+p_0}{2}}} \cdot \frac{1}{c_L^{\frac{5/3+p_0}{2}}} dx =$$

$$= c_L^{-5/6} \int_0^\infty \frac{\left(\frac{x^2}{c_L}\right)^{p_0/2}}{\left[\frac{x^2}{c_L} + 1\right]^{\frac{5/3+p_0}{2}}} dx = \left[\frac{x}{c_L^{1/2}} = y\right] =$$

$$= c_L^{-5/6} \int_0^\infty \frac{\left(y^2\right)^{p_0/2}}{\left[y^2 + 1\right]^{\frac{5/3+p_0}{2}}} \cdot c_L^{1/2} dy = \tag{58}$$

$$= c_L^{-1/3} \int_0^\infty \frac{\left(y^2\right)^{p_0/2}}{\left[y^2 + 1\right]^{\frac{5/3+p_0}{2}}} dy =$$

$$= c_L^{-1/3} I_2(p_0)$$

The value of c_L is relying on the choice of the modeling parameter p_0. p_0 can be chosen arbitrary, but most commonly as 2 or 4 [26]. If the integral I_2 is solved numerically by using Simpson's rule [27]

$$\int_a^b f(x)dx \approx \frac{b-a}{6}\left[f(a) + 4f\left(\frac{a+b}{2}\right) + f(b)\right], \tag{59}$$

I_1 is given by

$$\begin{cases} I_1 = c_L^{-1/3} \cdot 1.2591, \text{ for } p_0 = 2 \\ I_1 = c_L^{-1/3} \cdot 0.2294, \text{ for } p_0 = 4 \end{cases}. \tag{60}$$

According to [28], the constant C has been determined empirically from the constant C_1 to

$$C_1 = \frac{18}{55} C \approx 0.5 \tag{61}$$

$$\Rightarrow$$

$$C \approx 1.528 \approx 1.5\,. \tag{62}$$

Values for c_L then results in

$$\begin{cases} c_L = (1.5 \cdot 1.259)^3 \approx 6.74, \textit{ for } p_0 = 2 \\ c_L = (1.5 \cdot 1.031)^3 \approx 3.70, \textit{ for } p_0 = 4 \end{cases} \tag{63}$$

The dissipation rate, ε, can be written as the integral of $2\nu k^2 E(k)$ over all wave numbers [26]. The high Reynolds number approximation leads to the neglection of the $f_L(kl)$ term, since a very minor part of the energy is dissipated in the large scale region. This yields

$$\begin{aligned} \varepsilon &= \int_0^\infty 2\nu k^2 E(k) dk = \\ &= \int_0^\infty 2\nu k^2 C\varepsilon^{2/3} k^{-5/3} f_L(kl) f_\eta(k\eta) dk = \\ &= 2\nu C\varepsilon^{2/3} \int_0^\infty k^{1/3} \cdot f_L(kl) f_\eta(k\eta) \frac{d(k\eta)}{\eta} \approx \\ &\approx 2\nu C\varepsilon^{2/3} \eta^{-4/3} \int_0^\infty (k\eta)^{1/3} f_\eta(k\eta) d(k\eta) = \\ &= 2\nu C\varepsilon^{2/3} \eta^{-4/3} \int_0^\infty (k\eta)^{1/3} e^{-\beta\left(\left[(k\eta)^4 + c_\eta^4\right]^{1/4} - c_\eta\right)} d(k\eta) \end{aligned} \tag{64}$$

Rearranging terms in (64) and the using the definition of the Kolmogorov length scale lead to

$$\eta = \left(\frac{\nu^3}{\varepsilon}\right)^{1/4} \tag{65}$$

$$\Leftrightarrow$$

$$\nu = \varepsilon^{1/3} \eta^{4/3}\,. \tag{66}$$

Equations (64) and (66) gives

$$\nu = 2\nu C \int_0^\infty (k\eta)^{1/3} e^{-\beta\left(\left[(k\eta)^4 + c_\eta^4\right]^{1/4} - c_\eta\right)} d(k\eta) \tag{67}$$

$$\Leftrightarrow$$

$$\int_0^\infty (k\eta)^{1/3} e^{-\beta\left(\left[(k\eta)^4 + c_\eta^4\right]^{1/4} - c_\eta\right)} d(k\eta) = \frac{1}{2C}\,. \tag{68}$$

In the simplest case, $c_\eta = 0$, through the change of variable; $k\eta = x$, the integral could be solved using the gamma function

$$\int_0^\infty x^{1/3} e^{-\beta x} dx = \frac{1}{2C} \tag{69}$$

$$\Leftrightarrow$$

$$\beta^{-4/3}\Gamma\left(\frac{4}{3}\right) = \frac{1}{2C} \tag{70}$$

$$\Leftrightarrow$$

$$\beta = \left(2C \cdot \Gamma\left(\frac{4}{3}\right)\right)^{3/4} \approx \left(2 \cdot 1.5 \cdot 0.893\right)^{3/4} \approx 2.094\,. \tag{71}$$

According to Pope [26], β has been determined experimentally to be $\beta \approx 5.2$ which through numerically solving equation (68) using Simpson's rule (59), results in $c_\eta \approx 0.4$.

If the method is applied for low Reynolds number however, the neglect of the high and low wave number functions for the turbulent kinetic energy and the dissipation calculations respectively, is not a good estimation. Without the simplifications in (58) and (64) along with the estimation of the Kolmogorov length scale as

$$\eta \cong \frac{l}{\mathrm{Re}_T^{3/4}}\,, \tag{72}$$

the integral equations

$$\frac{1}{C} = \int_0^\infty (kl)^{-5/3} \left(\frac{kl}{\left[(kl)^2 + c_L\right]^{1/2}}\right)^{5/3+p_0} e^{-\beta\left(\left[\left(\frac{kl}{\mathrm{Re}_T^{3/4}}\right)^4 + c_\eta^4\right]^{1/4} - c_\eta\right)} d(kl) \tag{73}$$

$$\frac{1}{2C} = \int_0^\infty (k\eta)^{1/3} \left(\frac{k\eta \cdot \mathrm{Re}_T^{3/4}}{\left[\left(k\eta \cdot \mathrm{Re}_T^{3/4}\right)^2 + c_L\right]^{1/2}}\right)^{5/3+p_0} e^{-\beta\left(\left[(k\eta)^4 + c_\eta^4\right]^{1/4} - c_\eta\right)} d(k\eta) \tag{74}$$

must be solved through iteration since they are dependant. After the use of Simpson's rule (59) and iteration in two steps for a various range of turbulent Reynolds numbers, the results stabilized. The values of the constants c_L and c_η as functions of Reynolds number are displayed in figures 4 and 5 for $p_0 = 2$ and $p_0 = 4$ respectively.

Finally, the dissipation rate is to be estimated. The estimation can either be done by (i) using the estimation from equation (55), (ii) a RANS expression or (iii) through the definition of the Kolmogorov length scale by estimating both the length scale per se and the viscosity. For the fields created in this project, the first estimation (i) was used.

The dissipation rate estimation from equation (55) along with the estimation of the turbulent kinetic energy according to (51) yields

$$\varepsilon = \frac{\left(\frac{nDim}{2}\right)^{3/2} u'^3}{l}. \tag{75}$$

A quite similar way is using the RANS approach. Along with the estimation of the turbulent kinetic energy in (51) yields [26]

$$\varepsilon = C_D \frac{k^{3/2}}{l_m} \cong C_D \frac{\left(\frac{nDim}{2}\right)^{3/2} u'^3}{l_m} \tag{76}$$

Where the modeling parameter C_D and the length scale l_m is estimated according to RANS theory [26].

Equation (65) yields

$$\begin{aligned} \varepsilon &= \frac{\nu^3}{\eta^4} \cong \\ &\cong \frac{\nu^3}{\left(\frac{l}{\mathrm{Re}_T^{3/4}}\right)^4} = . \\ &= \frac{\nu^3 \cdot \mathrm{Re}_T^3}{l^4} \end{aligned} \tag{77}$$

According to [29] the dynamic viscosity of a gas mixture is calculated as

$$\mu_{mix} = \sum_{i=1}^{N} \frac{X_i \mu_i}{\sum_{j=1}^{N} X_j \varphi_{ij}}, \tag{78}$$

where φ_{ij} is given by

$$\varphi_{ij} = \frac{1}{\sqrt{8}} \left(1 + \frac{m_i}{m_j}\right)^{-1/2} \left[1 + \left(\frac{\mu_i}{\mu_j}\right)^{1/2} \left(\frac{m_j}{m_i}\right)^{1/4}\right]^2. \tag{79}$$

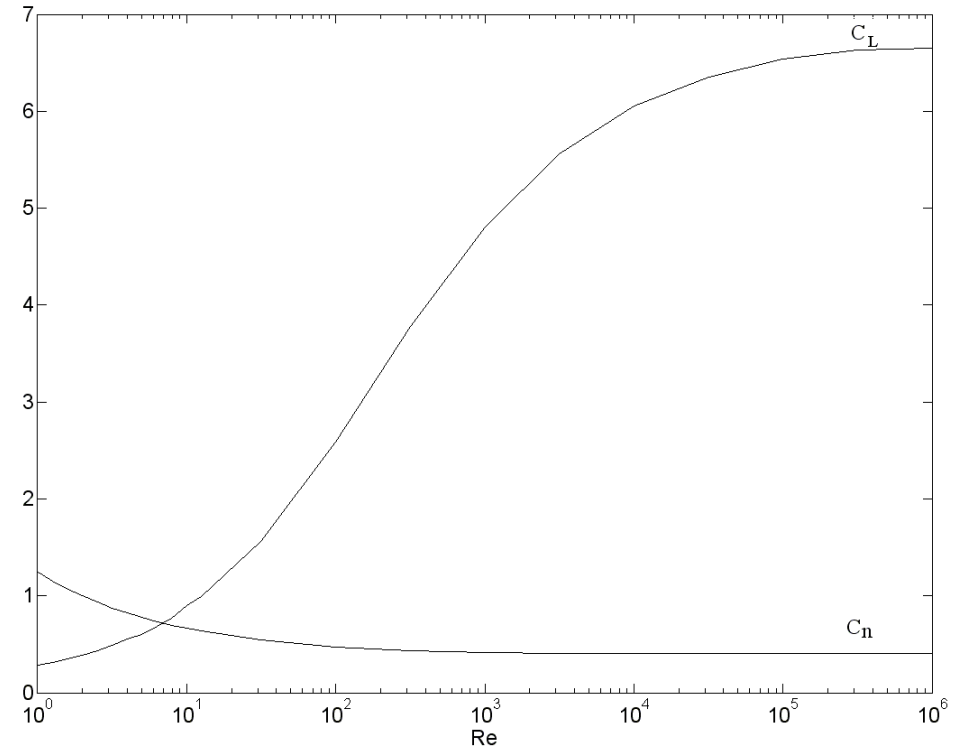

Figure 4. The modeling parameters C_L and C_η for various Reynolds numbers at $p_0 = 2$.

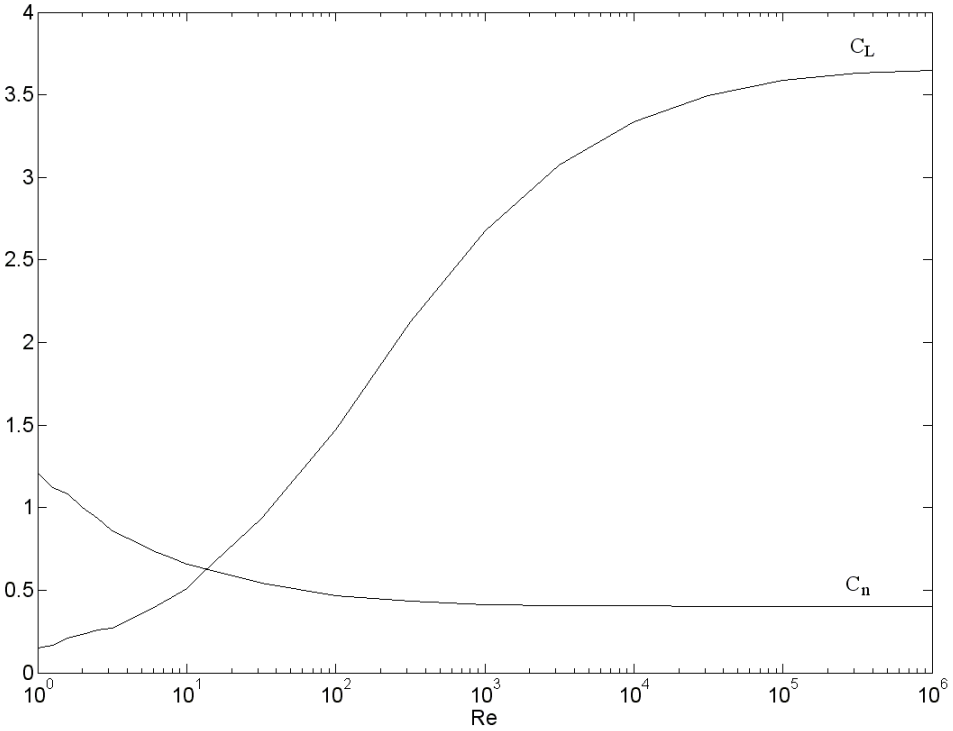

Figure 5. The modeling parameters C_L and C_η for various Reynolds numbers at $p_0 = 4$.

The kinematic viscosity is then given by

$$\nu_{mix} = \frac{\mu_{mix}}{\rho_{mix}} \tag{80}$$

which yields

$$\nu_{mix} = \sum_{i=1}^{N} \frac{X_i \nu_i}{\sum_{j=1}^{N} X_j \Phi_{ij}} \tag{81}$$

with Φ_{ij} as

$$\Phi_{ij} = \frac{1}{\sqrt{8}} \left(1 + \frac{m_i}{m_j}\right)^{-1/2} \left[1 + \left(\frac{\nu_i}{\nu_j}\right)^{1/2} \left(\frac{m_j}{m_i}\right)^{1/4}\right]^2 . \tag{82}$$

Some difficulties occur when the high Reynolds number approximation, equation (52), is used in a DNS setup, which is limited to low Reynolds numbers. Figure 6 shows a plot of the energy spectrum at various turbulent Reynolds number with the integral length scale, l, set as $l = 10^{-3}\, m$, the turbulent intensity set as $u' = 50 \frac{m}{s}$, which assumes variable viscosity when varying the Reynolds number, and with the Kolmogorov length scale estimation according to (72). All spectrums uses $p_0 = 2$, but the solid line spectrums uses fix values of the energy spectrum modeling parameters c_L and c_η as described by Pope [26], while the dashed line spectrums uses the variable values from figure 4. The figure more clearly demonstrates how severe the difference of using fixed and variable energy spectrum modeling parameters for low Reynolds numbers is. It also shows that the inertial sub-range is insignificant for $\mathrm{Re}_T < 200$ and does not become sufficient until the turbulent Reynolds number approaches at least 500. For low Reynolds numbers, it would be desirable to use some different kind of energy spectrum function with a, somewhat, more significant distribution of energy to the smaller scales.

3.1.5. Low Reynolds number modeling of energy spectrum

There are easier spectrums to use than the high Reynolds number energy spectrum approximation. For low Reynolds numbers, equation (52) can be simplified and written as an energy spectrum function [30]

$$E\left(\left|k^+\right|\right) = A \cdot u'^2 \cdot k^{+4} \cdot e^{-2k^{+2}}, \tag{83}$$

where k^+ is the nondimensionalized wave number parameter. The wave number is nondimensionalized by the maximum wave number of the domain i.e. division by 2π times the inverse of the integral length scale as shown in (84).

$$k^+ = \frac{k}{2\pi \cdot l^{-1}}. \tag{84}$$

Integrating the energy spectrum should lead to the turbulent kinetic energy, which results in the constant A according to [31]

$$\begin{aligned} k_e &= \int_0^\infty E\left(k^+\right) dk^+ = \\ &= \int_0^\infty A \cdot u'^2 \cdot k^{+4} \cdot e^{-2k^{+2}} dk^+ = \left[\int_0^\infty x^{2n} e^{-ax^2} dx = \frac{(2n-1)!!}{2(2a)^n} \sqrt{\frac{\pi}{a}}, n!! = n(n-2)...1 \right] = . \\ &= A \cdot u'^2 \cdot \frac{3}{32} \sqrt{\frac{\pi}{2}} \end{aligned} \tag{85}$$

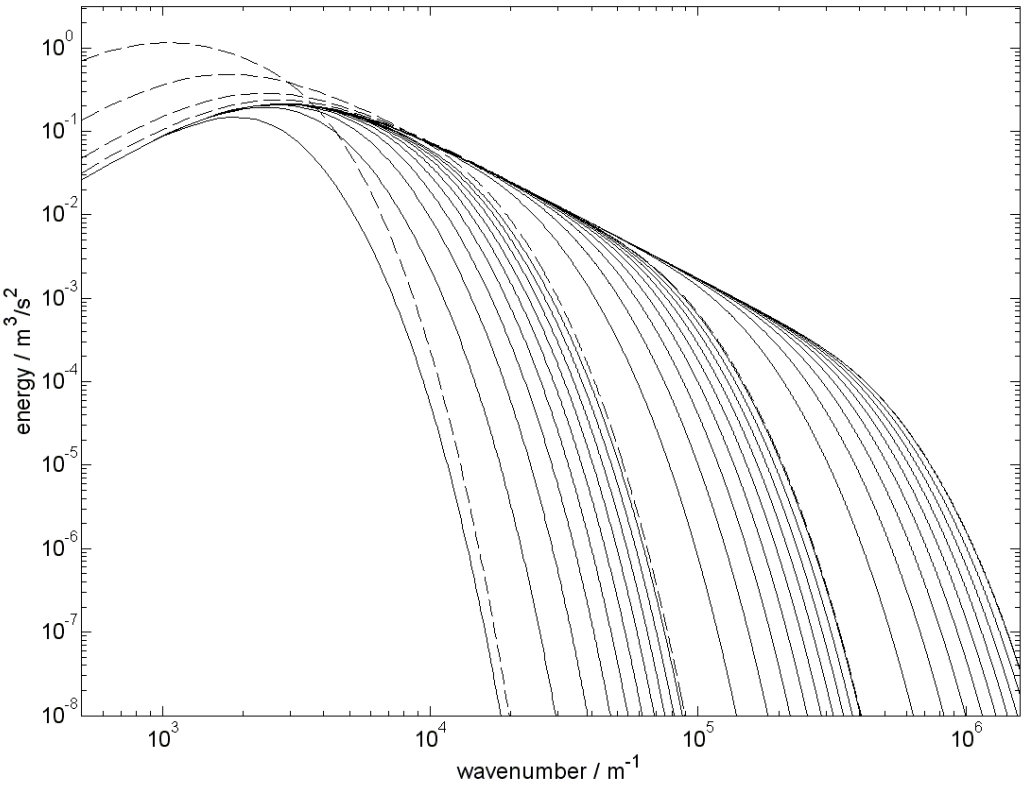

Figure 6. The high Reynolds number energy spectrum approximation (51) for various turbulent Reynolds number at $l = 10^{-3}\ m$ and $u' = 50\frac{m}{s}$. The solid line spectrums corresponds to the use of fix energy spectrum modeling parameters and turbulent Reynolds numbers, given from left to right; Re_T = 10, 20, 30, 40, 50, 60, 70, 80, 90, 100, 200, 300, 400, 500, 600, 700, 800, 900, 1000, 2000, 3000, 4000, 5000, 6000, 7000, 8000, 9000 and 10000. The dashed line spectrums corresponds to the use of varying values of c_L and c_η and turbulent Reynolds numbers, given from left to right; c_L = 0.898, 2.583, 4.809 and 6.054, c_η = 0.670, 0.471, 0.414 and 0.404, Re_T = 10, 100, 1000 and 10000 respectively.

$$\left[k_e \cong \frac{nDim}{2} u'^2 \right] \Rightarrow$$
$$A = \frac{nDim}{2} \frac{32}{3} \sqrt{\frac{2}{\pi}} = \frac{nDim \cdot 16}{3} \sqrt{\frac{2}{\pi}} \tag{86}$$

The constant A hence results in the values displayed in (87) for the different dimension cases respectively.

$$A = \begin{cases} \frac{16}{3} \left(\frac{2}{\pi} \right)^{1/2} & for\, 1D \\ \frac{32}{3} \left(\frac{2}{\pi} \right)^{1/2} & for\, 2D \\ 16 \left(\frac{2}{\pi} \right)^{1/2} & for\, 3D \end{cases}. \tag{87}$$

The low Reynolds number energy spectrum approximation is visualized in figure 7, using parameters $u' = 50 \frac{m}{s}$ and $l = 0.005\ m$ for a 1D case. The structure is similar to the low

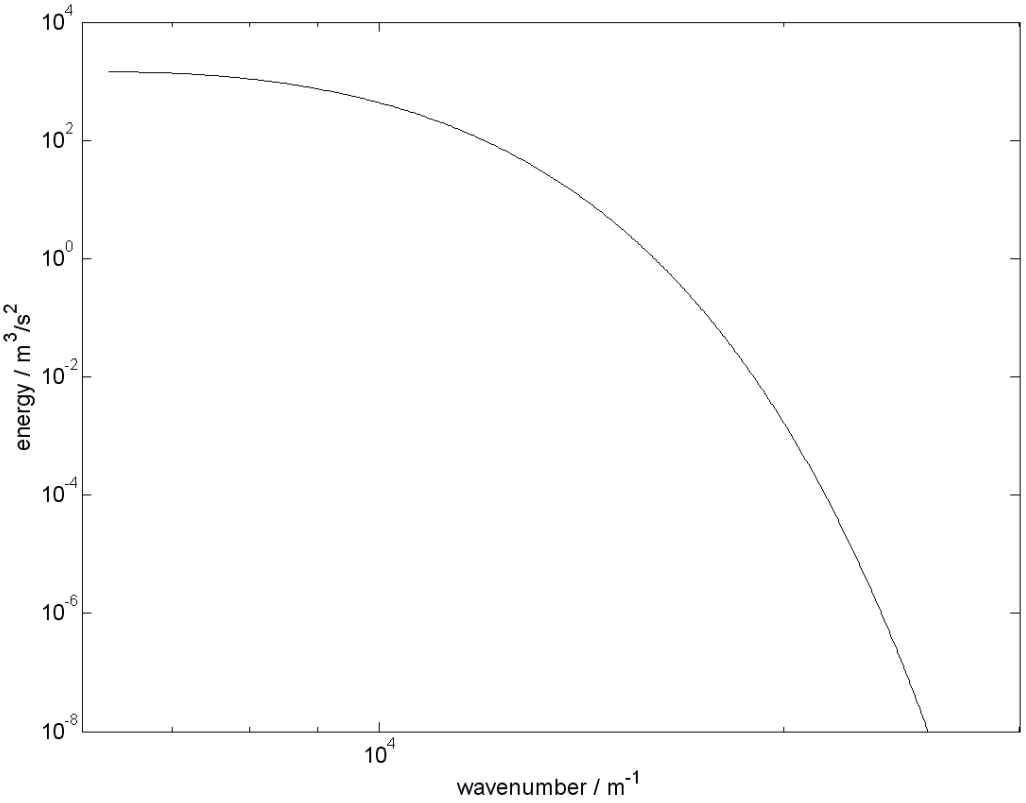

Figure 7. The low Reynolds number energy spectrum approximation (83) for a 1D cases with integral length scale $l = 0.5\,mm$ and turbulent intensity $u' = 50 \frac{m}{s}$.

Reynolds number visualizations in figure 6, although the low Reynolds number spectrum is independent of Reynolds number.

3.1.6. Testing and plots of the initial field of turbulence

As described in the previous sections, initial turbulence fields can be created in different ways. When performing simulations and visualization, three methods were tested; (i) the method described in section 3.1.2 for both 3D generated, plotted in 2D and directly 2D generated turbulence, (ii) the FFT method, as described in section 3.1.3, generated in 2D, both using the high and low Reynolds number energy spectrum approximation and (iii) the initial turbulence field created in the open source pencil code through feeding of energy at a set maximum wave number and then during iterations in time allowing it to cascade to smaller scales.

To resolve all scales of turbulence, the resolution would preferably be as high as possible. For the 3D initialization however, the number of grid points was limited by the amount of accessible memory to a $256 \times 256 \times 256$ grid mesh. The center layer in the z-direction was plotted. To simplify comparison between the different fields, the resolution for the 2D cases was also set to 256 grid points on the domain length i.e. a total grid mesh of 256×256. However, to make the visualization clearer, the initial fields are only displayed on a 64×64 mesh grid. The turbulent intensity was kept constant for all fields at $u' = 50\, m/s$ and the domain length was set to $5\, mm$. With integral scale equal to the domain length, i.e. $l = 5\, mm$, these conditions results in a turbulent Reynolds number equal to

$$\mathrm{Re}_T = \frac{u'}{S_L}\frac{l}{\delta_L} = \frac{50}{1.53}\frac{0.005}{0.000357} \approx 457.7\,. \tag{88}$$

The initial turbulence fields are pre-combustion, but since they are eventually to be used in lean premixed hydrogen air flames, Borghi's definition of the turbulent Reynolds number is still used. The values of laminar flame speed and laminar flame thickness are experimental measurements from [32].

Plots of the turbulence field generated through method 2 as described in chapter 3.1.2 are shown in figures 8 and 9 for the 3D and 2D case respectively, using the high Reynolds number approximation. Plots of turbulence generated through method 3 as described in section 3.1.3 are shown in figures 10 and 11, with integral scales of $5\, mm$ and $0.5\, mm$ respectively, using the low Reynolds number approximation. Figures 12 and 13 also shows method 3 generated turbulence with integral length scales of $5\, mm$ and $0.5\, mm$ respectively but instead using the high Reynolds number energy spectrum approximation. The pencil-code generated turbulence field is shown in figure 14, using an approximate integral length scale of $5\, mm$.

The fields in figures 8 and 9 do not differ significantly, which is expected since they are generated with identical methods. More interesting is that when testing with coarser grid, the differences become more severe. In that case, the pattern of eddies is much more discernable for 2D and the turbulence field in 3D looks more like a regular flow field. When the vorticity was measured, it was observed that the maximum vorticity for 3D case was almost one order of magnitude larger than in the 2D case. However, during the testing with coarser grid, the exact opposite was observed. This means that uneven distribution of vorticity is probably a

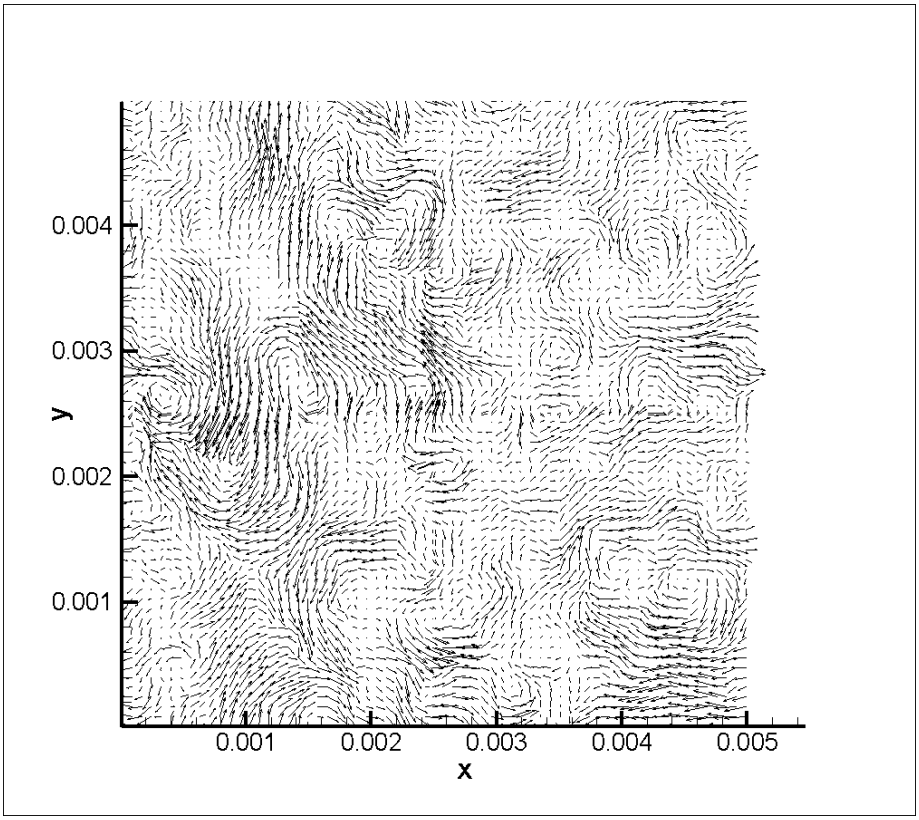

Figure 8. 3D initial turbulence field, created through method 2 as described in section 3.1.2 using energy spectrum (52). Parameters used are int. length scale of 5 mm, turbulent intensity of 50 m/s and grid resolution of 256x256.

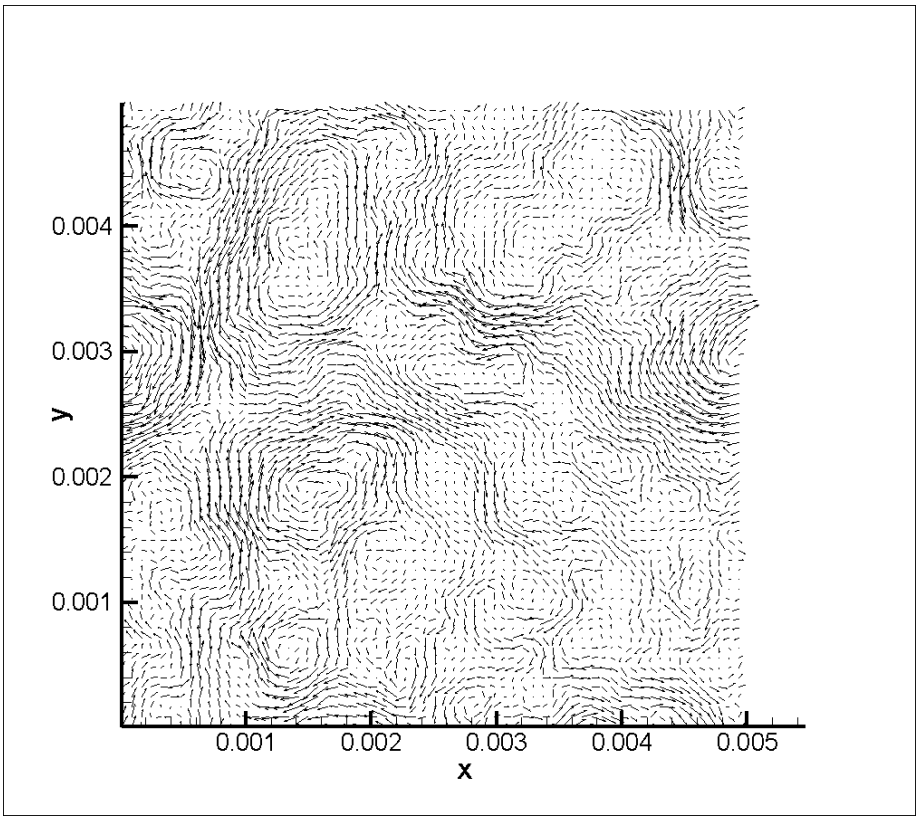

Figure 9. 2D initial turbulence field, created through method 2 as described in section 3.1.2 using energy spectrum (52) Parameters used are int. length scale of 5 mm, turbulent intensity of 50 m/s and grid resolution of 256x256.

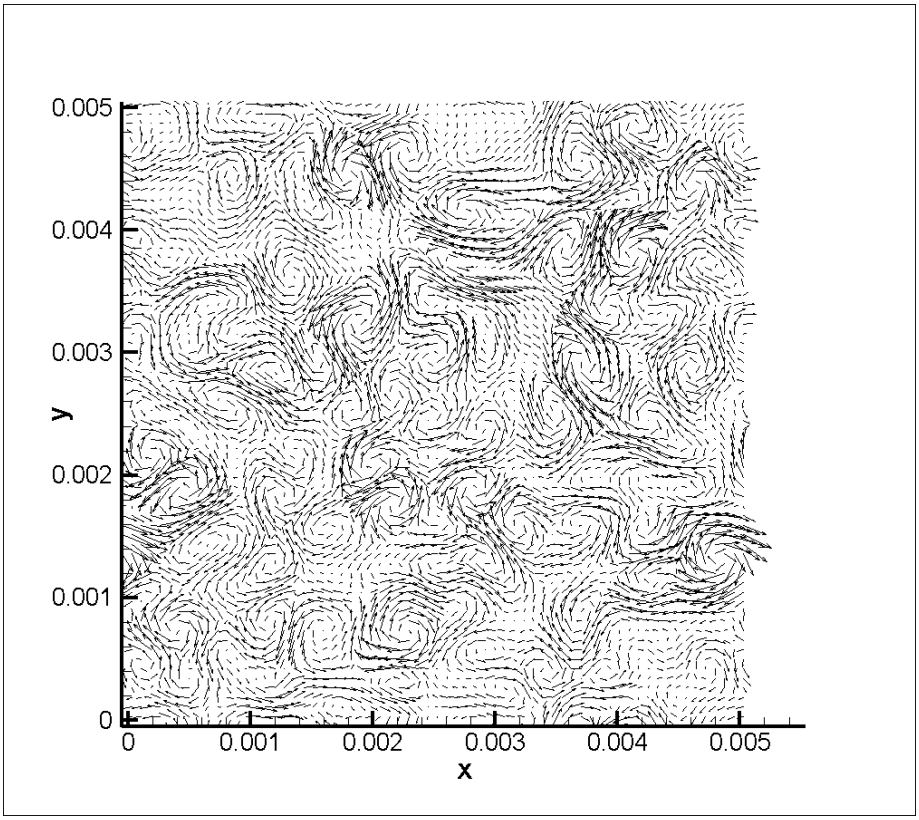

Figure 10. 2D init. turb. field, created through method 3 as described in section 3.1.3 using energy spectrum (83). Parameters used are int. length scale of 5 mm, turbulent intensity of 50 m/s and grid resolution of 256x256.

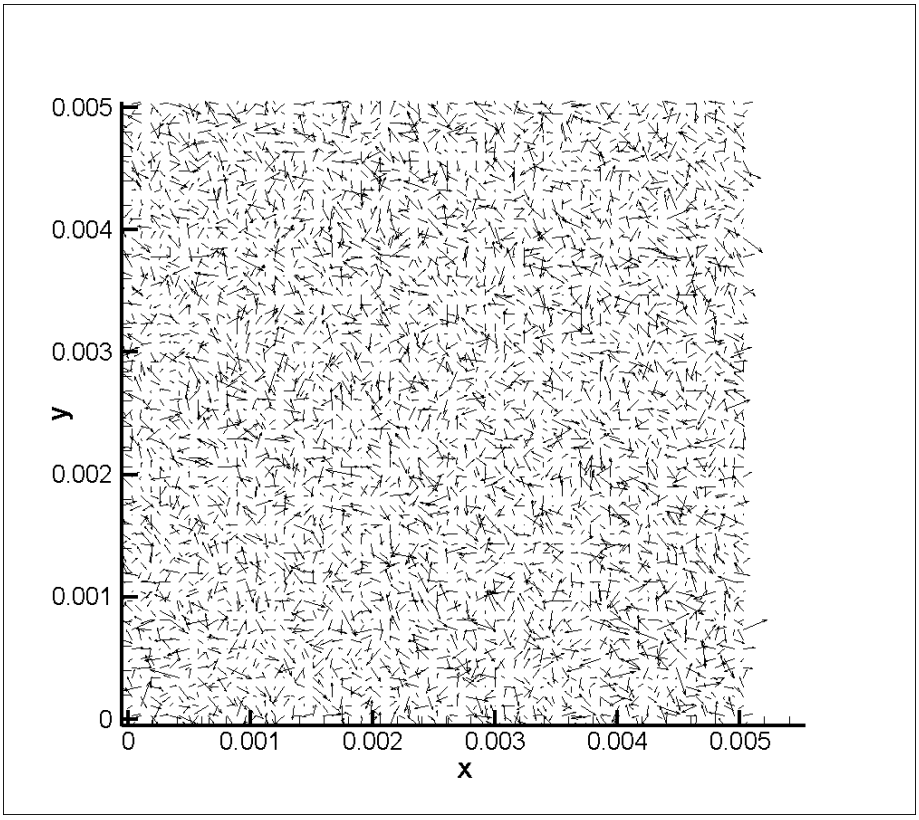

Figure 11. 2D init. turb. field, created through method 3 as described in section 3.1.3 using energy spectrum (83). Parameters used are int. length scale of 0.5 mm, turbulent intensity of 50 m/s and grid resolution of 256x256.

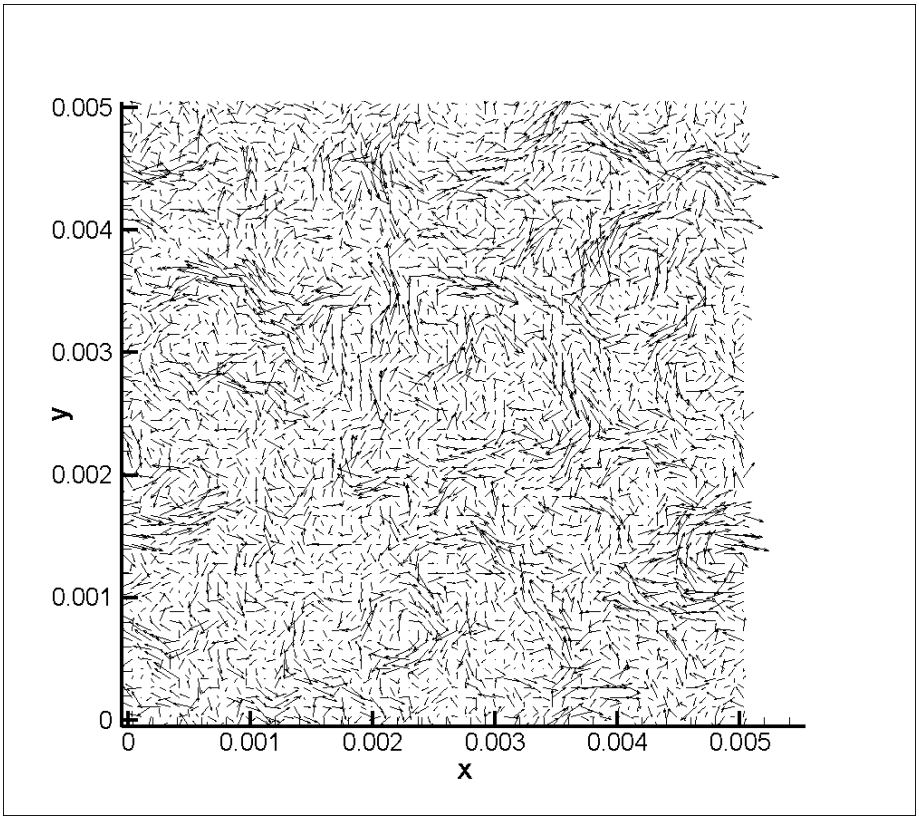

Figure 12. 2D init. turb. field, created through method 3 as described in section 3.1.3 using energy spectrum (52). Parameters used are int. length scale of 5 mm, turbulent intensity of 50 m/s and grid resolution of 256x256.

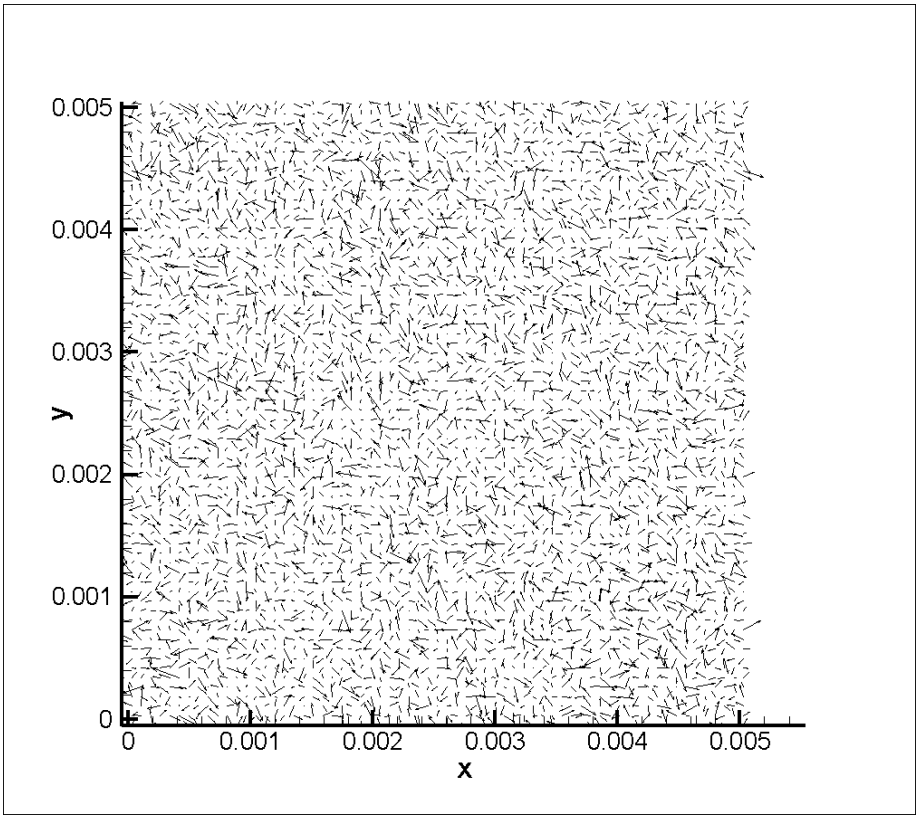

Figure 13. 2D init. turb. field, created through method 3 as described in section 3.1.3 using energy spectrum (52). Parameters used are int. length scale of 0.5 mm, turbulent intensity of 50 m/s and grid resolution of 256x256.

matter of coincidences. Also, the maximum root-mean-square velocity fluctuates a lot between different simulations of the same field. For the fields visualized in figures 8 and 9, the maximum root mean square velocity was measured to $200\frac{m}{s}$ for the 2D case and $260\frac{m}{s}$ for the 3D case. This means that both vorticity and the root mean square velocity is higher in the 3D case compared to 2D. Again, this is the opposite of what was observed during the testing with coarser grid so further conclusions could not be drawn.

The eddies in the turbulence generated through method 3 with large integral length scale, figure 10, are quite different from the others. The large eddies are clear but small scale fluctuations are not discernable. This is due to the use of the low Reynolds number energy spectrum approximation. An estimation of the Kolmogorov length scale commonly used is the one percent limit. The size of the Kolmogorov length scale is where the energy spectrum has reached one percent of its value at the integral length scale. In this case that means

$$\frac{E_\eta}{E_l} = \frac{A \cdot u'^2 \cdot \left(\frac{k_\eta}{2\pi \cdot l^{-1}}\right)^4 \cdot e^{-2\left(\frac{k_\eta}{2\pi \cdot l^{-1}}\right)^2}}{A \cdot u'^2 \cdot \left(\frac{k_l}{2\pi \cdot l^{-1}}\right)^4 \cdot e^{-2\left(\frac{k_l}{2\pi \cdot l^{-1}}\right)^2}} = \\ = \frac{k_\eta^{\,4}}{k_l^{\,4}} e^{\left(\frac{l}{\pi \cdot}\right)^2 \left(k_l^{\,2} - k_\eta^{\,2}\right)} = 0.01 \quad . \tag{89}$$

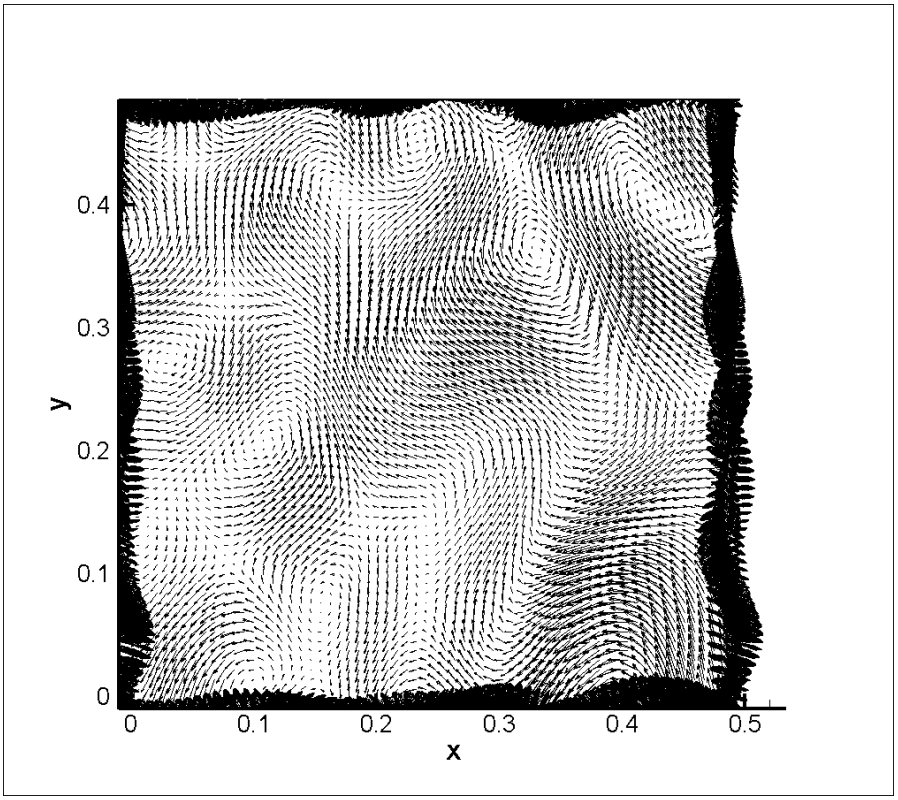

Figure 14. 3D init. turb. field, created through the open source pencil-code. Approximate parameters used are int. length scale of 0.5 mm, turbulent intensity of 50 m/s and grid resolution of 256x256.

An integral length scale of $5\,mm$ gives an integral scale wave number of

$$k_l = \frac{2\pi}{l} = \frac{2\pi}{0.005}\frac{1}{m} \tag{90}$$

and resulting, when put into equation (89), in

$$\frac{k_\eta^{\,4}}{\left(\frac{2\pi}{0.005}\right)^4} e^{\left(\frac{0.005}{\pi\cdot}\right)^2\left(\left(\frac{2\pi}{0.005}\right)^2 - k_\eta{}^2\right)} = 0.01\,. \tag{91}$$

Solving equation (91) numerically yields

$$\begin{aligned} &k_\eta \approx 2040.2098\,\frac{1}{m} \\ &\left[\eta = \frac{2\pi}{k_\eta}\right] \Rightarrow \qquad . \\ &\eta \approx 0.003079\ m \end{aligned} \tag{92}$$

The integral length scale being only about 1.6 times the Kolmogorov length scale clearly indicates that almost all energy is distributed over a very narrow band of large length scales and the small scales barely receives any. Maximum vorticity was measured in the field to $1.88\cdot 10^6\ m^{-1}$ and the maximum root mean square velocity to about $160\ m/s$, which was less than the ones in the 2D and 3D, method 2 generated turbulence cases, but not significant.

The theory described in the previous paragraph is also shown in figure 11. When the integral length scale was decreased, a narrow band of smaller eddies was observed. However, with the low resolution of the visualization, the eddies in this case only shows up as a random noise.

When the high Reynolds number energy spectrum function (52) was used instead, figures 12 and 13, the spectrum of scales became quite different. Comparing figures 10 and 12, it is obvious that a lot of smaller scales are discernable; e.g. the large eddy at coordinates x=0.0048, y=0.0014. In figure 10 that eddy is quite smooth while in figure 12 the small eddies makes it more irregular. The maximum vorticity in figure 12 is about $8\cdot 10^6\ m^{-1}$ which is significantly higher than the one in figure 10. Also the maximum root-mean-square velocity is higher in figure 12; $230\ m/s$ in comparison with $160\ m/s$ in figure 10. Even though the large structures are similar and the visual changes are minor, quantitatively, the vorticity and root mean square velocity differ quite considerably when the energy spectrum is changed.

The same comparison can be made between figures 11 and 13, who are using low Reynolds number and high Reynolds number energy spectrum functions respectively. However, in this case it is almost impossible to observe any differences. Figure 11, with a very narrow band of scales, is already observed as randomly distributed fluctuations on this coarse grid visualization and the adding of more smaller scales is not visible.

If the fields with the small integral scale instead are plotted with high resolution, 1024×1024, and zoomed into one tenth of the actual domain, the exact same conclusions should be able to

be drawn. The plots with energy spectrum (82) and (52) are visualized in figures 15 and 16 respectively. The small scale differences are not as easy to observe as previously, but through detailed comparison between the two, it could be seen that the high Reynolds number energy spectrum contains more small scales.

The pencil-code created turbulence field was plotted after the method described earlier stabilized. The velocity values at the edges are incorrect due to plotting and multiprocessor communication issues. The eddies in that field are larger and contains less small scales than the other methods, so even though the creation process appears more physical and it is much more time consuming, the field does not fulfill the desired properties.

To assure sufficient resolution, the velocity field can be visualized in a 3D plot. For increasing Reynolds numbers, the introducing of smaller scales increases the velocity differences between grid points and beyond a certain level, the resolution can not be considered adequate. Through testing and visualization, this can be seen through the following method. If the resolution is high enough, the velocity field looks smooth, while for too low resolution, the velocity field looks spiky i.e. too large velocity differences between adjacent grid points. For the 256×256 resolution test case, velocity fields for turbulent Reynolds numbers; 10, 50, 100 and 200 are visualized in figures 17, 18, 19 and 20 respectively. Which figures that actually is smooth enough is quite subjective. Clearly, for the Reynolds numbers 10 and 50, the resolution is sufficient and for the Reynolds number 200, it is insufficient. Reynolds number 100 however, is a borderline case. 256×256 resolution is probably not sufficient for Reynolds number 100 but the actual upper limitation is not far below. In the same way, the upper Reynolds number for resolutions 512×512 and 1024×1024 is also estimated. For the 512×512 resolution case, the maximum possible Reynolds number to simulate is approximately 900 and for the 1024×1024 resolution case approximately 2000. The visualization of the 1024×1024 case with turbulent intensity of 218.484 m/s and turbulent Reynolds number of 2000 is shown in figure 21.

3.2. Cases to be studied

As written in section 3.1.6, studies of turbulent cases are governed by simulation limitations. When the cases to be studied were set up for the thin reaction zone regime and the broken reaction zone regime, the requirements were considered according to that section. Theoretically, the highest possible turbulent Reynolds number to simulate is

$$\mathrm{Re}_T \leq N^{4/3}, \tag{93}$$

where N is the number of grid points on the domain width. The resolution requirement is due to that all scales, down to the Kolmogorov scale, must be resolved in a DNS study [22]. The highest possible turbulent Reynolds number to study in a 3D case with approximately 10^6 node points should therefore be around 464. 2D is the alternative, which with the same number of node points corresponds to a maximum turbulent Reynolds number of 10^4. As described in section 3.1.6, the actual upper limits are much lower and not more than half, if that, of the theoretical values should be used.

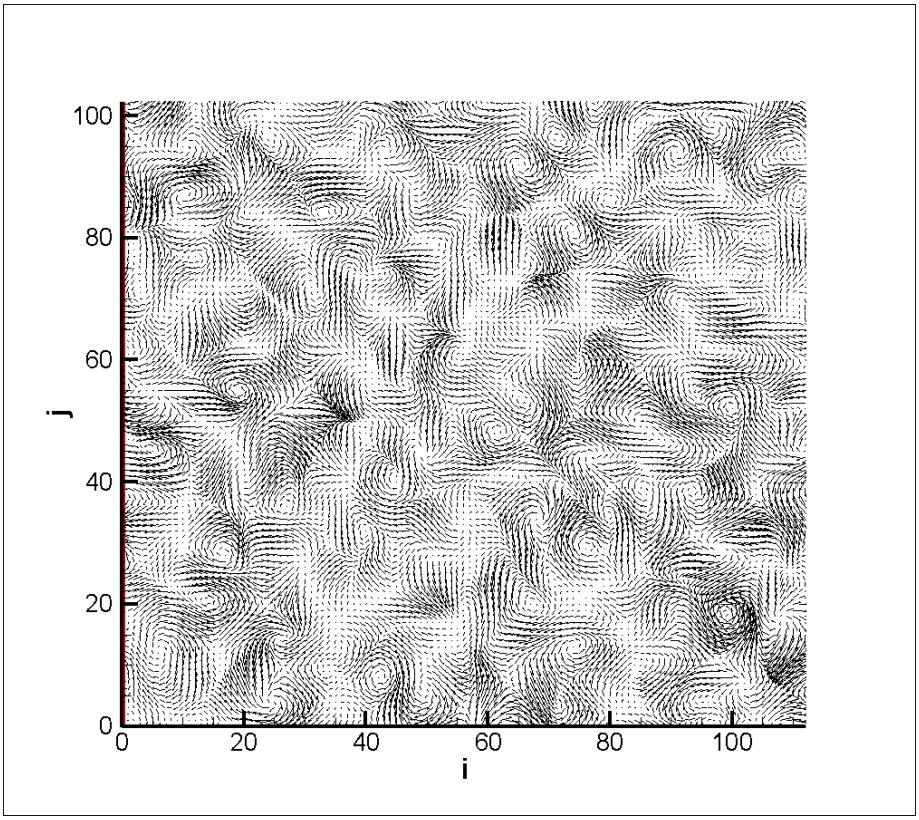

Figure 15. 2D init. turb. field, created through method 3 as described in section 3.1.3 using energy spectrum (82). Parameters used are int. length scale of 0.5 mm, turbulent intensity of 50 m/s and grid resolution of approximately 102x102.

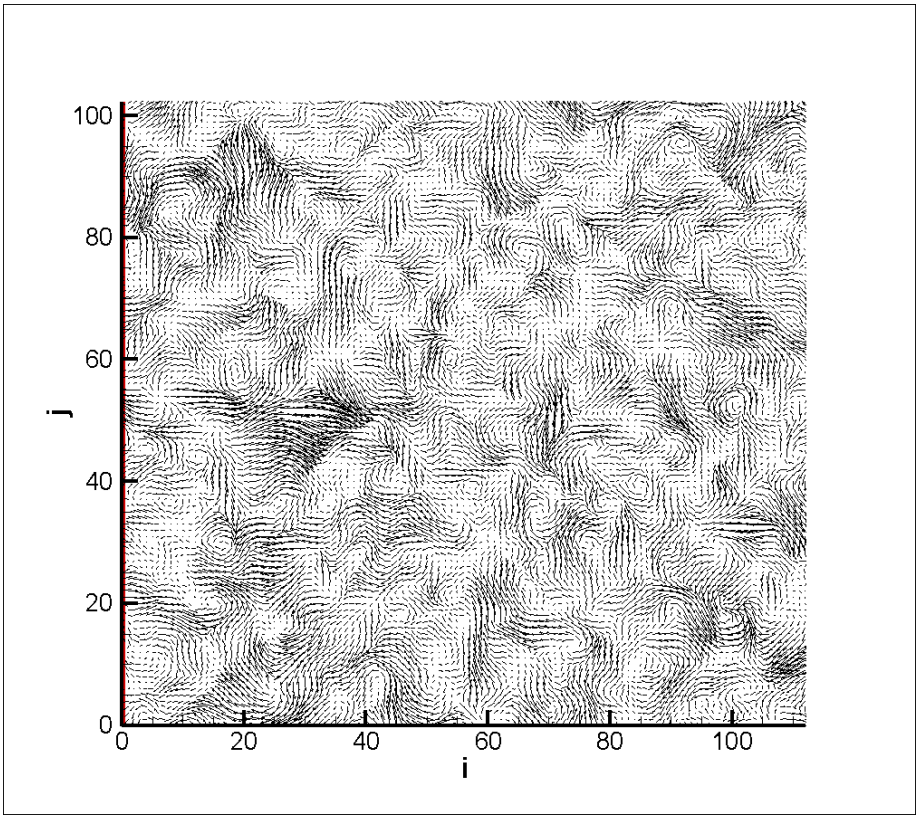

Figure 16. 2D init. turb. field, created through method 3 as described in section 3.1.3 using energy spectrum (52). Parameters used are int. length scale of 0.5 mm, Reynolds number of and grid resolution of 102x102.

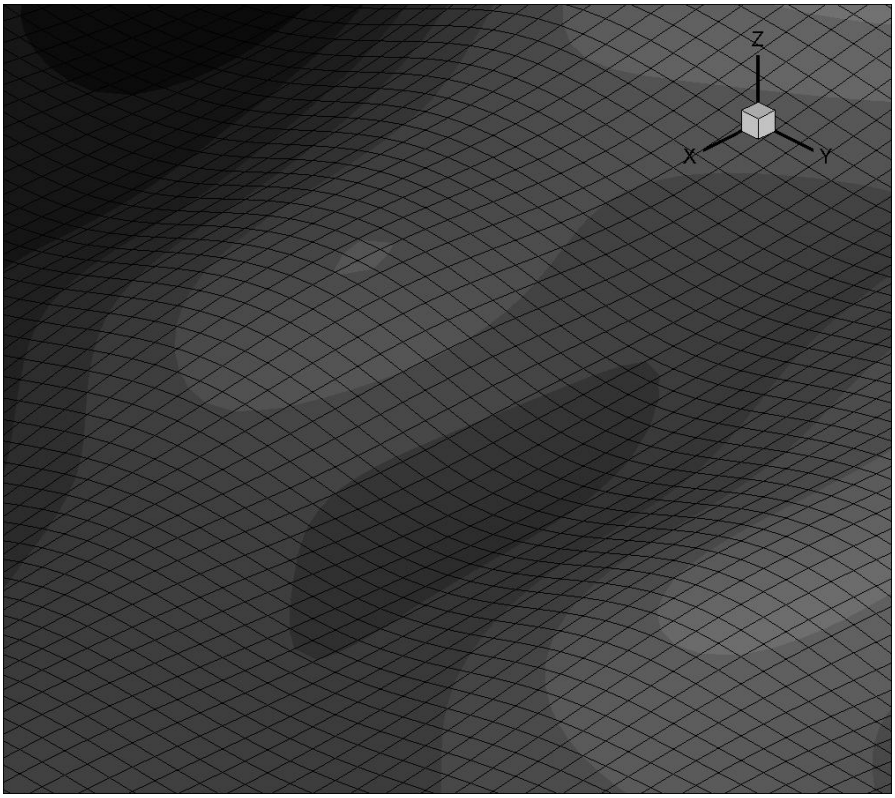

Figure 17. Zoomed plot of the 2D init. turb. field, created through method 3 as described in section 3.1.3 using energy spectrum (52). Parameters used are int. length scale of 5 mm, turbulent intensity of 1.09242 m/s and turbulent Reynolds number of 10.

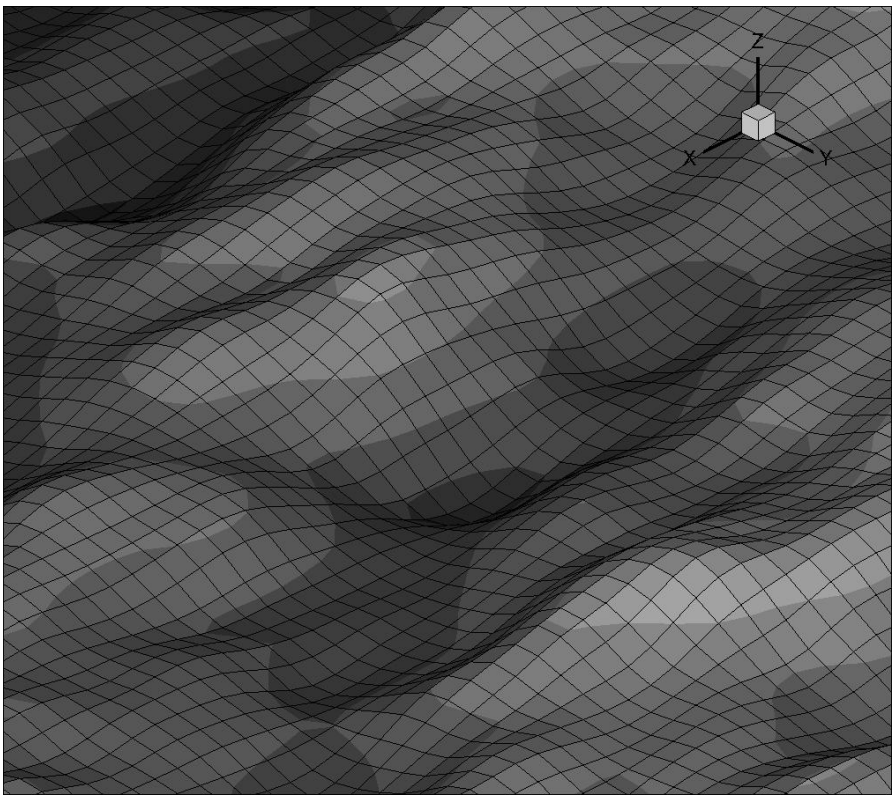

Figure 18. Zoomed plot of the 2D init. turb. field, created through method 3 as described in section 3.1.3 using energy spectrum (52). Parameters used are int. length scale of 5 mm, turbulent intensity of 5.4621 m/s and turbulent Reynolds number of 50.

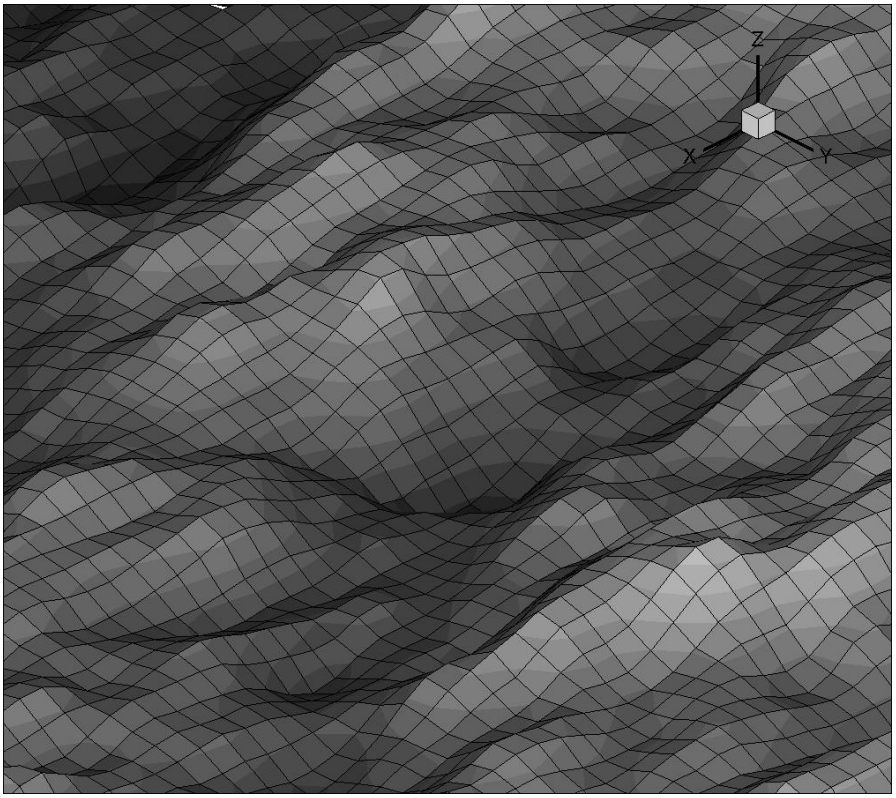

Figure 19. Zoomed plot of the 2D init. turb. field, created through method 3 as described in section 3.1.3 using energy spectrum (52). Parameters used are int. length scale of 5 mm, turbulent intensity of 10.9242 m/s and turbulent Reynolds number of 100.

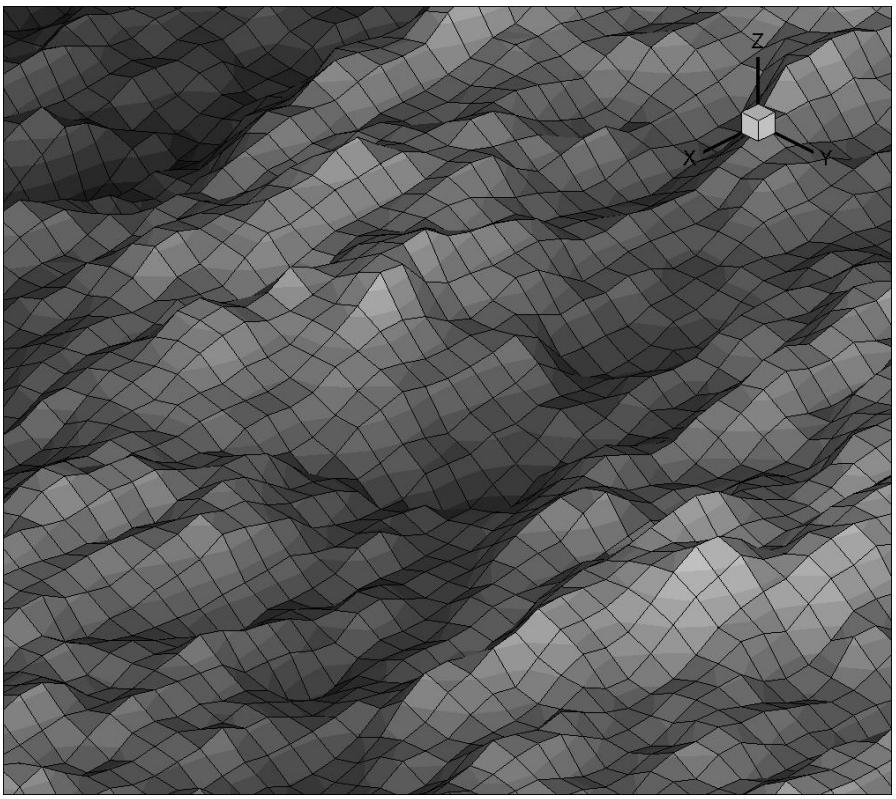

Figure 20. Zoomed plot of the 2D init. turb. field, created through method 3 as described in section 3.1.3 using energy spectrum (52). Parameters used are int. length scale of 5 mm, turbulent intensity of 21.8484 m/s and turbulent Reynolds number of 200.

To resolve the inner structure of the flame front, 20 grid points inside of the reaction zone is required. If the reaction zone thickness is compared to the integral length scale, which is in the same order as the computational domain length, this condition sets an upper limit for the l/δ_l in the Borghi diagram. In the 3D (2D) case, where the number of distributable grid points is 100 (1000) in one direction, this condition limits the calculable domain to $l/\delta_l < 5$ $\left(l/\delta_l < 50\right)$. This means that for l/δ_l higher than 5, a 2D simulation is required.

Six simulation cases were then set up with conditions for possibly relevant scenarios. Lean combustion is a relevant case to study. Low temperature leads to low emissions of e.g. NO_x and it has therefore practical applications. Due to this, the equivalence ratio was set somewhat lower than unity, $\phi = 0.8$, for all cases. The temperature and pressure was set to room temperature and atmospheric pressure, since it is a very common situation. Equal equivalence ratio and pressure for all cases leads to the same laminar flame speed and laminar flame thickness for all studies and the values used are from [32]. To study differences between the thin reaction zone regime and the broken reaction zone regime, the Karlovitz number was set to span over the range of $30 < Ka < 300$. After some minor testing it was realized that the resolution in a 3D simulation was too poor to visualize the desired phenomenon and 2D simulations was selected for all cases. 3D simulation was tested for cases 3 and 4 which are theoretically on the resolution limit since comparison between the Kolmogorov length scale and the cell length gives

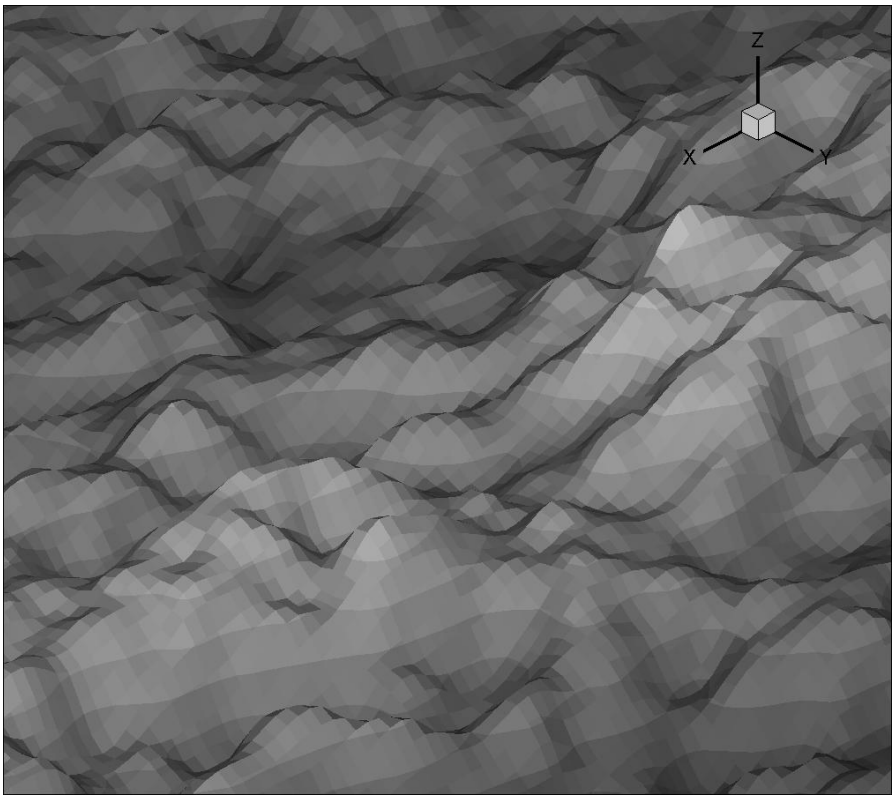

Figure 21. Zoomed plot of the 2D init. turb. field, created through method 3 as described in section 3.1.3 using energy spectrum (52). Parameters used are int. length scale of 5 mm, turbulent intensity of 218.484 m/s, turbulent Reynolds number of 2000 and resolution of 1024x1024.

$$\eta_{case\,3} = \frac{l_3}{Re_{T,\,3}^{\,3/4}} = \frac{0.005}{4 \cdot 100^{3/4}}\, m = 3.953 \cdot 10^{-5}\ m \tag{94}$$

$$\eta_{case\,4} = \frac{l_4}{Re_{T,\,4}^{\,3/4}} = \frac{0.005}{3 \cdot 114^{3/4}}\, m = 4.777 \cdot 10^{-5} m \tag{95}$$

$$\Delta = \frac{L}{\#cells_x} = \frac{0.005}{128} = 3.90625 \cdot 10^{-5} m \tag{96}$$

According to equations (94), (95) and (96), all scales should be possible to resolve, since $\eta_{case\,3}, \eta_{case\,4} > \Delta$. The calculation of the Kolmogorov length scale being a rough estimation makes it uncertain that the smallest scale is resolved for neither of the cases. This makes it doubtful if DNS in fact is used for the 3D simulations. The different cases are listed in Table 1 and marked in the Borghi diagram in figure 22.

Case	1	2	3	4	5	6
ϕ	0.8	0.8	0.8	0.8	0.8	0.8
$T\,(K)$	298	298	298	298	298	298
$p\,(atm)$	1	1	1	1	1	1
$l\,(mm)$	0.1667	0.357	1.25	1.667	2.5	5
$u'\,(m/s)$	33	15.3	50	33	86.8	165.3
Re_T	10	10	114	100	397.92	1512.88
Ka	146.78	31.6	100	46.42	161.56	300
$S_L\,(m/s)$	1.53	1.53	1.53	1.53	1.53	1.53
$\delta_l\,(mm)$	0.357	0.357	0.357	0.357	0.357	0.357
$L\,(mm)$	5	5	5	5	5	5
c_L	0.90	0.90	3.84	2.58	4.40	5.65
c_η	0.67	0.67	0.43	0.47	0.42	0.41

Table 1. Operating conditions for the simulation cases.

3.3. Computational set up

After setting the physical domain length fixed as $5\,mm$ and the integral length scale being varied as parts of the domain length, the initiation of a propagating flame front had to be considered. During early testing it was found that for high intensity turbulence cases, which most of the ones in table 1 are, a thin high temperature region was quickly distributed before ignition and a planar propagating flame was not possible to achieve. To assure quick ignition and propagation before distribution, the hot band was set as broad as half of the domain and with initial temperature of 3500 K. The temperature gradients between the hot and room temperate regions was then lowered by linearly decreasing the temperature over 2.5% of the domain length. This initial temperature distribution was used for all cases except the non-turbulent flame cases. For a non-turbulent flame, it is no risk using a thinner hot band since no turbulence has the possibility of shattering it. An initial high temperature distribution of one fourth of the domain length was therefore used to get a longer propagation and hence also a more accurate laminar flame speed measurement. The initial temperature distribution for the turbulent cases is visualized in figure 23.

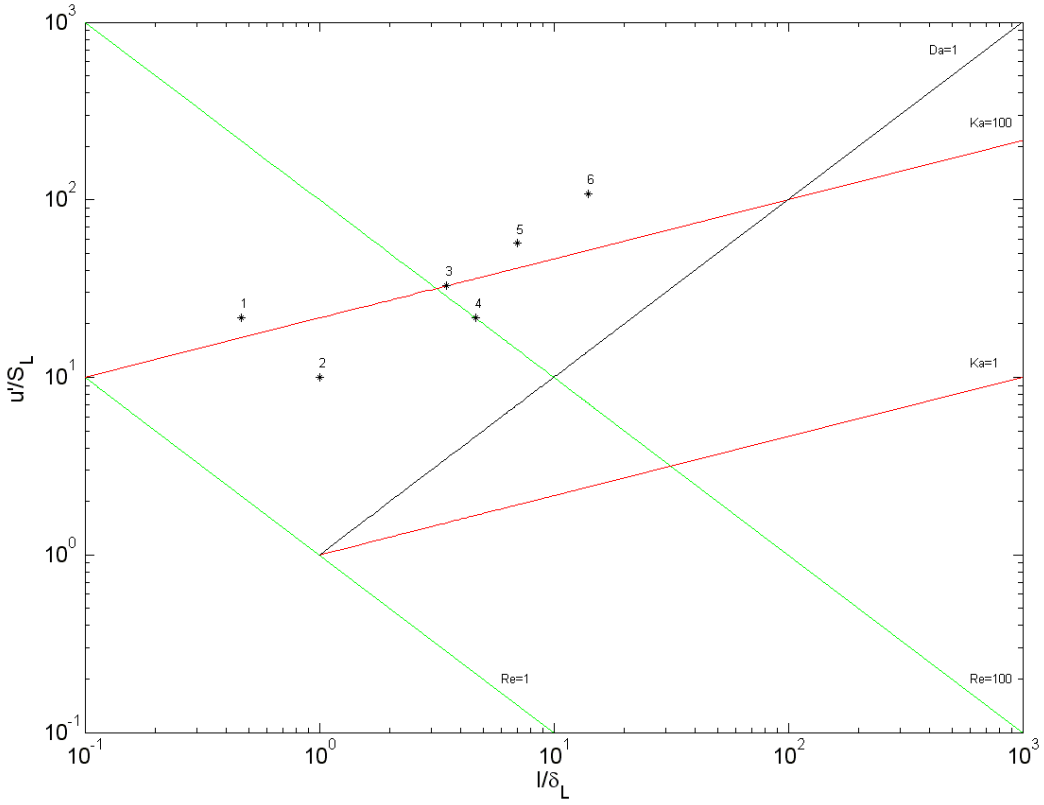

Figure 22. Borghi diagram with the cases to be studied marked out.

4. Results and discussion

In this chapter, results obtained from simulations of the cases described in section 3.2 will be presented and discussed. The flame front is visualized by the species HO_2, since it is created in elementary reactions involving species such as

$$H + O_2 + M \rightarrow HO_2 + M \tag{97}$$

$$HO_2 + H \leftrightarrow H_2 + O_2 . \tag{98}$$

Visualization of the flame turbulence interaction is done by simultaneous plotting of the HO_2 species and the vorticity ω defined as

$$\omega = \nabla \times \vec{u} . \tag{99}$$

For 2D, the vorticity around the z-axis is the interesting part and written as

$$\omega = \frac{\partial v}{\partial x} - \frac{\partial u}{\partial y} . \tag{100}$$

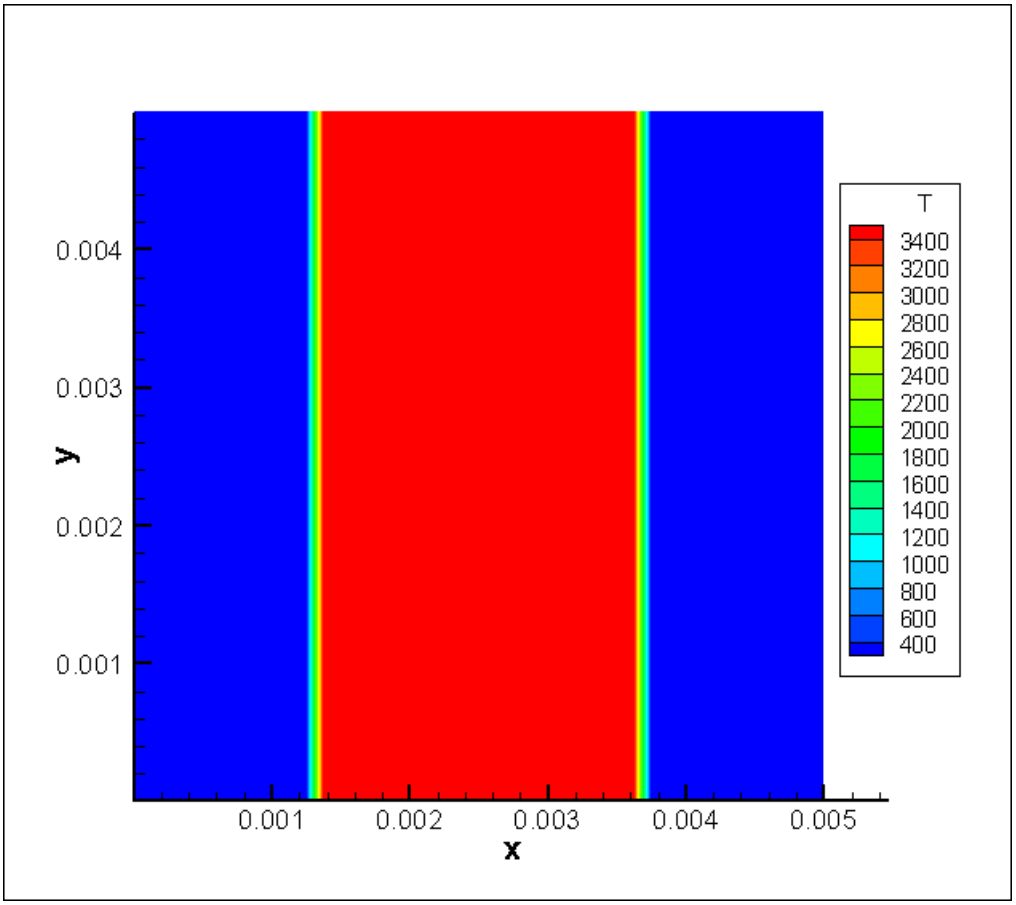

Figure 23. The initial temperature distribution used in all simulation cases.

4.1. 2D simulations

The main results were achieved from the use of 2D simulations for all cases described in section 3.3 with 1024×1024 grid resolution. Quantitatively, the turbulent flame speed and the flame surface density, FSD, were measured.

For both measurements, an exact instantaneous position of the flame front had to be calculated. For this, the normalized distribution of fuel was used. By the change of variable to the reaction progress variable

$$c(x,y,t) = \frac{Y_{fuel,unburned} - Y_{fuel}}{Y_{fuel,unburned} - Y_{fuel,burned}}, \tag{101}$$

the normalized fuel distribution scaled to vary between 0 and 1 approximately was given. The ensemble mean of it was obtained through the integration in the homogeneous direction y

$$\bar{c}(x,t) = \frac{1}{L_y}\int c(x,y,t)dy, \tag{102}$$

and the mean flame front location was then defined to be located at a fix value of the mean normalized distribution of fuel. Due to pocket formation for the highest turbulent intensity cases, the fixed value was chosen to be low to avoid disturbances from the pockets. The value

$$\bar{c}(x,t) = 0.25 \tag{103}$$

was used. For each time step, the flame front speed relative to fixed coordinates, S^*, was calculated by

$$S^* = \frac{x\big|_{\bar{c}(x,t+\Delta t)=0.25} - x\big|_{\bar{c}(x,t)=0.25}}{\Delta t}. \tag{104}$$

According to continuity equation relative S^*, the flow speed in the unburned mixture, u_u, would be

$$\begin{aligned} &\rho_u(u_u - S^*) = \rho_b(u_b - S^*) \\ &\qquad\Leftrightarrow \qquad\qquad , \\ &u_u = \frac{\rho_b}{\rho_u}u_b + \left(1 - \frac{\rho_b}{\rho_u}\right)S^* \end{aligned} \tag{105}$$

where ρ_u is the density on the unburned side, ρ_b is the density on the burned side and u_b is the flow speed in the burned mixture. S^* being positive, equation (104) means that u_u also is positive since

$$\rho_b < \rho_u. \tag{106}$$

To acquire the flame speed relative to unburned mixture, u_u has to be subtracted from S^*, i.e.

$$S = S^* - u_u . \tag{107}$$

The FSD was determined by first measuring the length of the flame front in each computational cell. The reaction progress variable in each cell was distributed to the adjacent node points and by calculation of the intersections of the flame front with the cell border through linear interpolation, the flame front length was calculated by the use of the Pythagorean Theorem. This also requires the assumption of a linear flame front within each cell. The FSD variable Σ in cell i, j was then calculated by

$$\Sigma(i, j) = \frac{l_{i,j}}{\Delta x \cdot \Delta y}, \tag{108}$$

where $l_{i,j}$ is the flame front length in cell i, j and Δx and Δy is the cell sizes in the x and y directions, respectively. The FSD average over the homogenous direction along the flame front is then calculated by

$$\bar{\Sigma}(i) = \frac{1}{N_J} \sum_{j=1}^{N_J} \Sigma(i, j). \tag{109}$$

4.1.1. Laminar flame

As an extra comparison case, simulation of laminar flames was performed. As mentioned in section 3.3, for a laminar flame (non-turbulent) there is no risk of shattering of the flame front and the width of the hot ignition region was therefore set as one fourth of the domain instead of half for the turbulent cases. This is to acquire a longer distance of propagation and therefore also a better stabilized value. Time evolution of the propagating HO_2 layer for a laminar flame at atmospheric pressure is visualized in figure 24.

Equations (101-103) were used when defining the instantaneous flame front. S_L^* was then calculated through equation (104) and visualized in figure 25 with the values of the left flame front displayed with stars and the values of the right flame front displayed with circles. Figure 25 shows a monotonic decrease, which is due to the pressure difference during earlier flame ignition. The mean flow velocity at the initial state was set to be zero. However, as it is shown below that as the flame propagates, the velocity field is altered. A mean flow velocity, u_u, defined at $\bar{c} = 0.25$ and averaged in the homogenous direction is calculated. u_u was calculated at each time and visualized in figure 25 with the values of the left flame front displayed with triangles and the values of the right flame front displayed with plus signs. Initially, due to ignition disturbances, the characteristics of the flame speed and the flow velocity is very different, but after some time the difference between the two velocities becomes stationary. The laminar flame speed was therefore estimated as the difference between the flame transportation speed and the flow velocity as

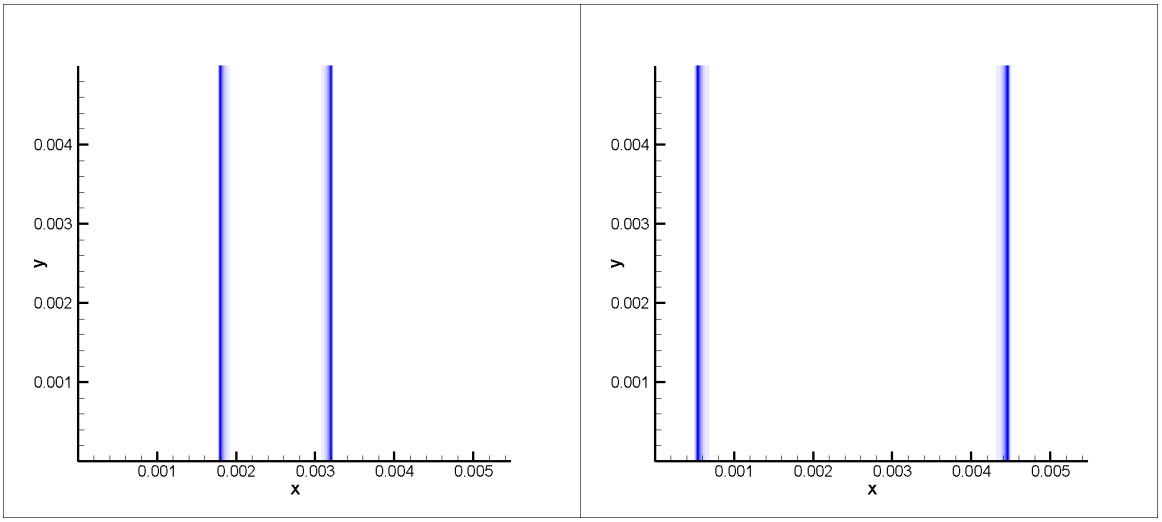

Figure 24. Time sequence of the propagation of the HO_2 layer for a non-turbulent flame. The frames corresponds to the elapsed times of $6.3065\,\mu s$ and $152.208\,\mu s$ respectively.

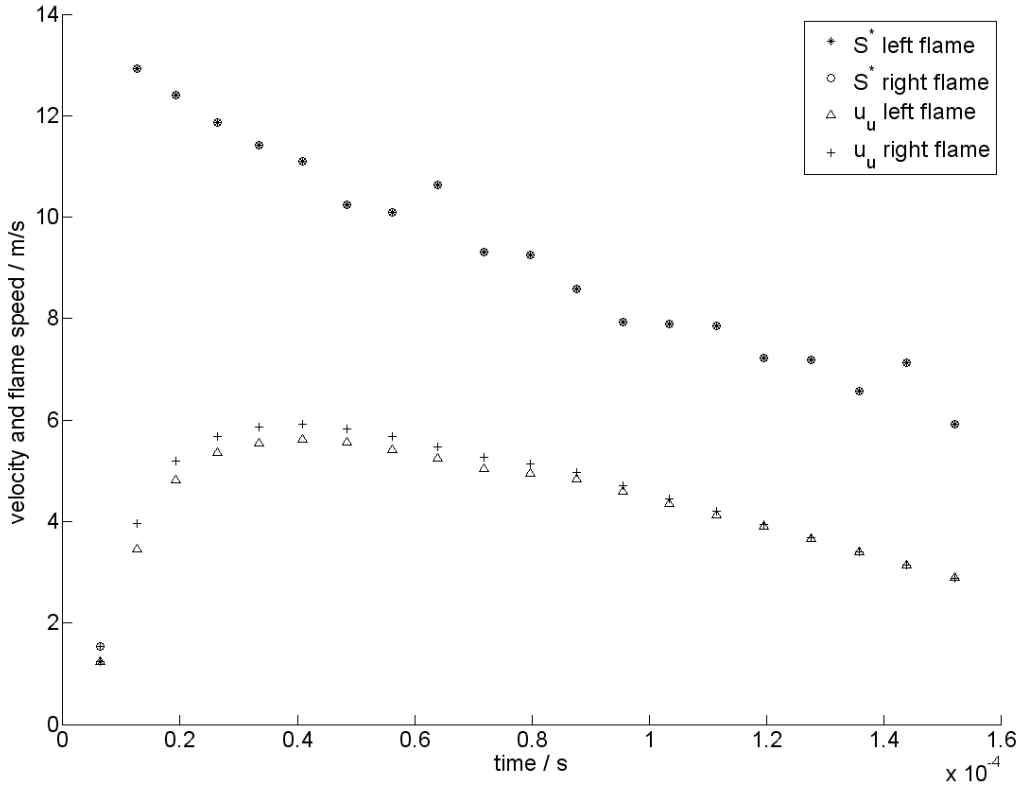

Figure 25. S_T^* for the laminar flame displayed as stars and circles and u_u at the flame front position displayed as triangles and plus signs for the left and right flame front respectively.

$$S_L = S_L^* - u = 5.923 - \frac{2.9 + 2.8785}{2}\frac{m}{s} \approx 3.034\frac{m}{s}. \quad (110)$$

The experimental measurement of the flame speed, and hence also the value of the flame speed used in the calculations of the turbulent Reynolds numbers, is $1.53\frac{m}{s}$ [32] and therefore about half the one calculated in this laminar flame case. This difference might be due to the use of constant volume and a very small propagation distance.

For future comparison, the thickness of the preheat zone was also measured. The preheat zone was assumed to last from approximately $350\ K$ to the ignition temperature. The ignition temperature is the temperature where the chain branching reaction

$$H + O_2 \rightarrow O + OH \quad (111)$$

is faster than the chain terminating reaction (97). The rate of the reactions is given by the Arrhenius expression (13), which for reactions (110) and (97) reads [33]

$$\frac{d[OH]}{dt} = [H]\cdot[O_2]\cdot 1.94\cdot 10^{14}\cdot e^{-\frac{68.78}{R\cdot T}} = X_H \cdot X_{O_2}\cdot 1.94\cdot 10^{14}\cdot e^{-\frac{68.78}{R\cdot T}}\cdot\left(\frac{p}{RT}\right)^2 \quad (112)$$

$$\frac{d[HO_2]}{dt} = [H]\cdot[O_2]\cdot[M]\cdot 6.7\cdot 10^{19}\cdot T^{-1.42} = X_H \cdot X_{O_2}\cdot X_M \cdot 6.7\cdot 10^{19}\cdot T^{-1.42}\cdot\left(\frac{p}{RT}\right)^3 . \quad (113)$$

The mole fraction X_M is one and the mole fractions of the other species does not influence the cross-over temperature since they are the same for both expressions. Figure 26 shows the rate of species concentration as function of temperature and the crossover temperature is found to be about $980\ K$.

The temperature field was then plotted and displayed in figure 27 with only three temperature stages; 300, 350 and 980, making the preheat zone clearly visualized. Figure 27 also shows the distribution of species H, O, OH, HO_2 and H_2O_2. The thickness of the preheat zone, δ_p, was measured from figure 27 and calculated as

$$\delta_p = 0.00391987 - 0.00383118\,m \approx 88.7\,\mu m. \quad (114)$$

This calculation along with the estimation of the Kolmogorov length scale, (72), yields that the smallest length scale is smaller than the laminar thickness of the preheat zone for all cases. Due to this, broadening of the preheat zone is expected to occur in all cases. The distribution of radicals, H, O and OH has differences in mass fraction but similar profiles. Their values in the preheat zone is low and then gradually increases through the reaction zone. The HO_2 species is mainly centered in the preheat zone and deceases closer to and through the reaction zone. This is due to that the reaction rate of HO_2 is mainly controlled by low temperature reactions such as (97), and due to the low concentration of radicals, the reverse reactions of (98) and (115).

$$HO_2 + OH \leftrightarrow H_2O + O_2 \tag{115}$$

A low concentration of OH, makes the reverse reaction of equations (116) and (117) quite insignificant.

$$HO_2 + H \leftrightarrow OH + OH \tag{116}$$

$$HO_2 + O \leftrightarrow OH + O_2 \tag{117}$$

The distribution of H_2O_2 is quite similar to the distribution of HO_2, except that it does not decrease as rapidly in the reaction zone and post-flame zone as HO_2. This is due to that the rate of formation of H_2O_2 is only governed by reactions involving either HO_2 or radicals. The highest concentration of H_2O_2 is therefore found in the preheat zone, where the concentration of HO_2 is high and the concentration of radicals is low. The rate of H_2O_2 is therefore mainly controlled by reactions (118), (119) and (120).

$$HO_2 + HO_2 \leftrightarrow H_2O_2 + O_2 \tag{118}$$

$$H_2O_2 + H \leftrightarrow H_2 + HO_2 \tag{119}$$

$$H_2O_2 + OH \leftrightarrow H_2O + HO_2 \tag{120}$$

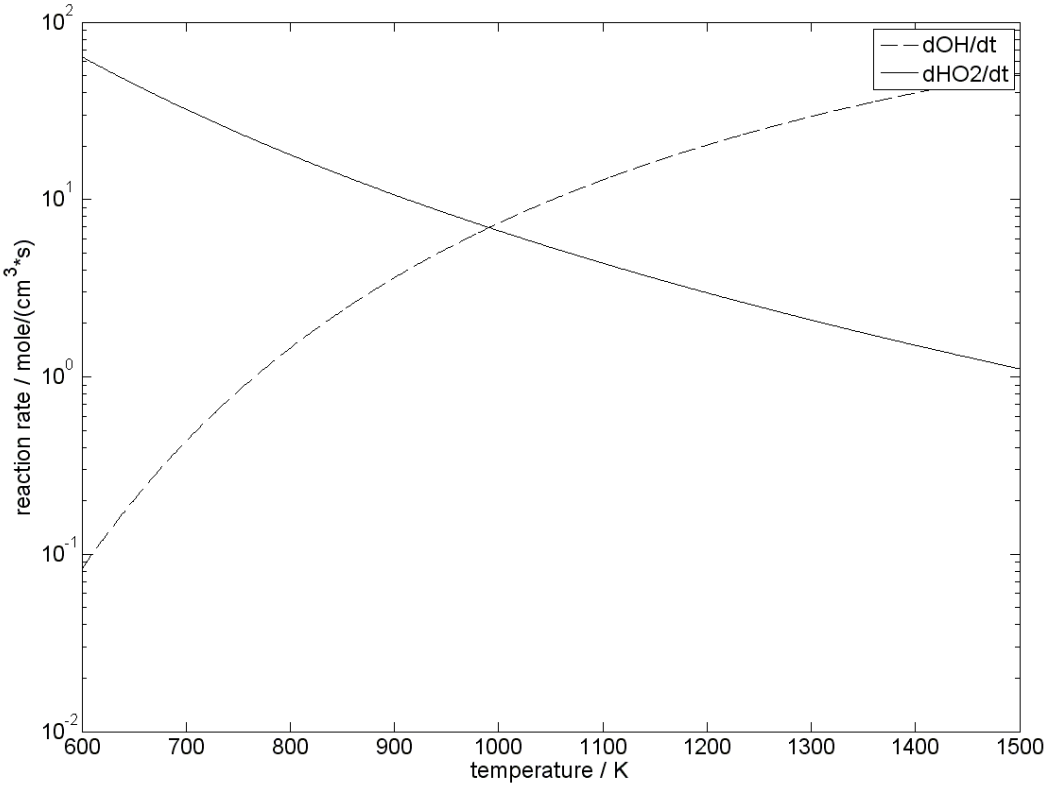

Figure 26. The reaction rate of species OH and HO_2 plotted against temperature. The intersection is at approximately $980\,K$.

When the concentration of HO_2 decreases through the reaction zone, the rate of H_2O_2 is kept up by the increased concentration of OH through the reverse reactions in equations (121), (122) and (123).

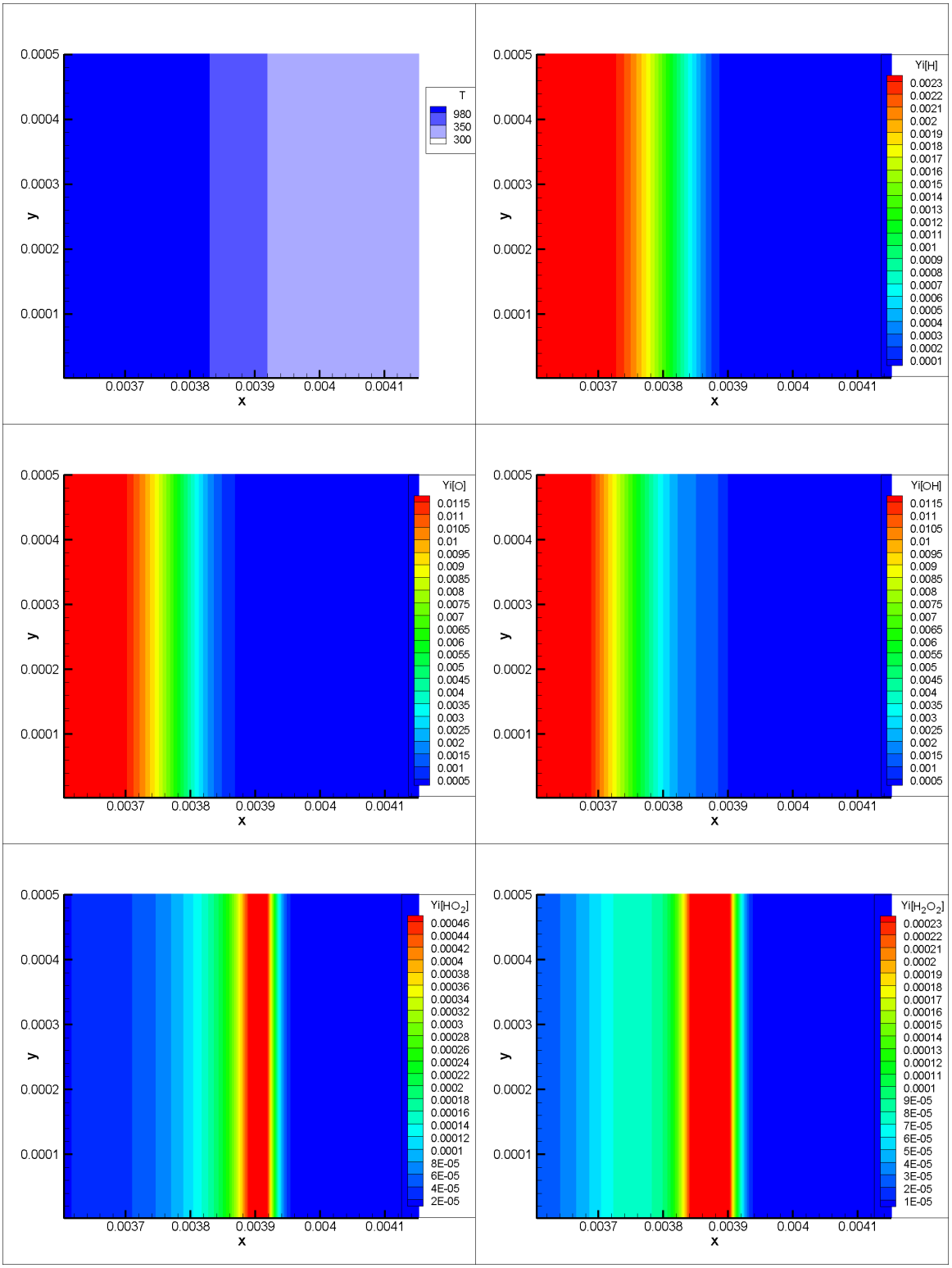

Figure 27. Magnified visualization of the preheat zone for a stationary propagating laminar flame. The frames correspond to the preheat zone and distribution of species; H, O, OH, HO_2 and H_2O_2 respectively.

$$H_2O_2 + M \leftrightarrow +OH + OH + M \tag{121}$$

$$H_2O_2 + H \leftrightarrow H_2O + OH \tag{122}$$

$$H_2O_2 + O \leftrightarrow OH + HO_2 \tag{123}$$

A simulation of a laminar flame at 30 atmospheres pressure was also performed and the position of the HO_2 layer at times $85.8223\mu s$, $98.0061\mu s$ and $116.221\mu s$ along with a zoomed figure of the HO_2 layer at $116.221\mu s$ are visualized in figure 28. At this pressure the flame front is much thinner than at atmospheric pressure and some minor wrinkling starts approximately at time $85.8223\mu s$. It later enhances and at time $116.221\mu s$, the wrinkling is severe. Wrinkling of a laminar flame at high pressure is due to the non-unity Lewis number. Lewis number is the ratio between thermal and mass diffusivity and when it is non-unity, the mixture is not homogenously premixed. When the flame thickness becomes smaller, due to

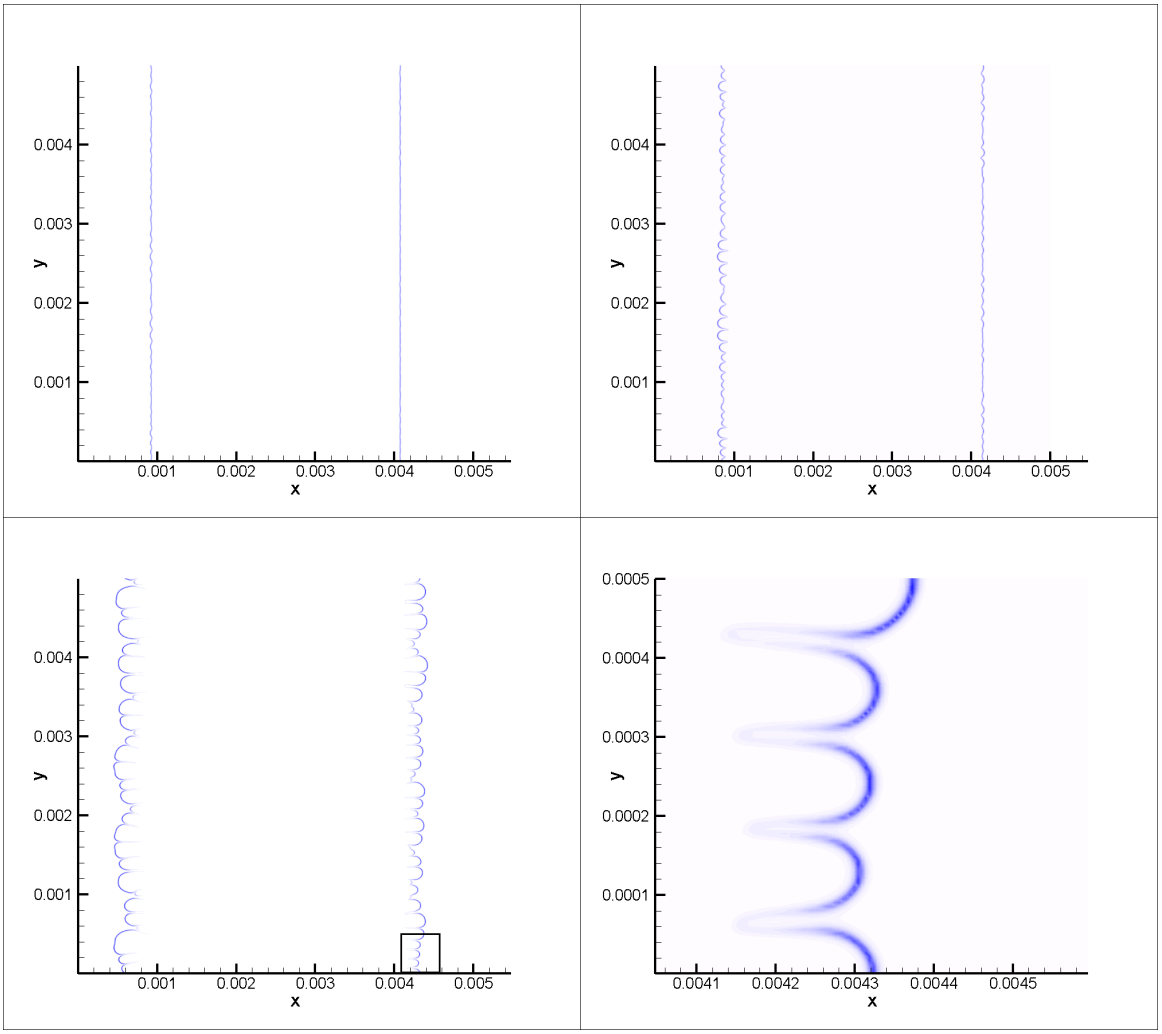

Figure 28. The HO_2 layer for a non-turbulent flame with 30 atmospheres pressure. The first three frames corresponds to the elapsed times of $85.8223\mu s$, $98.0061\mu s$ and $116.221\mu s$ respectively and the fourth frame shows a zoomed image of the lower right corner of the HO_2 at $116.221\mu s$.

high pressure, the flame becomes more responsive to the disturbances of the diffusive-thermal effect, the non-unity Lewis number effect.

4.1.2. Case 1 in 2D

Although the turbulent Reynolds number of case 1 is low, the Karlovitz number is very high. This is due to the high turbulent intensity in comparison with the very small integral length scale. In theory, inner flame region disturbance is expected for this case at the same time as the large structures of the flame front should be left with minor distortion. The turbulent flame speed is also in large extent connected to the degree of which the large scales of the flame are perturbed. A time sequence of the propagation of the HO_2 species layer along with vorticity is shown in figure 29.

The first frame in the sequence of figure 29 shows the vorticity of the initial turbulence field and is clearly governed by very small scales. The second frame in the sequence, which is close to ignition, clearly shows the very minor large scale distortion. In the unburned gas region, the dissipation of the smallest scales is already severe and due to the raise of the viscosity in the unburned gases, a large amount of the turbulence was extinguished in the hot region. In the third and fourth frame it can be seen how the initial minor wrinkling of the flame is enhanced by the diffusive thermal effect and the Darrieus-Landau effect and eventually stabilizes. Due to the use of constant volume and the fact that the remaining eddies in the unburned gas eventually are being crushed between flame fronts, time steps beyond the fourth frame will for sure not provide any additional knowledge about the desired observations.

Through the same method as described in section 4.1.1, the preheat zone and vorticity was visualized in figure 30 in a zoomed frame of the lower right part of the second frame in figure 29 i.e. at time $47.73701\mu s$. Figure 30 also shows the distribution of species H, O, OH, HO_2 and H_2O_2 respectively at the same time and position as the preheat zone frame.

The first frame in figure 30 clearly shows the broadening of the preheat zone by turbulent eddies. The distribution of radicals is very similar to the one observed in the laminar case. Apart from wrinkling, a minor disturbance in the OH distribution is discernable. When a preheat zone broadened by turbulent eddies is observed it becomes clear that the distributions of HO_2 and H_2O_2 is a good indicator of the preheat zone. They are the only ones of the observed species that are affected by the preheat zone broadening and follows the contour of it very well. Measurements also shows that the concentration of species HO_2 and H_2O_2 in the turbulent case is increased where the preheat zone is concave and decreased where it is convex, compared to the laminar case.

S_T^* was estimated through the method described in section 4.1 and plotted as a function of time in figure 31 with the values of the left flame front displayed with stars and the values of the right flame front displayed with circles. In the same figure, u_u at the flame front position is visualized with the values of the left flame front as triangles and the values of the right

flame front with plus signs. Both S_T^* and u_u are considered to be stabilized in the interval between times $18.9352\,\mu s$ and $66.7438\,\mu s$. After time $66.7438\,\mu s$, the wrinkling of the two flame fronts became quite different, as can be seen in figure 29, which also makes the flame speed evolve in different directions. The turbulent flame speed was therefore estimated as the mean of the stabilized values i.e.

$$S_{T,case1} = \frac{\sum_{j=4}^{14} S_{T,1,j}^* - u_{1,j} + \sum_{j=4}^{14} S_{T,2,j}^* - u_{2,j}}{2 \cdot 11} = 6.07 \frac{m}{s}. \tag{124}$$

The FSD was calculated for times $4.73701\,\mu s$ and $96.3255\,\mu s$ and plotted in figures 32 and 33 to visualize the difference in wrinkling for the two flame fronts. As expected from the results during the calculation of the flame speed, it in the FSD figures becomes clear that the left flame front is much more wrinkled than the right one. Ideally, the distribution of flame surface density should be continuous and expected, if overstated a bit, to be formed as a triangle. The FSD at early time seems to be well fitting to that description, due to very little

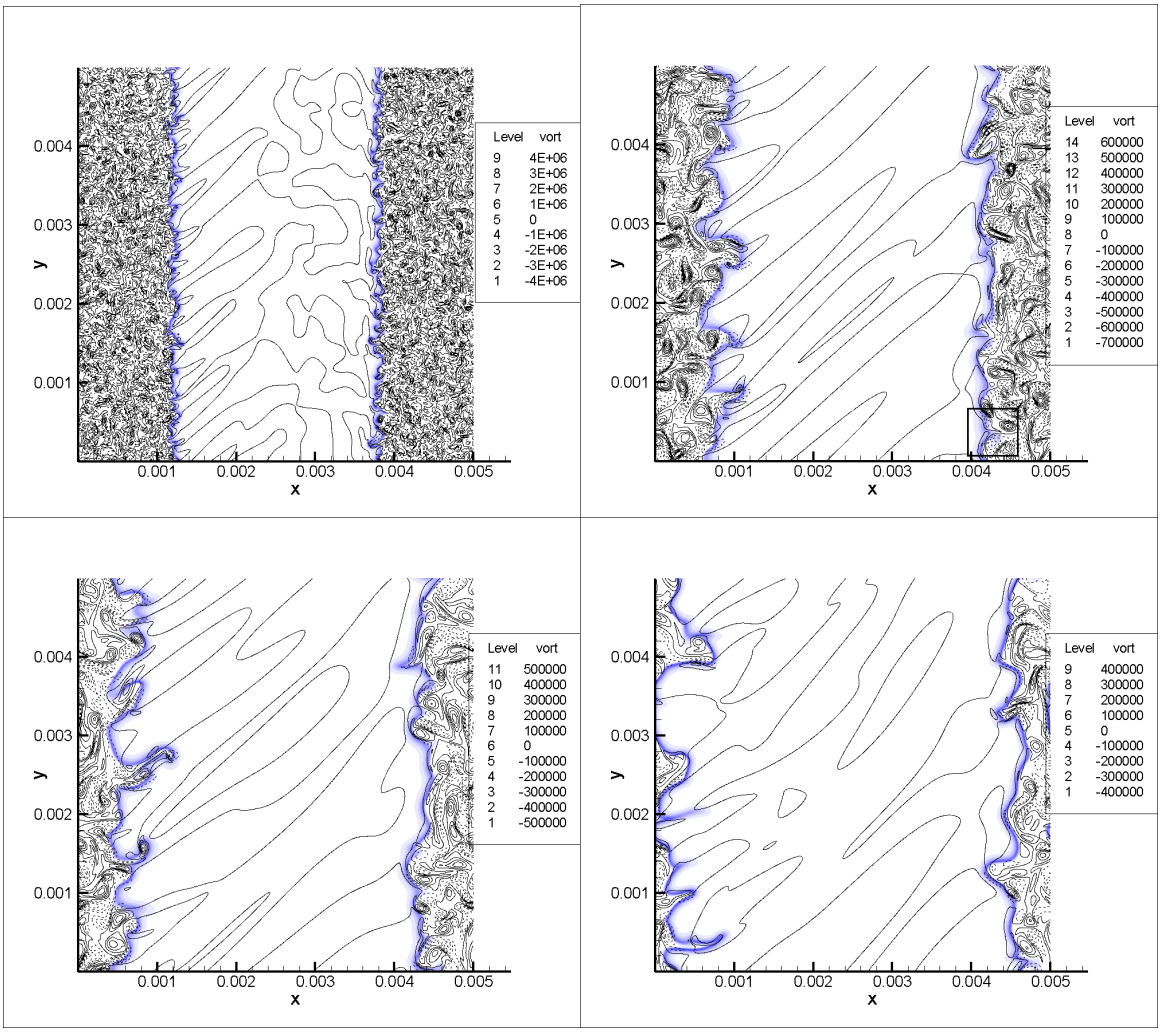

Figure 29. Time sequence of the HO_2 layer propagation along with vorticity for case 1. The frames corresponds to the elapsed times of $4.73701\,\mu s$, $47.407\,\mu s$, $66.7438\,\mu s$ and $96.3255\,\mu s$ respectively.

wrinkling. At later time however, the wrinkling becomes large and a big part of the domain length, which makes it statistically impossible to get a well distributed FSD. The statistics and the shape of the distribution should become better if the domain was larger.

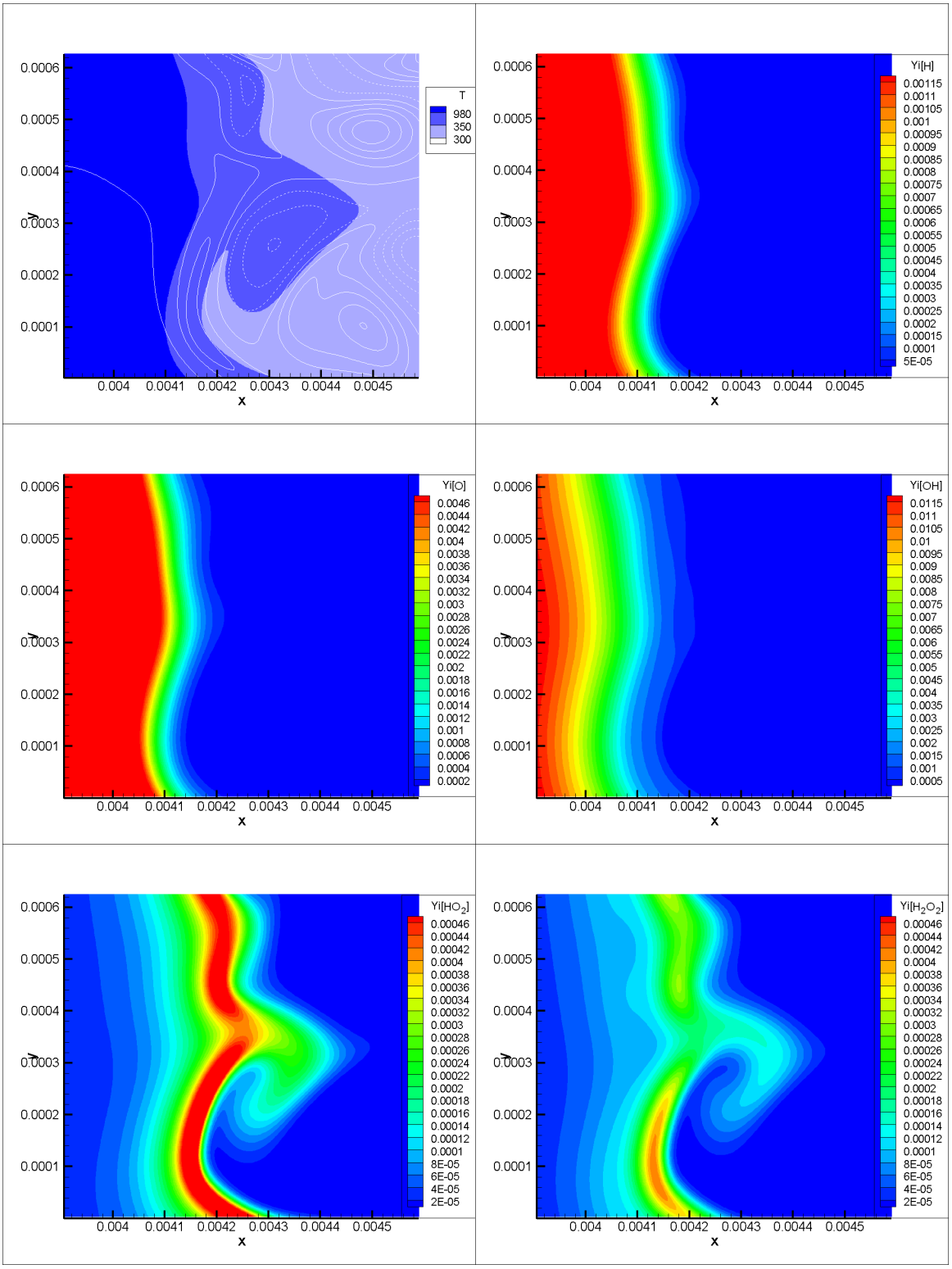

Figure 30. Visualizations at time 47.407 μs for zoomed figures of the preheat zone along with vorticity and distribution of species; H, O, OH, HO_2 and H_2O_2 for the frames respectively. The zoomed area is also marked in figure 29, frame 3.

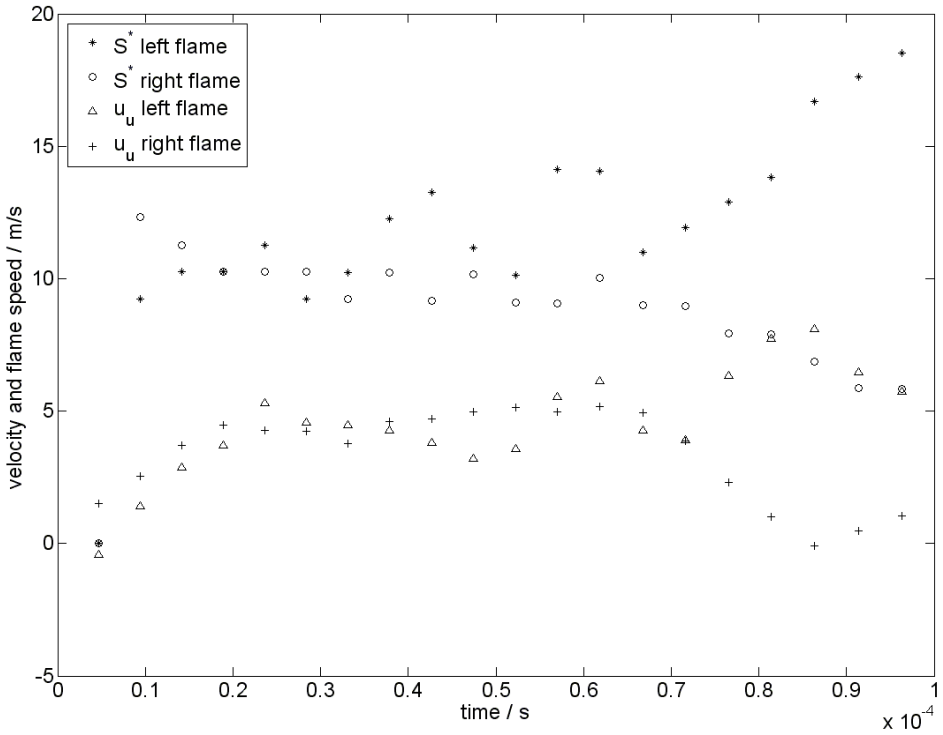

Figure 31. S_T^* for case 1 displayed as stars and circles and u_u at the flame front position displayed as triangles and plus signs for the left and right flame front respectively.

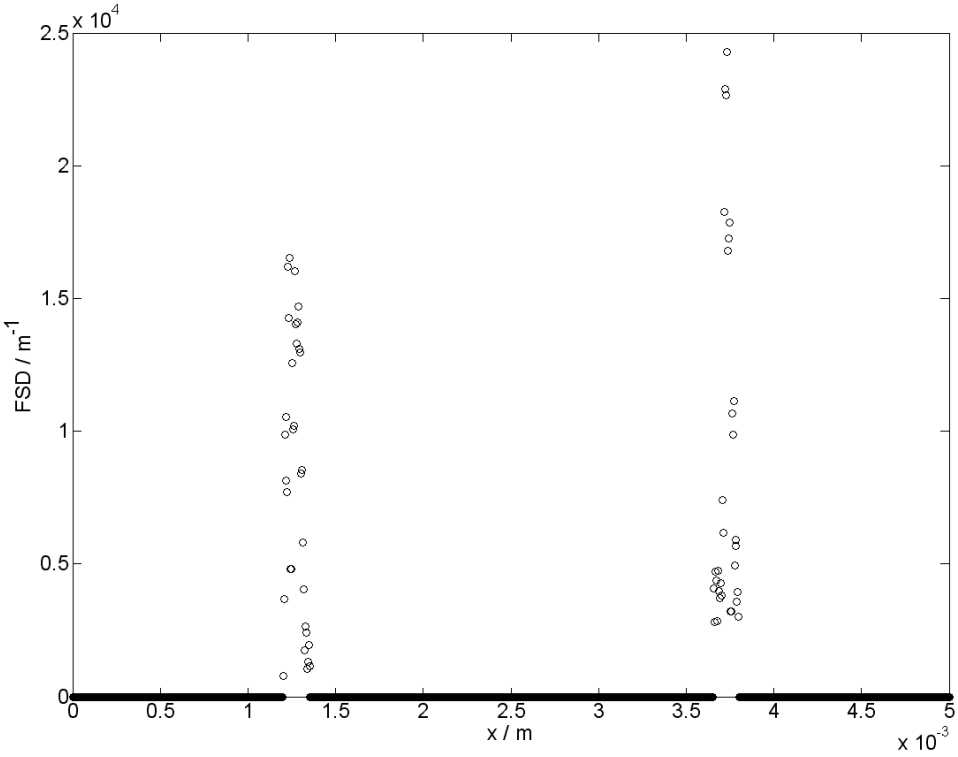

Figure 32. FSD for case 1 over the domain width at time $4.73701\,\mu s$.

4.1.3. Case 2 in 2D

The second case is similar to the first in the sense that the integral length scale is small compared to the length of the domain. The Reynolds numbers are identical, which is achieved by approximately setting the turbulent intensity to half the one in case 1. These changes in conditions make the Karlovitz number drop significantly and end up in about one fourth of the one in case 1. The flame is in the thin reaction zone region and inner flame region distortion is therefore not expected. The phenomenon that should be able to discern are instead broadening of the pre heat zone and higher rate of large scale distortion of the flame than in case 1. A time sequence of the propagation of the HO_2 species layer along with vorticity is shown in figure 34. Like in case 1, the large scale wrinkling seems much more severe for the left flame front than the right.

S_T^* was estimated through the method described in section 4.1 and plotted as a function of time in figure 35 with the values of the left flame front displayed with stars and the values of the right flame front displayed with circles. In the same figure, u_u at the flame front position is visualized with the values of the left flame front as triangles and the values of the right flame front with plus signs. Both S_T^* and u_u are considered to be stabilized in the interval between times $18.9478\,\mu s$ and $71.7868\,\mu s$. After time $71.7868\,\mu s$, the wrinkling of the two flame fronts became quite different, as can be seen in figure 34, which also makes the flame speed evolve in different directions. The turbulent flame speed was therefore estimated as the mean of the stabilized values i.e.

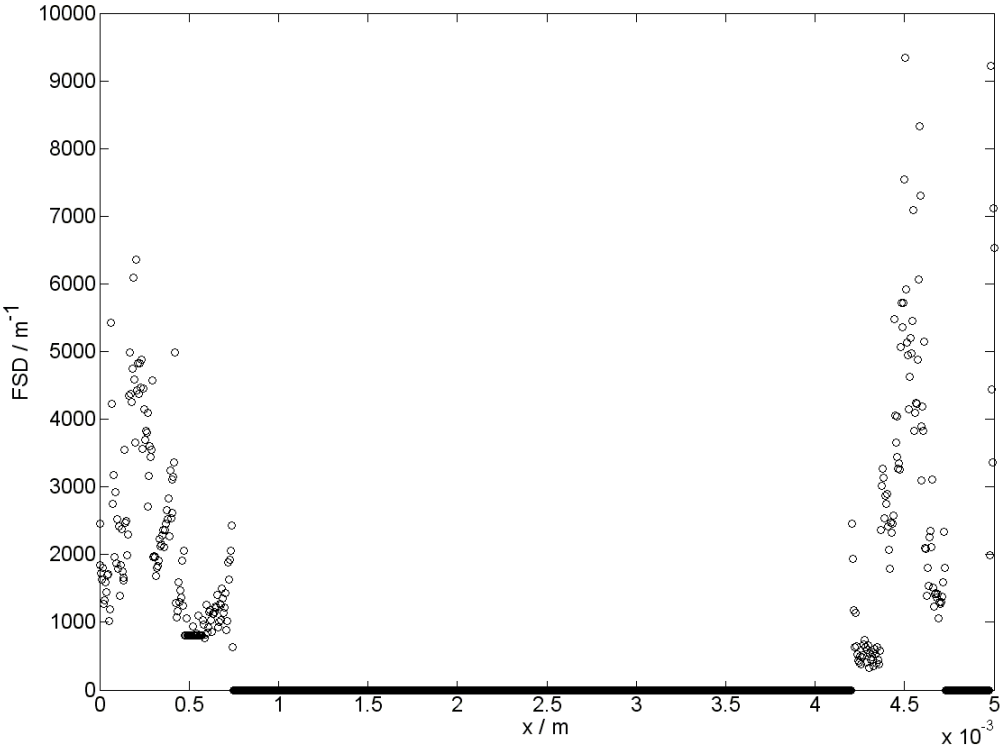

Figure 33. FSD for case1 over the domain width at time $96.3255\,\mu s$.

$$S_{T,case2} = \frac{\sum_{j=4}^{15} S^*_{T,1,j} - u_{1,j} + \sum_{j=4}^{15} S^*_{T,2,j} - u_{2,j}}{2 \cdot 12} = 5.82 \frac{m}{s}. \quad (125)$$

The FSD was calculated for time $96.307\,\mu s$ and plotted in figure 36 to visualize the difference in wrinkling for the two flame fronts. Just as in case 1, the degree of wrinkling of the left flame front is higher than the one of the right flame front. As can be seen at the end of figure 35, the more severe wrinkling of the left flame front in comparison to the right one makes the flame speed higher and allows the left flame front to travel longer, making its position in figure 36 closer to the boundary.

The absolute value of the vorticity in the burned region was calculated, averaged and plotted as a function of time in figure 37. The vorticity in the burned region of the flame is both consisting of non dissipated turbulence from the initial field and flame generated turbulence due to baroclinic torque. Initially, the measured vorticity is zero since there is no burned side. Shortly after ignition, the vorticity in the center region was quickly lowered due to the

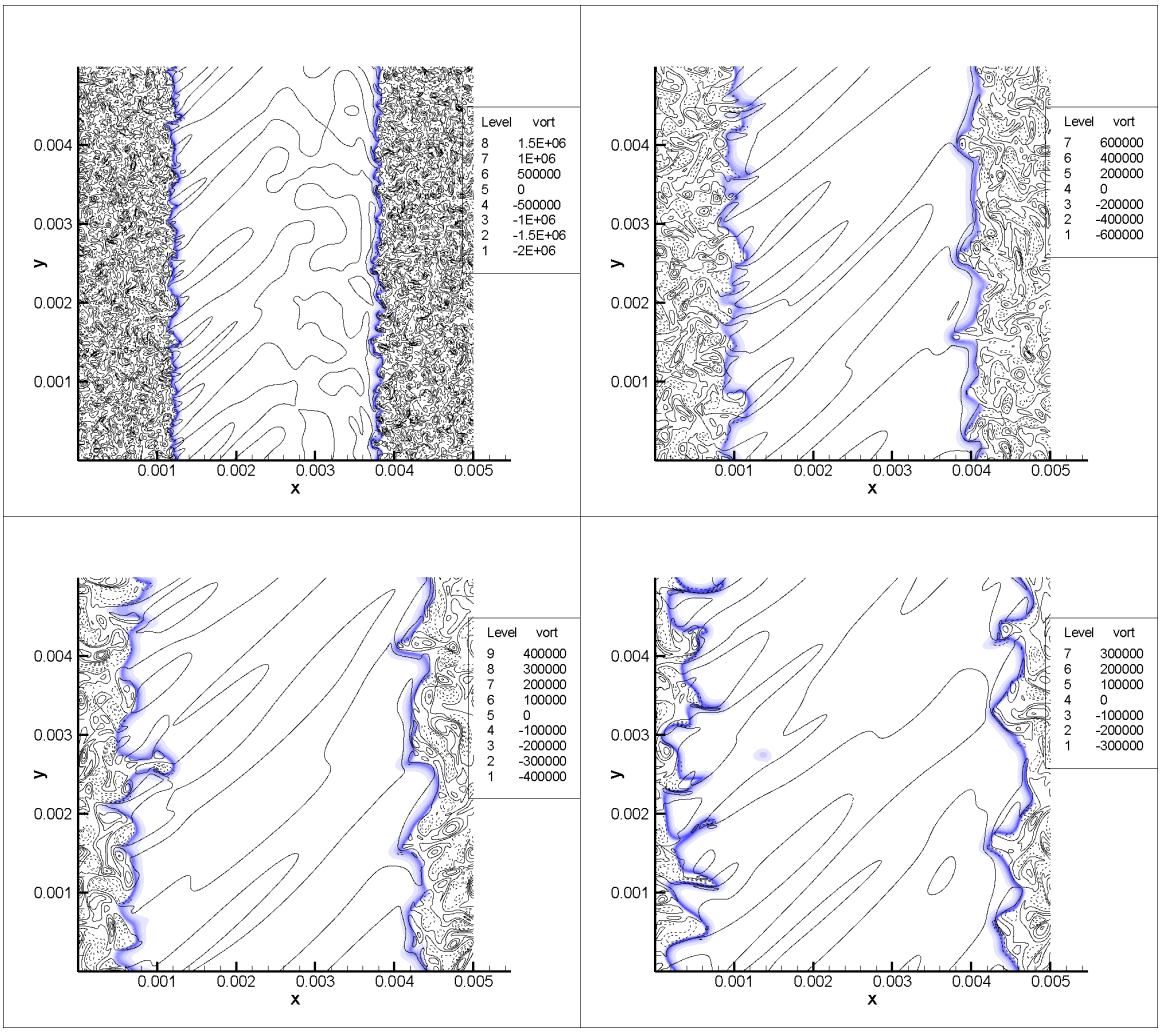

Figure 34. Time sequence of the HO_2 layer propagation along with vorticity for case 2. The frames corresponds to the elapsed times of $4.7382\,\mu s$, $28.4307\,\mu s$, $61.8683\,\mu s$ and $91.3239\,\mu s$ respectively.

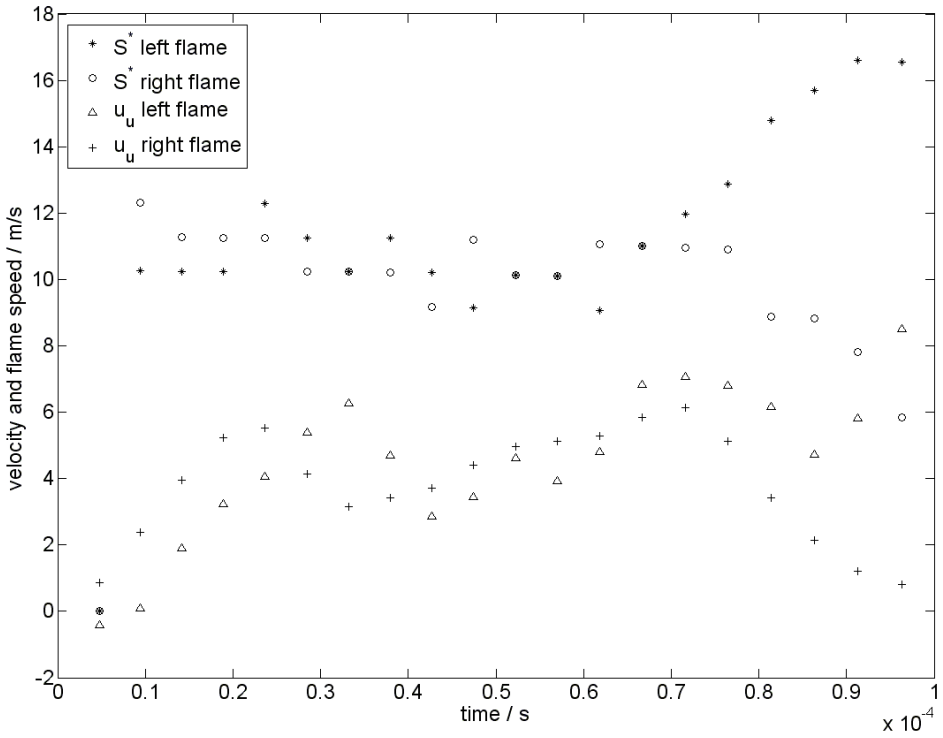

Figure 35. S_T^* for case 2 displayed as stars and circles and u_u at the flame front position displayed as triangles and plus signs for the left and right flame front respectively.

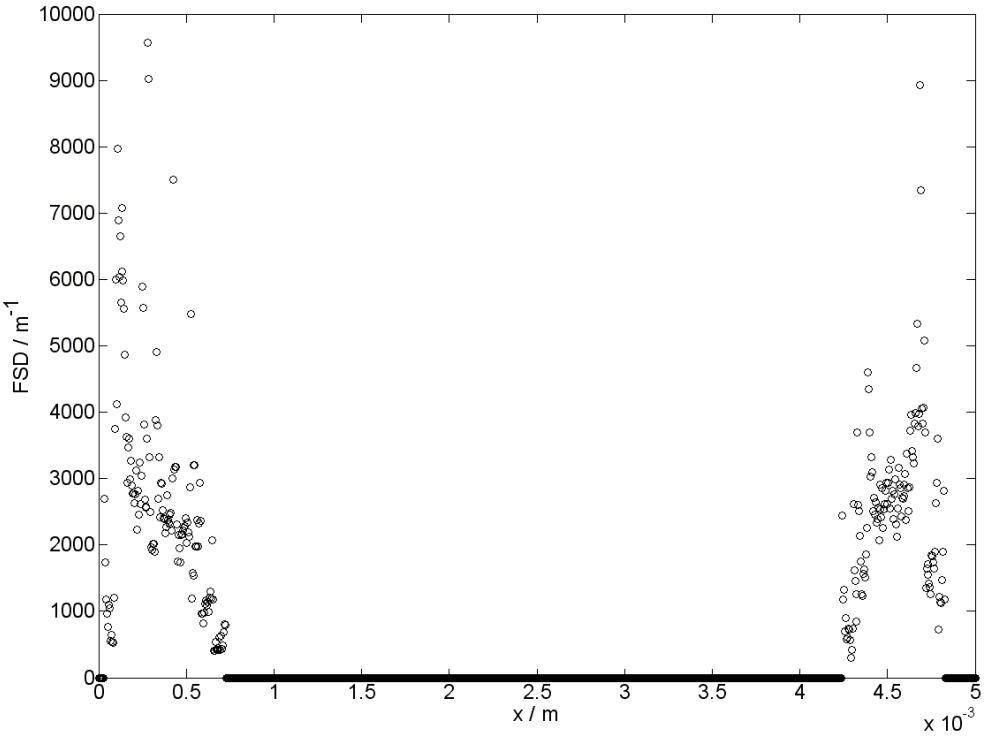

Figure 36. FSD for case 2 over the domain width at time $96.307\ \mu s$.

viscosity increase. It was then quite rapidly stabilized at a somewhat constant level. At later times, the high peak of vorticity left at the position of the flame front, which in early time was quickly lowered to the stabilized value, became broader. This is probably due to wrinkling effects, that the vorticity in the burned region is calculated as an average through division by the number of contributing cells.

4.1.4. Case 3 in 2D

For the third case, the Reynolds number and the integral length scale was increased and the turbulent scales were spread over a wider range. A time sequence of the propagation of the HO_2 species layer along with vorticity is shown in figure 38. An additional phenomenon visualized in this case is the propagation of an eddy pair through the flame front. This is clearly seen in the center of the flame front on the left hand side where the eddy pair starts to create an erosion in frame 2 and continues with the roll up in frame 3. Zoomed visualizations of the roll up at times $22.6391\,\mu s$ and $44.9502\,\mu s$ are shown in figure 39. When the eddy pair passes through the flame front, it leaves an unburned pocket of fuel and air on the burned side of the flame. It is eventually also burned, but the consumption of the fuel air pocket is relatively slow and at time $44.9502\,\mu s$, remainings of the eddy pair cavity is still discernable.

S_T^* was estimated through the method described in section 4.1 and plotted as a function of time in figure 40 with the values of the left flame front displayed with stars and the values of the right flame front displayed with circles. In the same figure, the

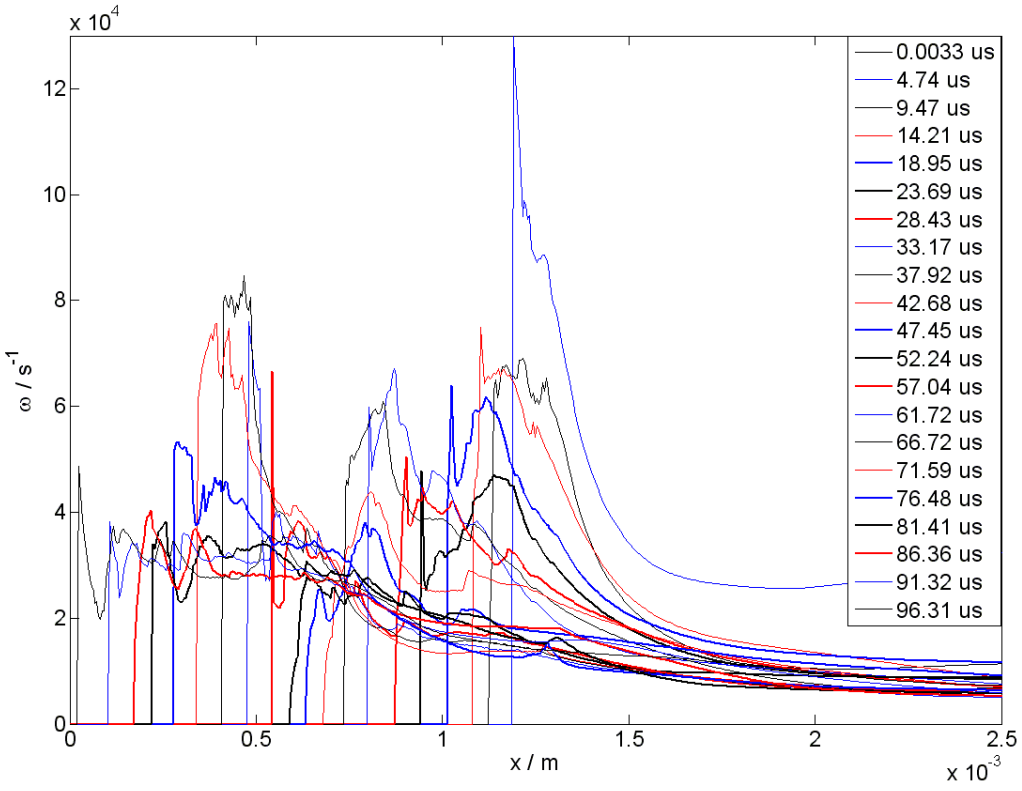

Figure 37. Vorticity on the burned side of the left flame front displayed for different times.

mean flow velocity at the flame front position is visualized with the values of the left flame front as triangles and the values of the right flame front with plus signs. The figure clearly shows the uncertainty of the turbulent flame speed when a very high turbulent intensity is contained in a small volume. The flame speed increases and drops very quickly and even becomes negative at one point. The interval of stability is considered to be located between times $5.99813\,\mu s$ and $17.3967\,\mu s$. The turbulent flame speed was therefore estimated as the mean of the stabilized values i.e.

$$S_{T,case3} = \frac{\sum_{j=4}^{10} S^*_{T,1,j} - u_{1,j} + \sum_{j=4}^{10} S^*_{T,2,j} - u_{2,j}}{2 \cdot 7} = 13.07 \frac{m}{s}. \tag{126}$$

The FSD was calculated for time $31.603\,\mu s$ and plotted in figure 41 to visualize the difference in wrinkling for the two flame fronts. As can be seen in frame 4 in figure 38, due to a small region with high propagation speed in the center of the domain height, the two flame fronts has almost merged. In figure 41 this is also shown as the nonzero part of the region

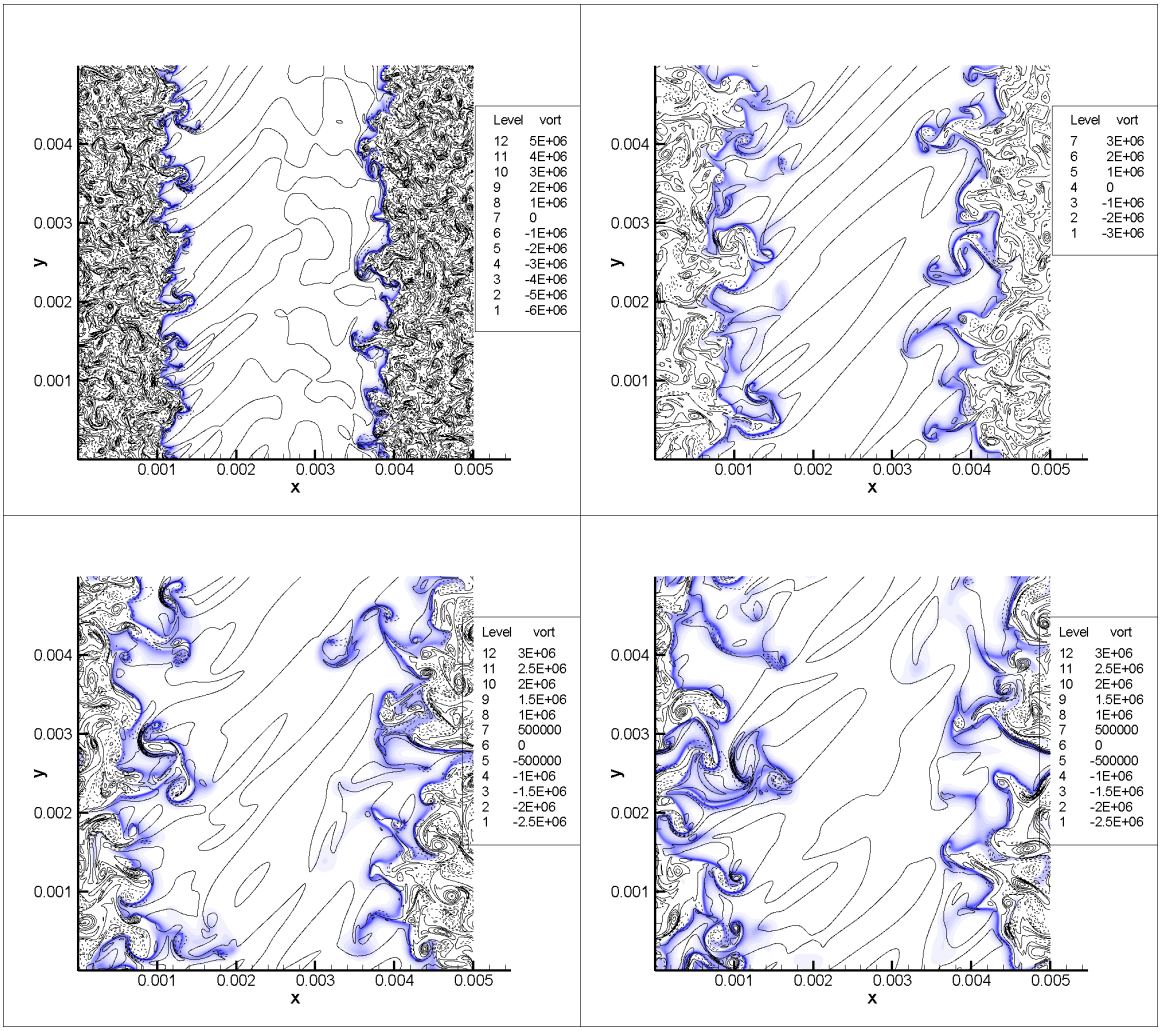

Figure 38. Time sequence of the HO_2 layer propagation along with vorticity for case 3. The frames corresponds to the elapsed times of $4.11844\,\mu s$, $13.4748\,\mu s$, $22.6391\,\mu s$ and $31.603\,\mu s$ respectively.

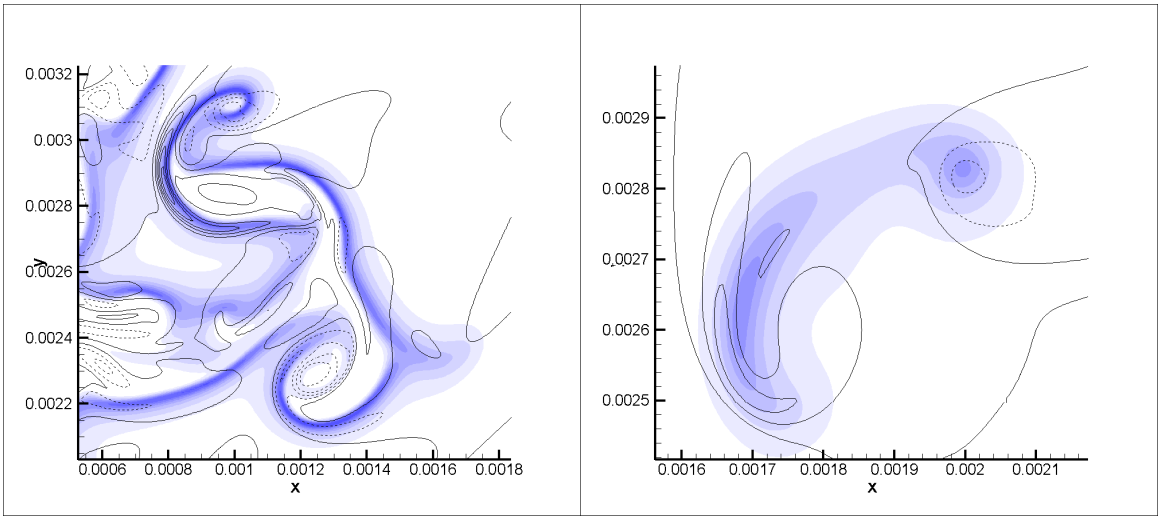

Figure 39. The roll up of the flame front by an eddy pair at time $22.6391\,\mu s$ and $44.9502\,\mu s$.

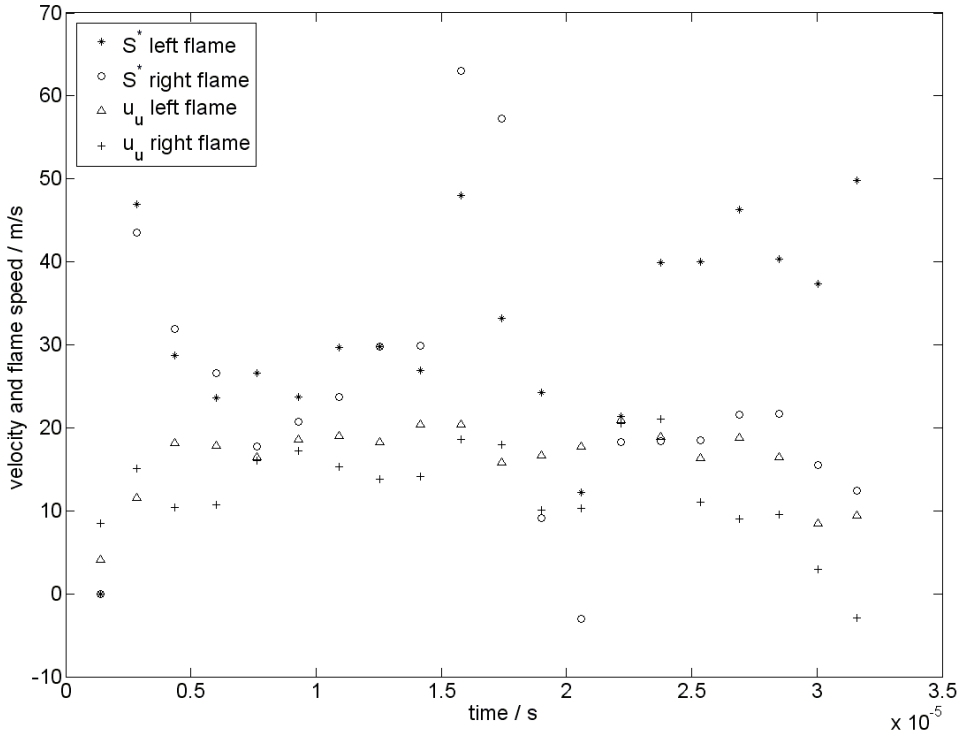

Figure 40. S_T^* for case 3 displayed as stars and circles and u_u at the flame front position displayed as triangles and plus signs for the left and right flame front respectively.

between the flame fronts. As previously shown, the left flame front was more wrinkled than the right one.

4.1.5. Case 4 in 2D

The fourth case is similar to the third one. The Reynolds number is practically the same, but the Karlovitz number is, like in the case 1/case 2 comparison, drastically lowered. A time sequence of the propagation of the HO_2 species layer along with vorticity is shown in figure 42 and as can be seen, the large scale distortion does not differ significantly from the one obtained in case 3. The pocket creation by eddy pairs is also similar to the case 3 study, but the vorticity near and inside the flame front is more obvious in case 3. Both the gradients and the actual maximum value of the vorticity is much higher in case 3.

S_T^* was estimated through the method described in section 4.1 and plotted as a function of time in figure 43 with the values of the left flame front displayed with stars and the values of the right flame front displayed with circles. In the same figure, u_u at the flame front position is visualized with the values of the left flame front as triangles and the values of the right flame front with plus signs. Between times $5.05062\,\mu s$ and $22.5043\,\mu s$, the difference between S_T^* and u_u was considered to be stabilized and the turbulent flame speed was therefore calculated as

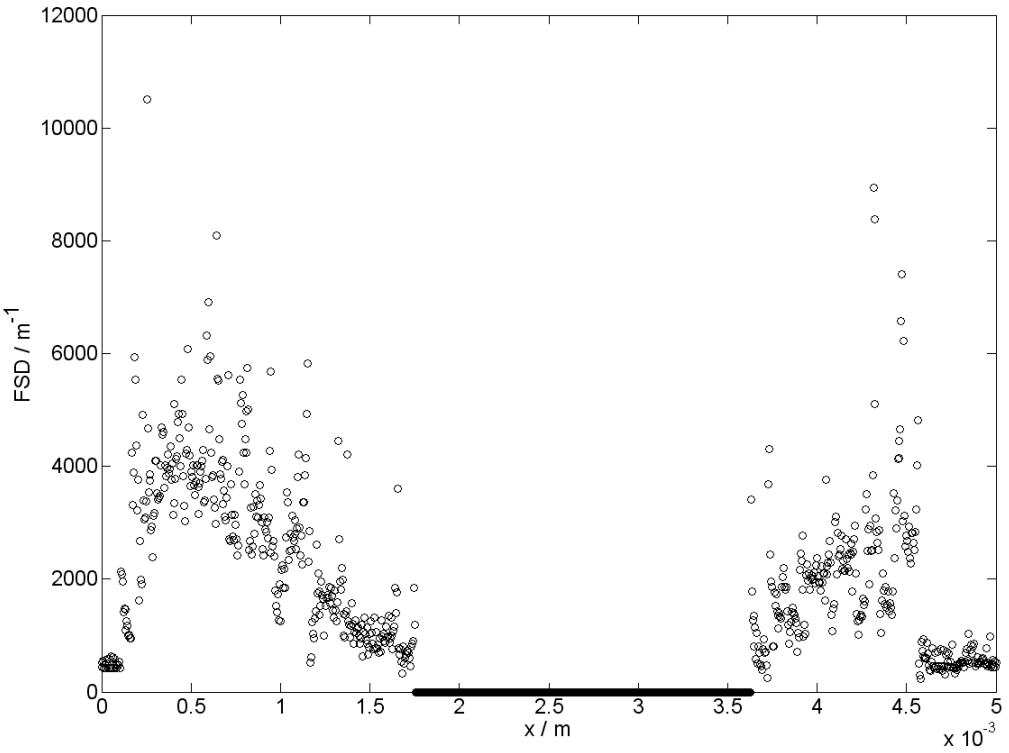

Figure 41. FSD for case 3 over the domain width at time $31.603\,\mu s$.

$$S_{T,case4} = \frac{\sum_{j=2}^{9} S^*_{T,1,j} - u_{1,j} + \sum_{j=2}^{9} S^*_{T,2,j} - u_{2,j}}{2 \cdot 8} = 10.26 \frac{m}{s} \tag{127}$$

The FSD was calculated and plotted for time $49.1243\,\mu s$ in figure 44 to visualize the difference in wrinkling for the two flame fronts. The FSD is very similar to the one plotted for case 3 and no further conclusions could be drawn.

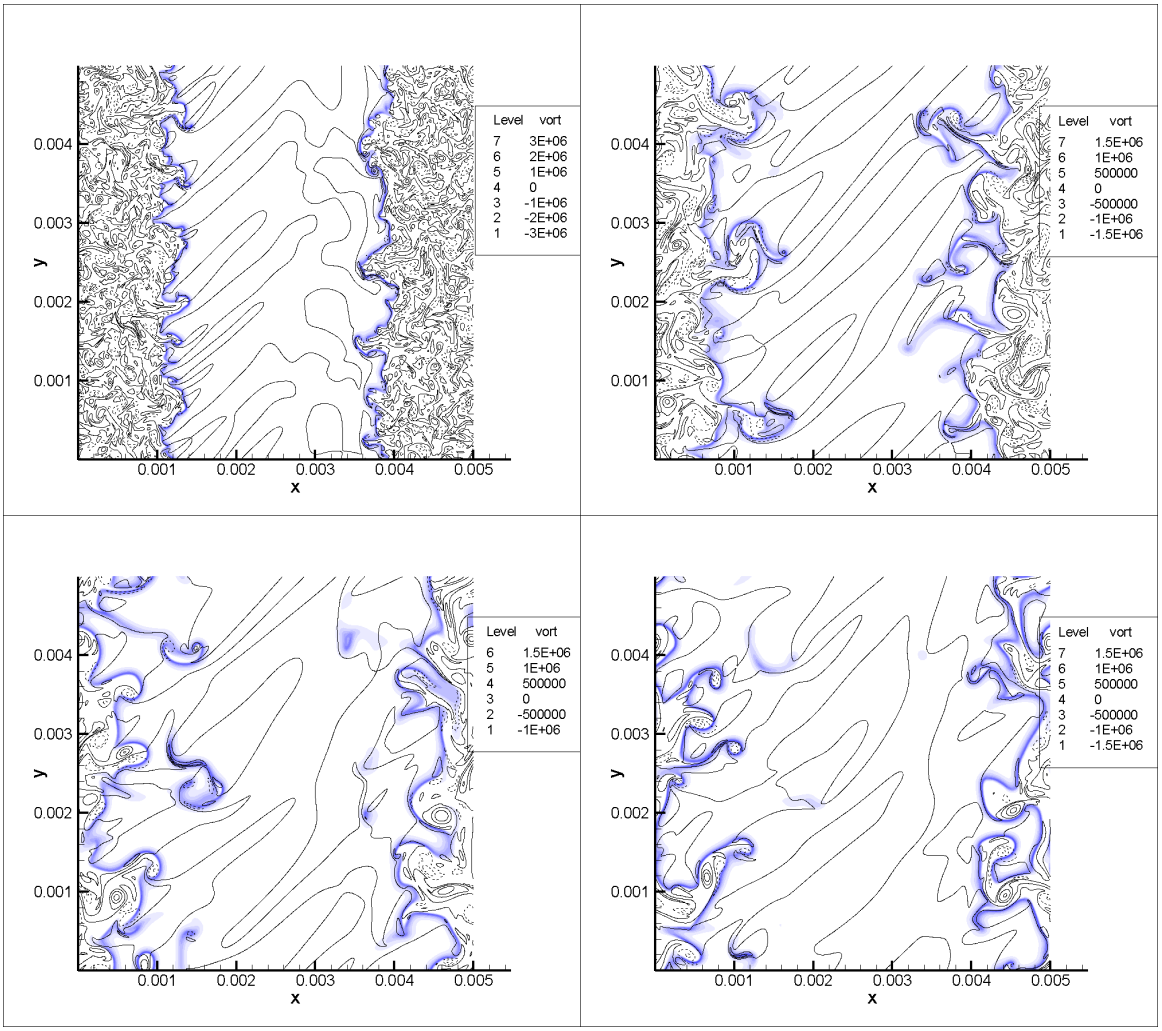

Figure 42. Time sequence of the HO_2 layer propagation along with vorticity for case 4. The frames corresponds to the elapsed times of $5.0506\,\mu s$, $22.5043\,\mu s$, $39.4755\,\mu s$ and $49.1243\,\mu s$ respectively.

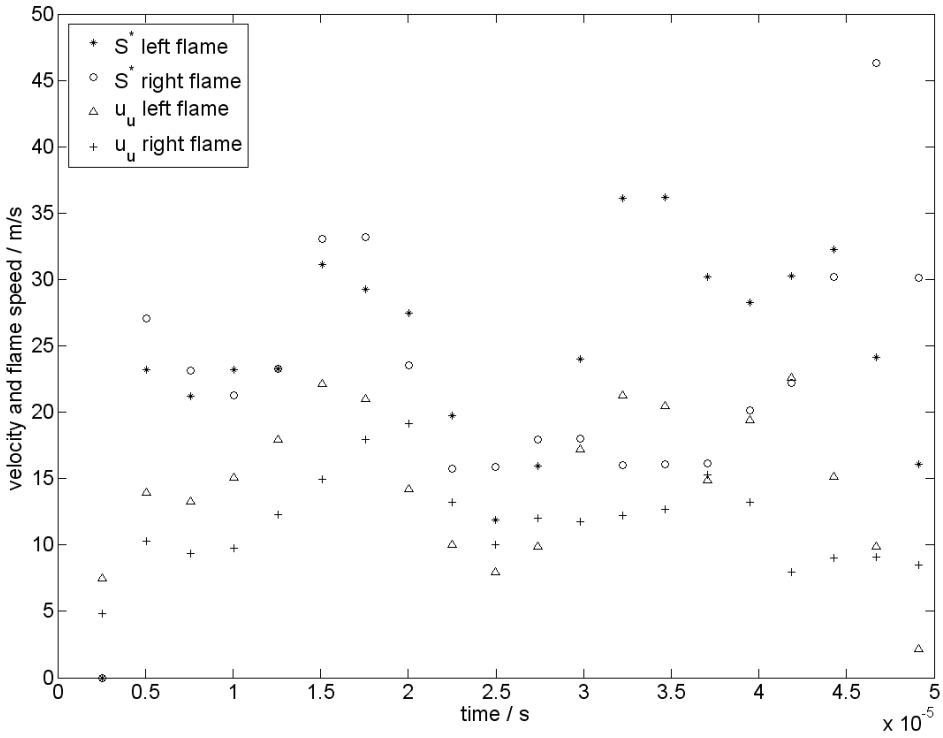

Figure 43. S_T^* for case 4 displayed as stars and circles and u_u at the flame front position displayed as triangles and plus signs for the left and right flame front respectively.

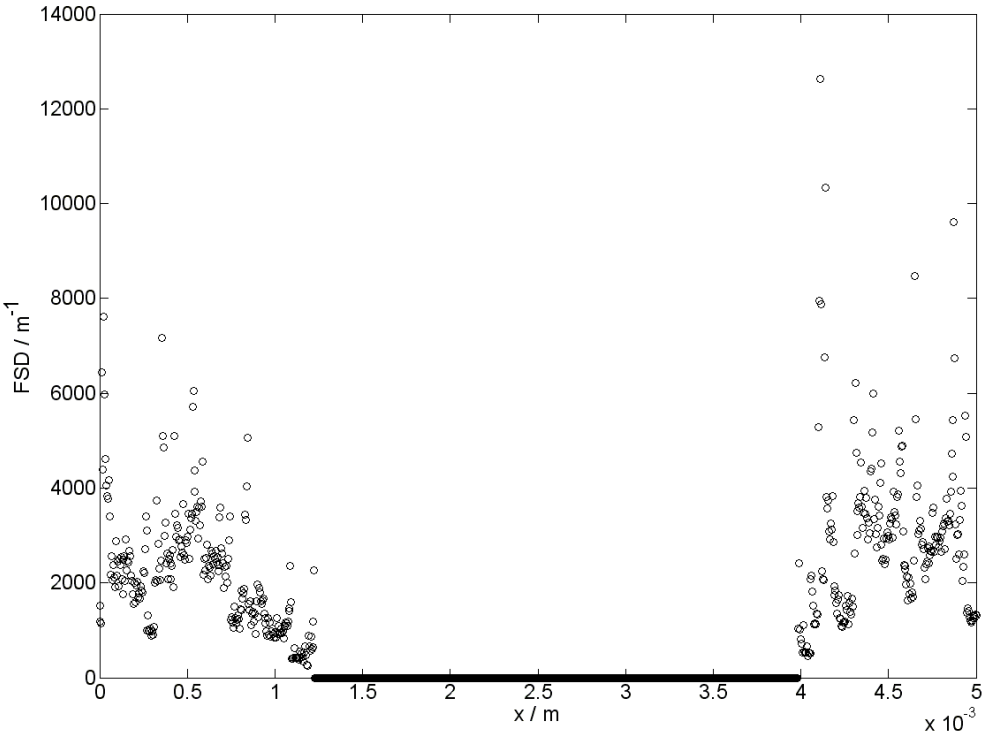

Figure 44. FSD for case 4 over the domain width at time $49.1243\,\mu s$.

4.1.6. Case 5 in 2D

In case 5, all the available parameters were increased, making the flame highly turbulent. A time sequence of the propagation of the HO_2 species layer along with vorticity is shown in figure 45. The overall flame turbulence interaction is similar to the one in case 3, but the large scale distortion is more intense.

Due to even higher rate of pocket formation and instabilities in the fuel distribution, the constant defining the flame front position was lowered to

$$\bar{c}(x,t) = 0.2\,. \tag{128}$$

S_T^* was estimated through the method described in section 4.1 and plotted as a function of time in figure 46 with the values of the left flame front displayed with stars and the values of the right flame front displayed with circles. In the same figure, u_u at the flame front position is visualized with the values of the left flame front as triangles and the values of the right flame front with plus signs. Between times $5.05062\,\mu s$ and $29.8239\,\mu s$, the difference between S_T^* and u_u was considered to be stabilized for the left flame front and the turbulent flame speed was therefore calculated as

$$S_{T,case5} = \frac{\sum_{j=7}^{13} S_{T,1,j}^* - u_{1,j}}{7} = 18.47\,\frac{m}{s} \tag{129}$$

The FSD was calculated and plotted for time $18.482\,\mu s$ in figure 47 to visualize the difference in wrinkling for the two flame fronts. The wrinkling is very severe, but the two different flame fronts are still possible to observe.

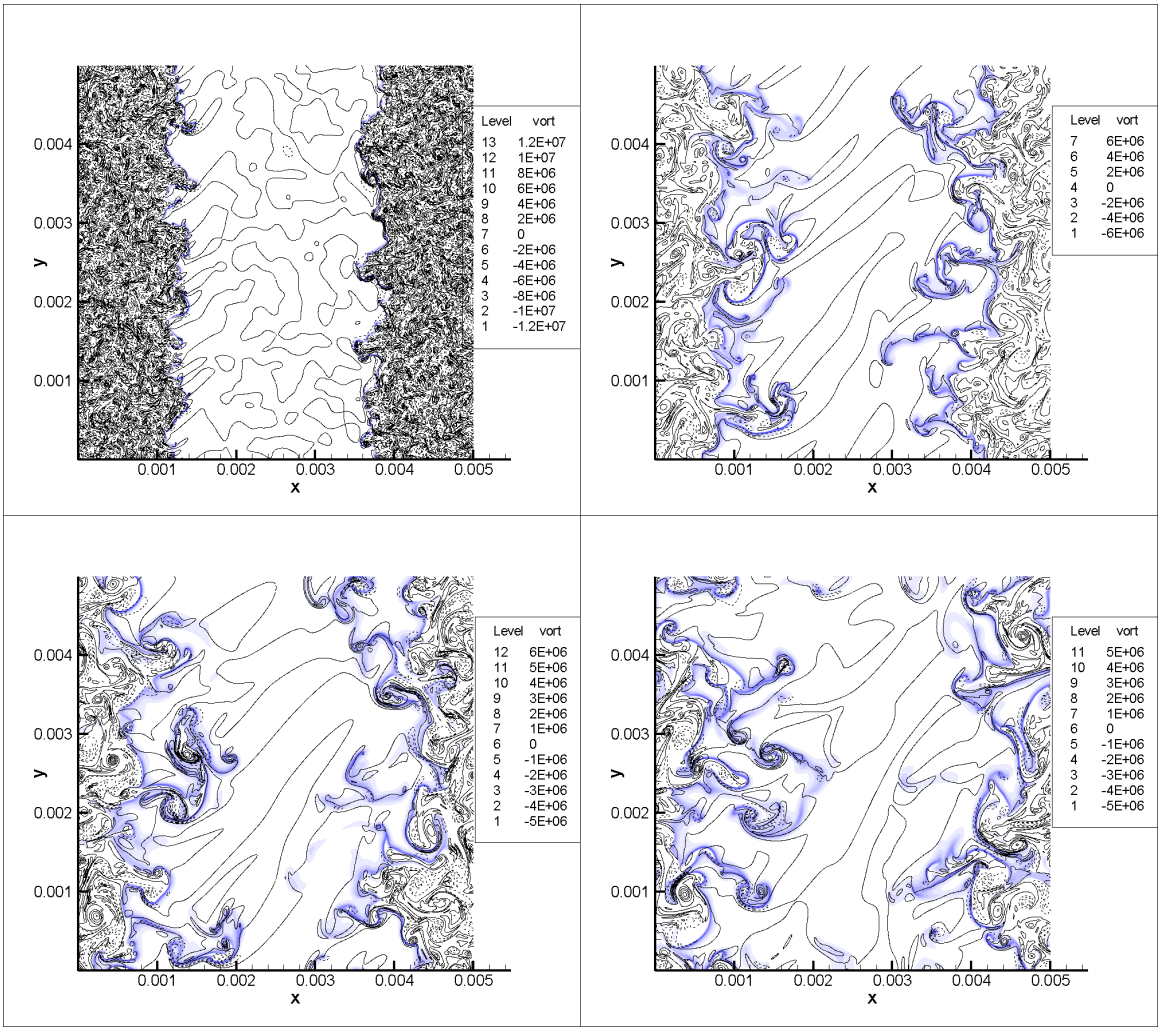

Figure 45. Time sequence of the HO_2 layer propagation along with vorticity for case 5. The frames corresponds to the elapsed times of 1.55906 μs, 8.08016 μs, 13.0647 μs and 18.482 μs respectively.

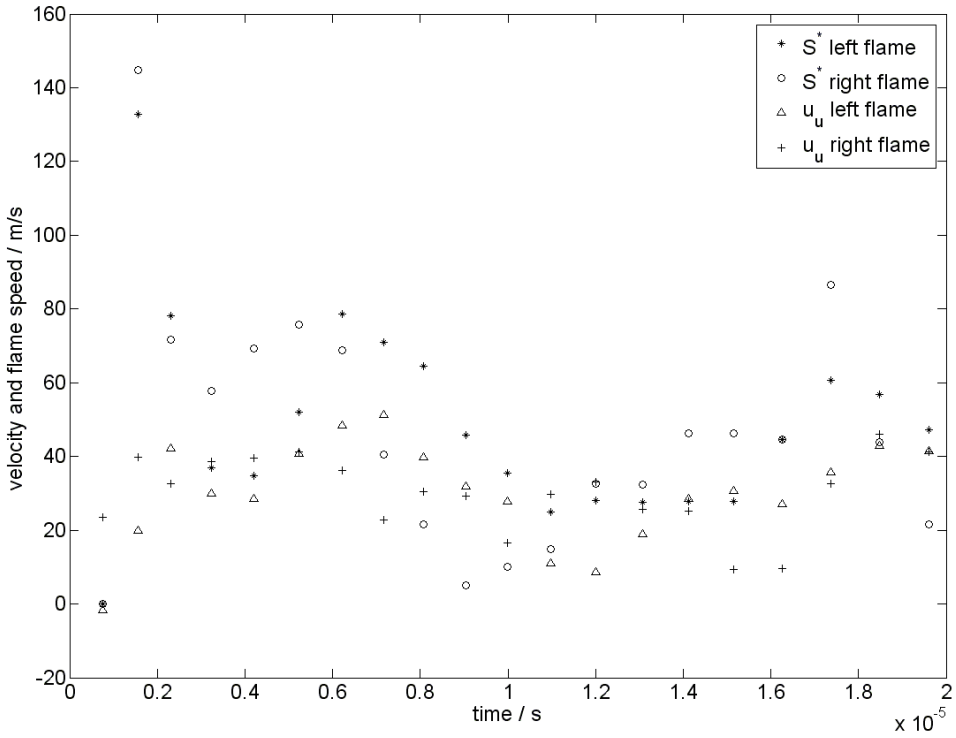

Figure 46. S_T^* for case 5 displayed as stars and circles and u_u at the flame front position displayed as triangles and plus signs for the left and right flame front respectively.

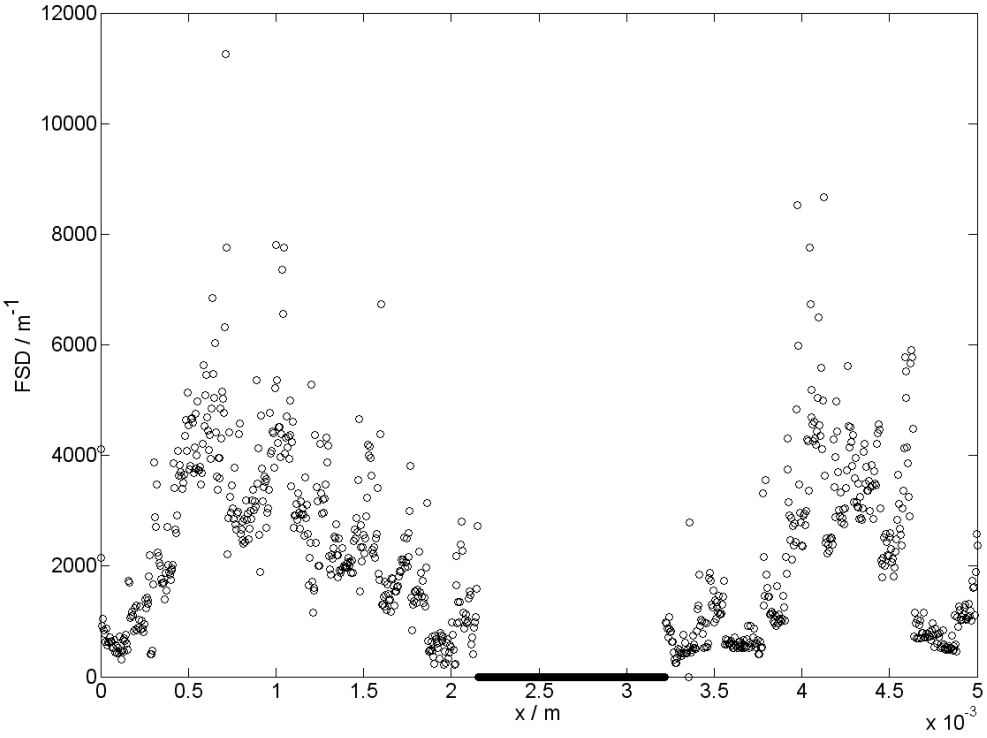

Figure 47. FSD for case 5 over the domain width at time $31.603\,\mu s$.

4.1.7. Case 6 in 2D

In case 6, the Reynolds number was raised close to the limit of sufficient resolution. A time sequence of the propagation of the HO_2 species layer along with vorticity is shown in figure 48. The hot band for flame initiation was almost shattered and it is doubtful whether a turbulent flame front could be considered to be achieved. To make this case physically interesting as a propagating planar flame, a larger physical domain is needed to make the flame stabilized.

S_T^* was estimated through the method described in section 4.1 and plotted as a function of time in figure 49 with the values of the left flame front displayed with stars and the values of the right flame front displayed with circles. In the same figure, u_u at the flame front position is visualized with the values of the left flame front as triangles and the values of the right flame front with plus signs. Equation (128) was used in case 6 as well due to the heavy pocket formation. The flame speed fluctuations were extreme in case 6 and the right flame front transportation speed varied over a span of $300\ m/s$, making a stable interval difficult to find.

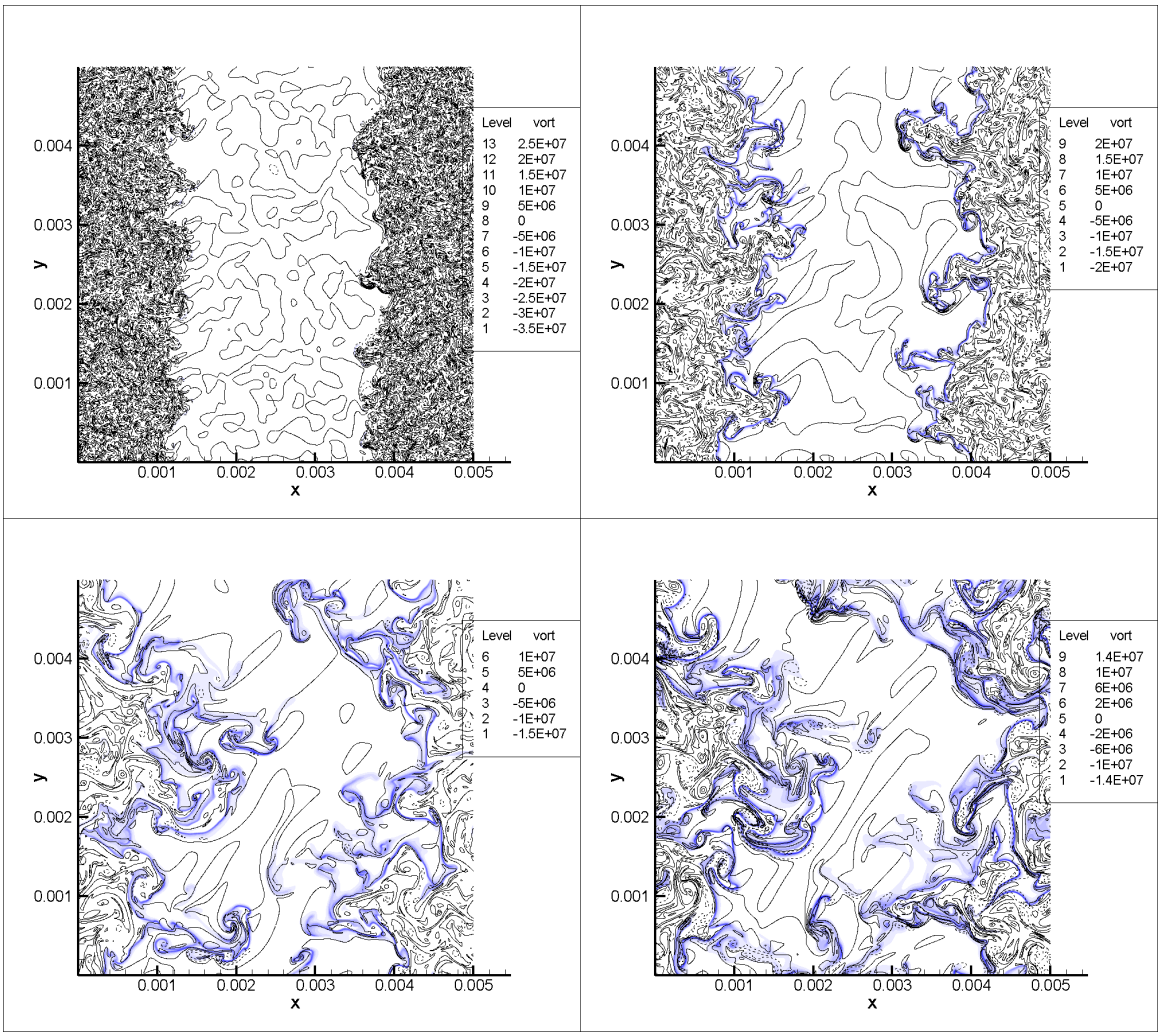

Figure 48. Time sequence of the HO_2 layer propagation along with vorticity for case 6. The frames corresponds to the elapsed times of $0.776923\,\mu s$, $2.64122\,\mu s$, $6.72875\,\mu s$ and $8.93823\,\mu s$ respectively.

It was nevertheless considered that the difference between S_T^* and u_u between times $1.66977\,\mu s$ and $4.13671\,\mu s$ for the left flame front reached some kind of steady state and the turbulent flame speed was calculated as

$$S_{T,case6} = \frac{\sum_{j=4}^{9} S_{T,1,j}^* - u_{1,j} + \sum_{j=4}^{9} S_{T,2,j}^* - u_{2,j}}{2 \cdot 6} = 35.76 \frac{m}{s} \tag{130}$$

The FSD was calculated and plotted for time $8.93823\,\mu s$ in figure 50 to visualize the difference in wrinkling for the two flame fronts. At this point of the flame propagation, the flame front was heavily wrinkled and distributed over the entire domain width.

4.2. 3D simulations

To obtain more physical results, turbulence should be simulated in three dimensions and, as written in section 3.2, the cases 3 and 4 were also simulated in 3D using $128 \times 128 \times 128$ grid resolution.

4.2.1. Case 3 in 3D

A visualization of a 3D simulation of case 3 through the HO_2 layer along with the 2D temperature distribution in the x-y plane and the vorticity in the x-z plane at time $42.384\,\mu s$ is

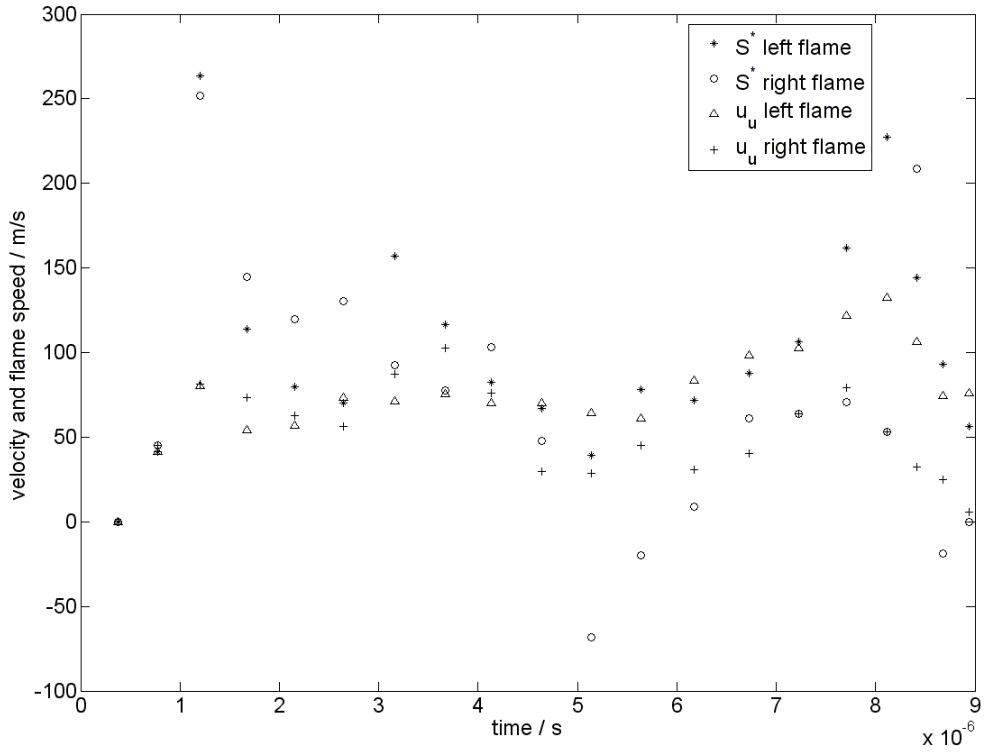

Figure 49. S_T^* for case 6 displayed as stars and circles and u_u at the flame front position displayed as triangles and plus signs for the left and right flame front respectively.

shown in figure 51. A 2D time sequence of the propagation of the HO_2 species layer along with vorticity is shown in figure 52. Due to a plotting issue, the vorticity lines follow the edges of the domain parts when shown in 2D.

The shape of the HO_2 layer is very different from the one obtained in section 4.1.4. Both small scale and large scale distortion is less severe and the HO_2 layer appears more smudged. The unclear shape of the HO_2 layer is probably due to the low resolution. The vorticity lines also show the 3D effect. In the burned region it is most clear and the vorticity lines overlap each other in a way not visible in the 2D simulated case 3 in figure 38.

S_T^* was estimated through the method described in section 4.1, but to obtain a 1D distribution of the fuel, an averaging over the z-axis through integration was also performed. S_T^* was then plotted as a function of time in figure 53 with the values of the left flame front displayed with stars and the values of the right flame front displayed with circles. In the same figure, u_u at the flame front position was visualized with the values of the left flame front as triangles and the values of the right flame front with plus signs. The figure clearly shows the lack of resolution in the 3D simulation. The flame front position is determined by a certain grid number, which has lower accuracy at a coarse 3D grid compared to 2D. This means that initially the flame front only moves one cell each time step and while the time steps grows, the flame transportation speed shrinks. At approximate time $2-2.5\,\mu s$, the flame fronts start to move two cells each time step and therefore suddenly increases. Due to equal time steps

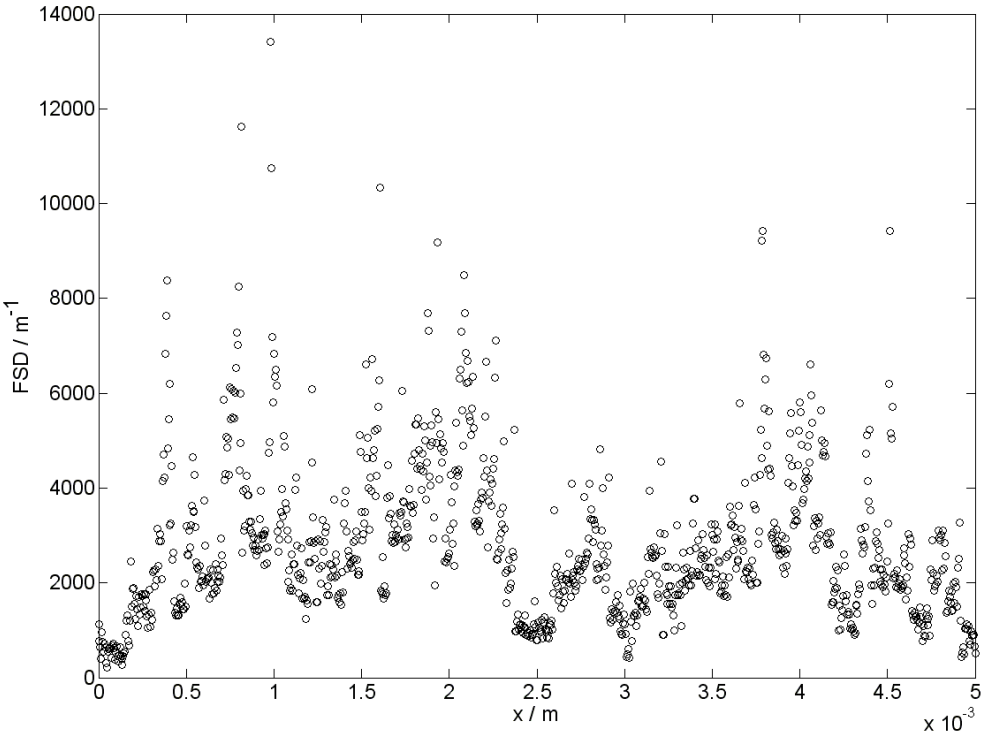

Figure 50. FSD for case 6 over the domain width at time $8.93823\,\mu s$.

and flame transportation for most times, this also explains why the flame transportation speed is identical for the two fronts at many times. The flame speed was calculated as a mean from time $6.34237\,\mu s$ i.e.

$$S_{T,case3D} = \frac{\sum_{j=5}^{20} S^*_{T,1,j} - u_{1,j} + \sum_{j=5}^{20} S^*_{T,2,j} - u_{2,j}}{2 \cdot 16} = 20.91 \frac{m}{s}. \qquad (131)$$

The turbulent flame speed is higher in 3D than in 2D. Which one of the two values that is better is not easy to guess without experimental comparison. 2D has the advantage of more exact determination of the flame front position, but a very fluctuating flame speed over time. 3D has the advantage of averaging over a larger amount of cells, but the poor determination of the flame front position gives a high uncertainty for each value.

In the 3D cases, the FSD was not calculated through equations (108) and (109). The flame being a surface instead of a line and the control cell being a volume instead of an area, the

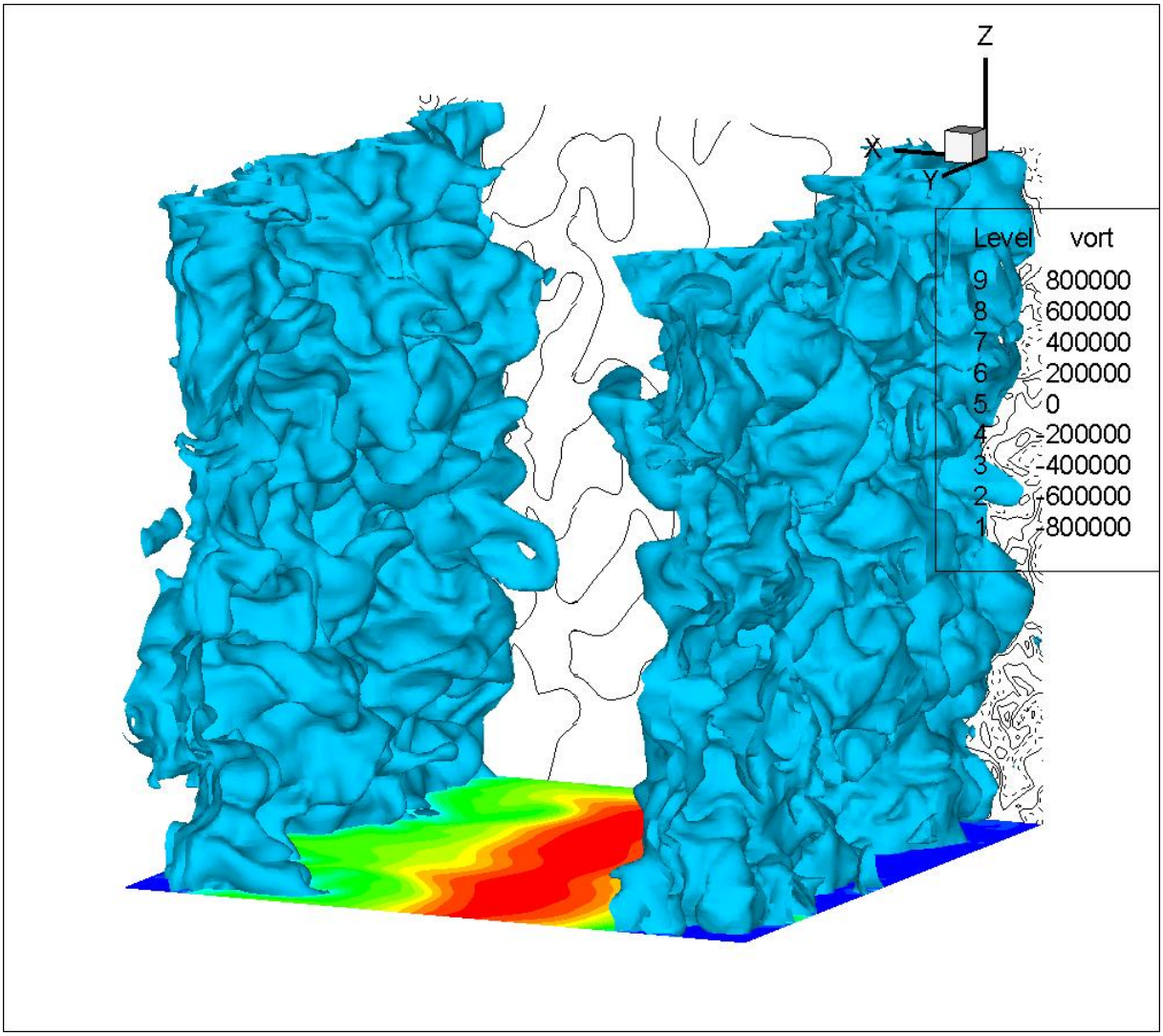

Figure 51. HO_2 layer along with the temperature distribution at the x-y plane and the vorticity at the x-z plane at time $42.384\,\mu s$.

FSD variable Σ in cell i, j, k was calculated by

$$\Sigma(i,j,k) = \frac{A_{i,j,k}}{\Delta x \cdot \Delta y \cdot \Delta z}, \tag{132}$$

where $A_{i,j,k}$ is the flame front area in cell i, j, k and Δz the cell size in the z direction. The FSB average over the entire flame front is then calculated by

$$\overline{\Sigma}(i) = \frac{1}{N_j N_k} \sum_{j=1}^{N_j} \sum_{k=1}^{N_k} \Sigma(i,j,k). \tag{133}$$

The FSD was calculated and plotted for time $32.7627\,\mu s$ in figure 54 to visualize the difference in wrinkling for the two flame fronts. A comparison between the 3D FSD, figure 54, and the 2D FSD, figure 41, who are taken at approximately the same time, shows similarities. If the height of the peaks in figure 41 is approximated to somewhere in the

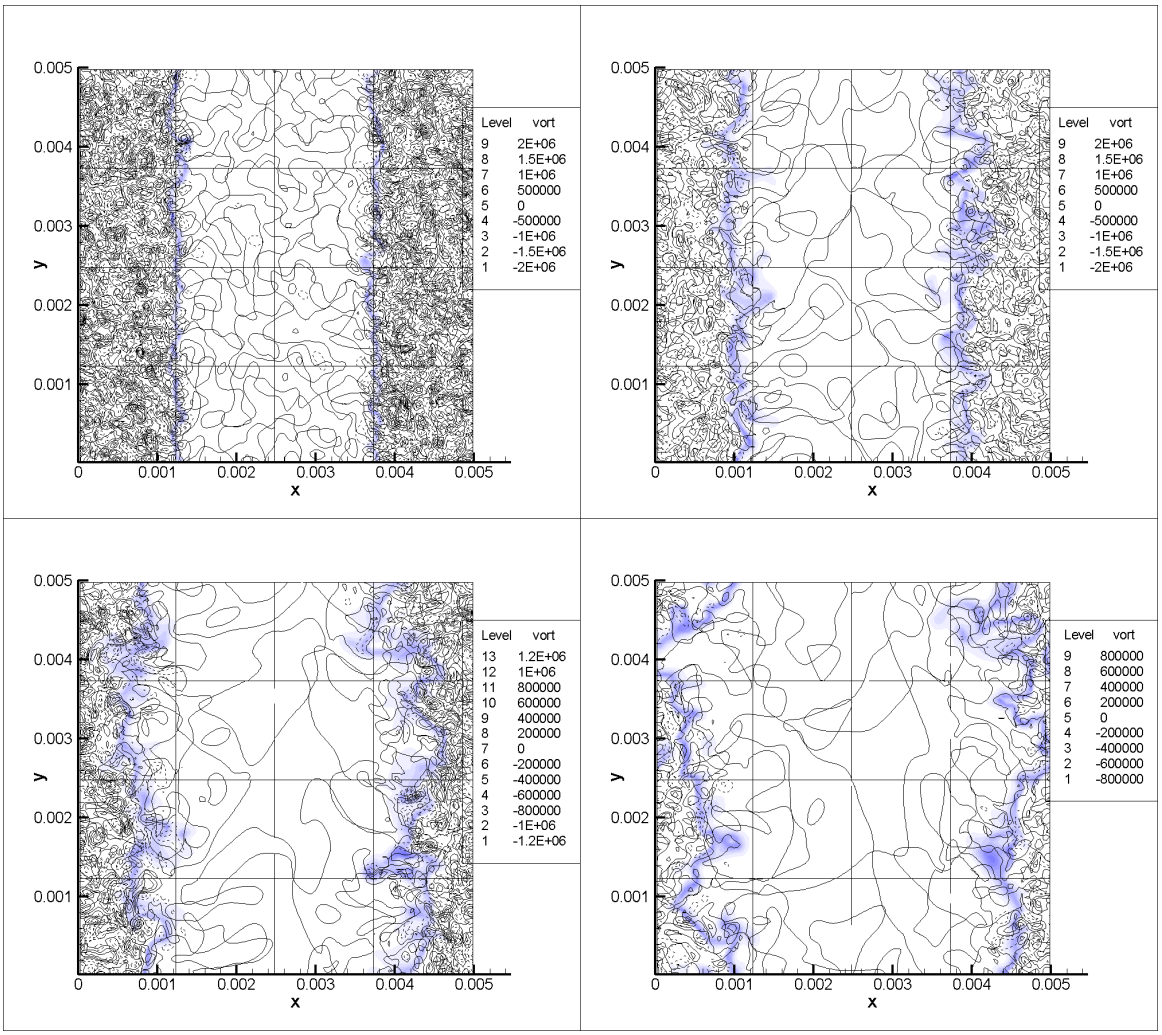

Figure 52. Time sequence of the flame propagation for case 3, simulated in 3D. The frames corresponds to the elapsed times of $1.80827\,\mu s$, $9.5067\,\mu s$, $22.8019\,\mu s$ and $42.384\,\mu s$ respectively.

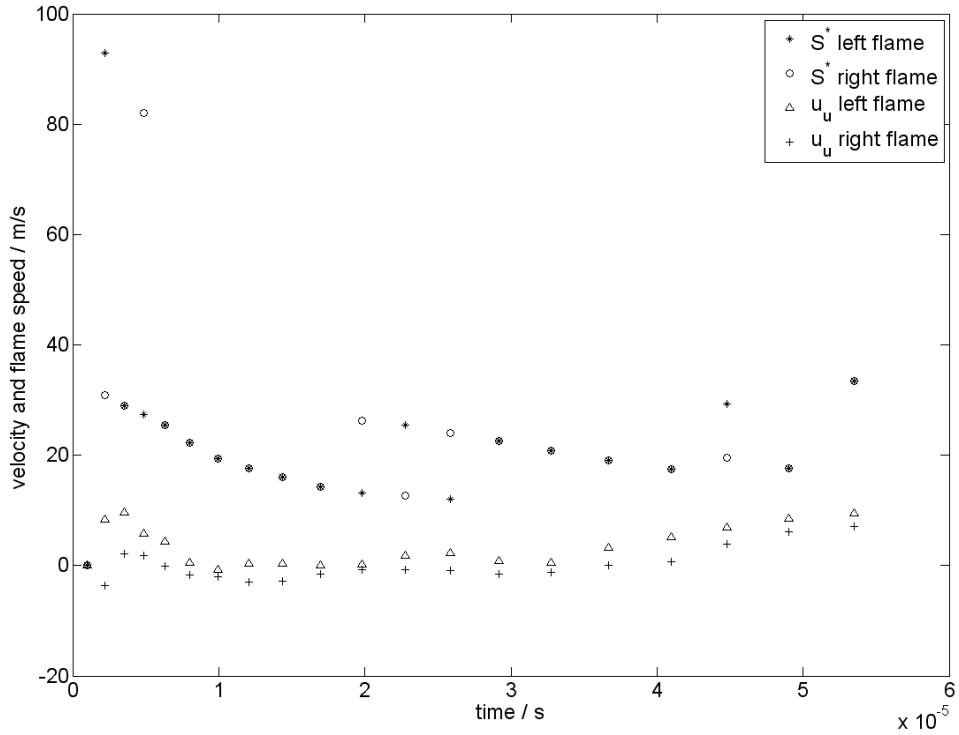

Figure 53. S_T^* for case 3 in 3D displayed as stars and circles and u_u at the flame front position displayed as triangles and plus signs for the left and right flame front respectively.

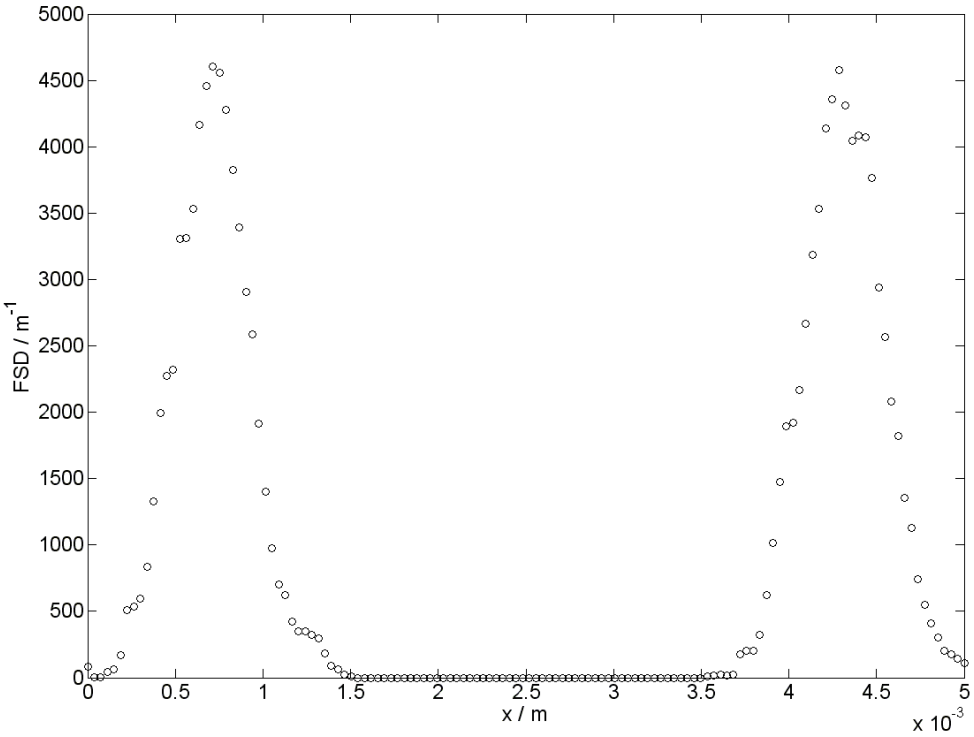

Figure 54. FSD for case 3 in 3D over the domain width at time $32..7627\,\mu s$.

interval $4000-5000\frac{1}{m}$, both the width, height and position of the peaks are almost identical for 2D and 3D. What differs is the shape. In the 3D simulation, a nearly perfect Gaussian distribution was obtained, while the one in 2D was much more chaotic and a Gaussian shape was difficult to observe. The reason for the Gaussian shape in 3D is probably due to the averaging over 16 times more cells in comparison to 2D. An additional similarity is that the left flame front has some kind of a tail in both 2D and 3D due to pocket formation and remainings of flame front on the burned side of the flame.

4.2.2. Case 4 in 3D

A visualization of a 3D simulation of case 3 through the HO_2 layer along with the 2D temperature distribution in the x-y plane and the vorticity in the x-z plane at time $26.812\,\mu s$ is shown in figure 55. A 2D time sequence of the propagation of the HO_2 species layer along with vorticity is shown in figure 56. Due to a plotting issue, the vorticity lines follow the

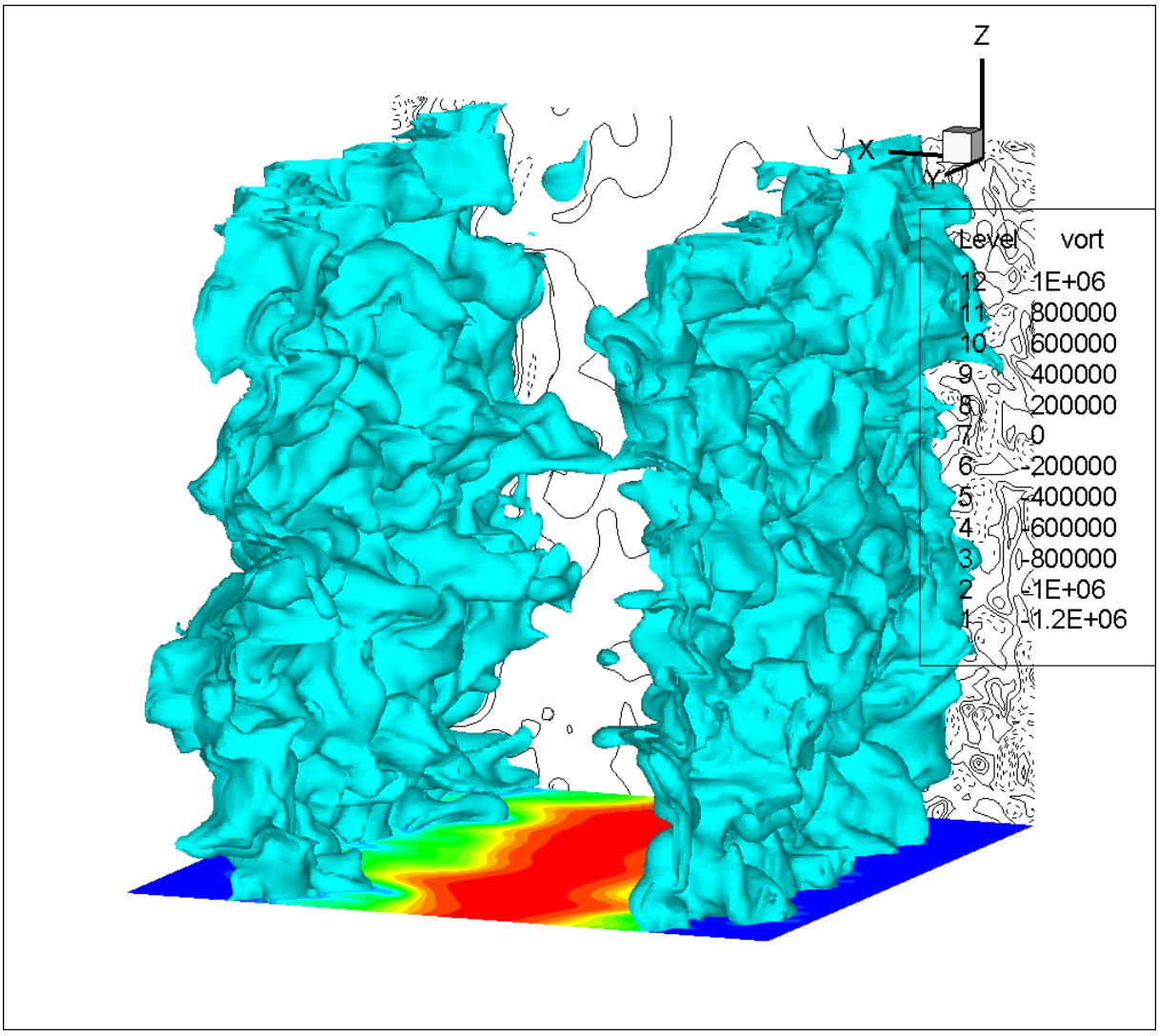

Figure 55. HO_2 layer along with the temperature distribution at the x-y plane and the vorticity at the x-z plane at time $26.812\,\mu s$.

edges of the domain parts when shown in 2D.

S_T^* was estimated through the method described in section 4.1 along with averaging of the fuel distribution over the z-axis through integration. S_T^* was then plotted as a function of time in figure 57 with the values of the left flame front displayed with stars and the values of the right flame front displayed with circles. In the same figure, u_u at the flame front position was visualized with the values of the left flame front as triangles and the values of the right flame front with plus signs. The interval of stability is considered to be located between times $7.97269\,\mu s$ and $41.2267\,\mu s$. The turbulent flame speed was estimated as the mean of the stabilized values i.e.

$$S_{T,case43D} = \frac{\sum_{j=5}^{17} S_{T,1,j}^* - u_{1,j} + \sum_{j=5}^{17} S_{T,2,j}^* - u_{2,j}}{2 \cdot 13} = 23.39 \frac{m}{s}. \tag{134}$$

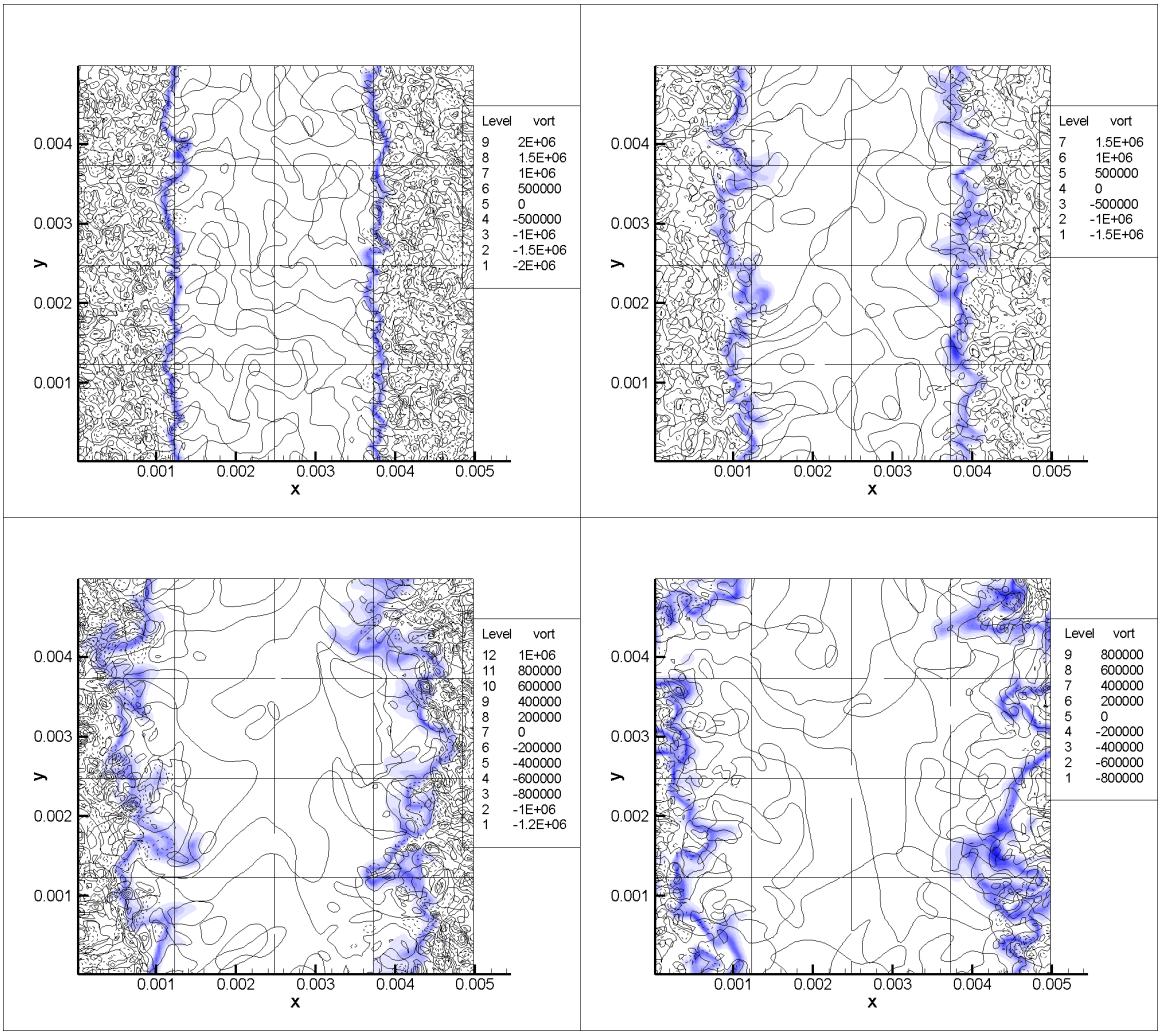

Figure 56. Time sequence of the flame propagation for case 4, simulated in 3D. The frames corresponds to the elapsed times of $3.07437\,\mu s$, $10.4458\,\mu s$, $26.812\,\mu s$ and $48.9424\,\mu s$ respectively.

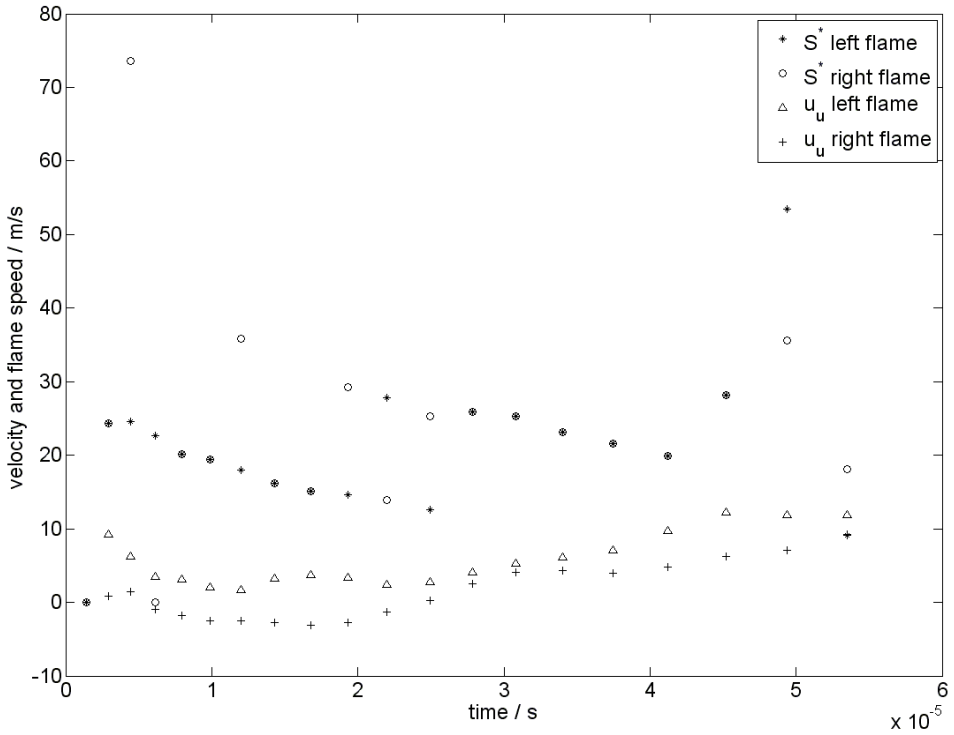

Figure 57. S_T^* for case 4 in 3D displayed as stars and circles and u_u at the flame front position displayed as triangles and plus signs for the left and right flame front respectively.

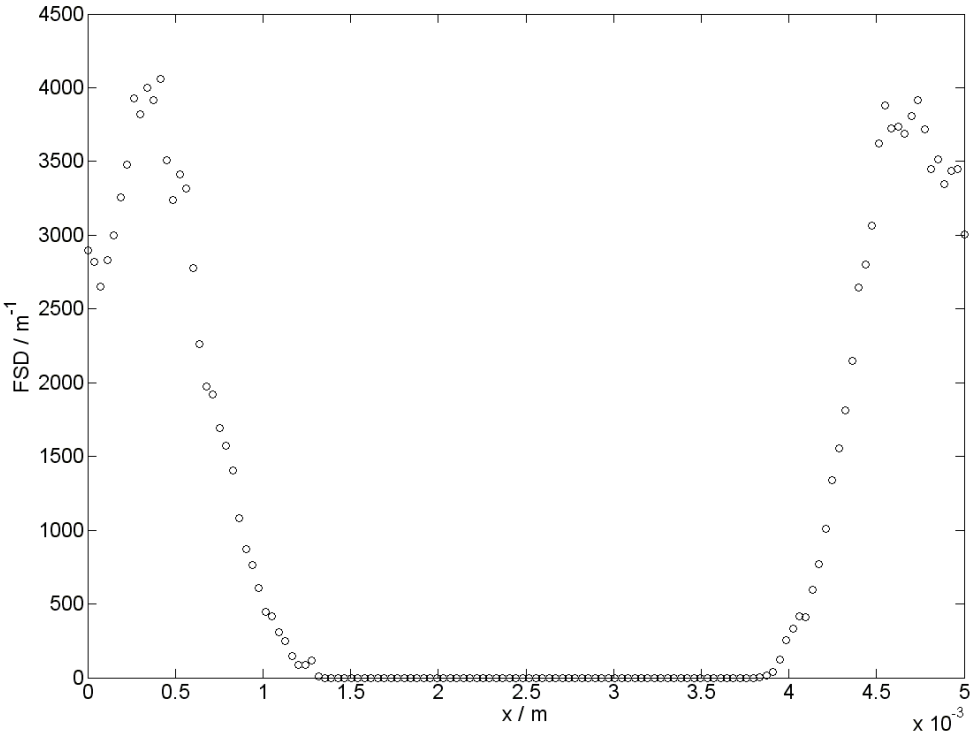

Figure 58. FSD for case 4 in 3D over the domain width at time $49.0271\mu s$.

As for case 3, the turbulent flame speed for case 4 in 3D is quite high compared to the 2D measured one.

The FSD was calculated and plotted for time $49.0271\mu s$ in figure 58 to visualize the difference in wrinkling for the two flame fronts. Like in the 3D case 3, if the 3D FSD, figure 58, is compared with the 2D FSD for case 4, figure 44, both width, approximate height and position are very similar for 2D and 3D.

5. Conclusions and future work

5.1. Initial field

The initial turbulence field can be created through different methods. When the methods described in sections 3.1.2 and 3.1.3 were tested, differences were not discerned with the naked eye and which one to prefer was not obvious. Since the FFT method is much faster, the results indicate that this is the method to prefer. It was therefore the method used in all computations.

To assure a physically reliable energy spectrum, the high Reynolds number energy spectrum function with Reynolds number dependant modeling parameters should be used. With the low Reynolds number energy spectrum function, a too small amount of energy is distributed to the smallest scales and more importantly; it is completely independent of Reynolds number.

5.2. Turbulent combustion

Through simulations of turbulent combustion at various turbulent intensity and integral length scale, a few fundamental phenomenons were observed.

HO_2 and H_2O_2 are good indicators of the position of the preheat zone, both for laminar and turbulent flames. This also proves that the preheat zone is not free from reactions. The rates of high temperature reactions are low, but the preheat zone is clearly not free from low temperature reactions.

The eddy pair rollup and the species distribution within the reaction zone were clearly visualized. The rollup is a large scale phenomenon and was very clear for cases 3-6 where the integral length scale became a quite large part of the domain length.

The 2D flame speed measurements did not benefit from the clear visualization of the flame front rollup. The measurements became difficult to perform through the kind of statistically averaging method used in this thesis. The turbulent flame speed was found to be very dependent on the turbulent intensity as well as the integral length scale. On what scale the largest flame wrinkling occurs is important, since the flame speed increase due to wrinkling is mainly a large scale phenomenon.

DNS results are very dependent on the resolution. Comparisons between 2D and 3D simulations, where the resolution differ by a factor 8, show differences in the fundamental physical phenomenon visualized. Simulations performed in 2D lacks the important conditions

of turbulence being three dimensional and when averaging through the method used in this thesis, 3D gives 16 times better statistics.

High resolution is, as discussed previously, of major importance in studies of fundamental physics through DNS. The increased resolution in 2D therefore makes it, with current computational power and accessible memory, highly interesting.

5.3. Future work

After performing high resolution 2D simulations and low resolution 3D simulations, the vision is obviously to perform 3D with high resolution. The computational requirements for this is however extremely high and will probably remain a vision for several years. The future work more close by, before the vision is fulfilled, might be introducing some turbulence feeding for the largest scale during the solving process to keep the initial turbulence from dissipating before combustion. An interesting method to be able to perform longer simulations could be the introduction of inlet and outlet boundary conditions in the x-direction along with the feeding of unburned turbulent gas mixture at the inlet. After the initiation of the two flame fronts, one of them is designated to blow off and the other one is stabilized in the center of the domain. With varying inlet feeding velocity, the turbulent flame speed could in this way be better estimated by conditioning a stable flame front. Through this method for better estimating the turbulent flame speed, simulations for fixed values of the turbulent intensity and varying integral length scales, or vice versa, could be perform, expanding, and determine with higher precision, the tables presented in this work.

The definition of the flame front through fuel distribution requires a larger physical domain to obtain a statistically well positioned flame surface. This will for sure improve the measurements of the flame speed.

To be sure that flame induced vorticity is observed, the decay due to viscosity raise has to be subtracted from the vorticity field. If this is not done, separation of the flame induced and the initial field remaining vorticity can not be done.

To detect flame holes, the reaction rate in the oxidation layer has to be studied. In places where the rate of formation of water is low, a flame hole could be present.

6. Acknowledgements

The computations in this work were performed on the computation center, LUNARC, on Lund's university.

I would like to thank my supervisor Prof. Xue-Song Bai for the opportunity of performing this master thesis study and for introducing me to the field of turbulent combustion. Each discussion we have had has improved my understanding of the subject.

I would also like to thank Dr. Rixin Yu for all help with numerous questions of coding and CFD.

I thank Rickard Solsjö, Ali Alsam and Roy van der Wijst for keeping my spirit up and for all nice topics of discussion over coffee.

7. References

[1] Turns SR. An introduction to combustion. 2006, second edition: McGraw-Hill higher education.

[2] Poinsot T, Veynante D, Candel S. Diagrams of premixed turbulent combustion based on direct simulation. Twenty-Third Symposium on Combustion/The Combustion Institute 1990:613-619.

[3] Renard PH, Thévenin D, Rolon JC, Candel S. Dynamics of flame/vortex interactions. Prog. Energ. Combust. Sci. 2000;26:225-285.

[4] Kadowaki S, Hasegawa T. Numerical simulation of dynamics of premixed flames: flame instability and vortex-flame interaction. Prog. Energ. Combust. Sci. 2005;31:193-241.

[5] Najm, HN, Wyckoff P. Premixed flame response to unsteady strain rate and curvature. Combust. and flame 1997;110:92-112.

[6] Li ZS, Li B, Sun ZW, Bai XS, Aldén M. Turbulence and combustion interaction: high resolution local flame front structure visualization using simultaneous single-shot PLIF imaging of CH, OH, and CH2O in a piloted premixed jet flame. Combust. and flame 2010;157:1087-1096.

[7] Driscoll JF. Turbulent premixed combustion: Flamelet structure and its effect on turbulent burning velocities. Prog. Energ. Combust. Sci. 2008;31:91-134.

[8] Sankaran V, Menon, S. Structure of premixed flames in the thin-reaction-zones regime. Proceedings of the Combustion institute 2000;28:203-209.

[9] Sankaran V, Menon, S. Subgrid combustion modeling of 3-D premixed flames in the thin-reaction-zone regime. Proceedings of the Combustion institute 2005;30:575-582.

[10] Bell JB, Day MS, Grcar JF, Lijewski MJ, Driscoll JF, Filatyev SA. Numerical simulation of a laboratory-scale turbulent slot flame. Prog. Energ. Combust. Sci. 2007;31:1299-1307.

[11] Bell JB, Day MS, Shepherd IG, Johnson MR, Cheng RK, Grcar JF, VE Beckner, MJ Lijewski. Numerical simulation of a laboratory-scale turbulent V-flame. PNAS 2005;102:10006-10011.

[12] Sankaran R, Hawkes ER, Chen JH, Lu T, Law CH. Structure of a spatially developing turbulent lean methane-air Bunsen flame. Proceedings of the Combustion Institute 2007;31:1291-1298.

[13] Chen YC, Bilger RW. Simultaneous 2-D imaging measurements of reaction progress variable and OH radical concentration in turbulent premixed flames: instantaneous flame-front structure. Combust. sci. and tech. 2001;167:187-222.

[14] Dunn MJ, Masri AR, Bilger RW, Barlow RS, Wang GH. The compositional structure of highly turbulent piloted premixed flames issuing into a hot coflow. Proceedings of the combustion institute 2009;32:1779-1786.

[15] Dunn MJ, Masri AR, Bilger RW. A new piloted premixed jet burner to study strong finite-rate chemistry effects. Combust. and flame 2007;151:46-60.

[16] Lipatnikov AN, Chomiak J. Molecular transport effects on turbulent flame propagation and structure. Prog. Energ. Combust. Sci. 2005;31:1-73.

[17] Chen JH, Im HG. Stretch effects on the burning velocity of turbulent premixed hydrogen/air flames. Proceedings of the combustion institute 2000;28:211-218.

[18] Lipatnikov AN, Chomiak J. Effects of premixed flames on turbulence and turbulent scalar transport. Prog. Energ. Combust. Sci. 2010;36:1-102.

[19] Yaldizli M, Mehravaran K, Mohammad H, Jaberi FA. The structure of partially premixed flames in high-intensity turbulent flows. Combust and flame 2008;154:695-714.
[20] Shanbhogue SJ, Husain S, Lieuwen T. Lean blowoff of bluff body stabalized flames: scaling and dynamics. Prog. Energ. Combust. Sci. 2009;35:98-120.
[21] Williams FA. Detailed and reduced chemistry for hydrogen autoignition. Journal of loss prevention in process industries. 2008;21:131-135.
[22] Poinsot T, Veynante D. Theoretical and numerical combustion. 2005, second edition: Edwards RT.
[23] Babkovskaia N, Haugen NEL, Brandenburg A. A high-order public domain code for direct numerical simulations of turbulent combustion. Journal of computational physics. 2011;230:issue 1
[24] Kraichnan RH. Diffusion by a random velocity field. The physics of fluids 1970;13:22-31.
[25] Carera A, Sagués F, Sancho JM. Stochastic generation of homogenous isotropic turbulence with well-defined spectra. Physical review E 1993;48:2279-2287.
[26] Pope SB. Turbulent flows. 2009, Sixth printing: Cambridge university press.
[27] Süli E, Mayers D. An introduction to numerical analysis. 2008, fourth printing: Cambridge university press.
[28] Sreenivasan KR. On the universality of the Kolmogorov constant. Phys. Fluids 1995;7:2778-2784.
[29] Wilke CR. A viscosity equation for gas mixtures. Journal of chemical physics 1950;18:517-519.
[30] Meecham WC, Clever WC. Use of C-M-W representations for nonlinear random process applications, Statistical models and turbulence. 1972, second volume: Springer Berlin/Heidelberg.
[31] Ohlén G. Kvantvärldens fenomen-teori och begrepp. First printing, 2005. Studentlitteratur.
[32] Sun CJ, Sung CJ, He L, Law CK. Dynamics of weakly stretched flames: quantitative description and extraction of global flame parameters. Combust. and flame 1999;118:108-128.
[33] Glassman I. Combustion. Third edition, 1996. Academic press.